Building Quantum Systems with Ytterbium Rydberg Arrays

Samuel Saskin

a dissertation

presented to the faculty

of princeton university

in candidacy for the degree

of doctor of philosophy

reccommended for acceptance by

the Department of Physics

Advisor: Professor Jeff Thompson

November 2021

Abstract

Neutral atoms trapped in optical tweezer arrays have emerged as a promising platform for quantum science. The dynamic reconfigurability of tweezer traps enables a high degree of single atom control and the generation of large-scale defect-free atom arrays in many geometries. Furthermore, the ability to introduce long-range interactions via excitation to Rydberg states, enables the implementation of high-fidelity multi-qubit gates and the study of many-body quantum physics. Prior to the work in this thesis all existing neutral atom tweezer platforms have used alkali atoms, which have a single valence electron.

Alkaline-earth atoms (AEA), such as Ytterbium (Yb), have a second valence electron and additional electronic structure, leading to many potential advantages in terms of coherence and control, including ultralong coherence for nuclear spin qubits encoded in a $J = 0$ electronic ground state, metastable states for shelving quantum information or metrological applications, and broad and narrow cycling transitions for rapid laser cooling to low temperatures and low-loss fluorescence imaging. Furthermore, the core electron in AEA Rydberg states enables the trapping of Rydberg states via the polarizability of the ion core, allows for high-fidelity Rydberg state detection utilizing the fast autoionization decay of ion core excited states, and leads to strong hyperfine coupling in Rydberg states of fermionic isotopes.

In this thesis, we discuss the motivation (Chapter 1) and many technical details (Chapter 2) for building the first Yb optical tweezer experiment. In Chapter 3, we present a technique for high-fidelity imaging (0.9985) of ^{174}Yb using the narrow $^1S_0 \rightarrow {}^3P_1$ transition for simultaneous cooling and imaging in 532 nm magic-wavelength tweezers. In Chapter 4, we discuss novel spectroscopy of ^{174}Yb Rydberg states, including the $^3S_1$ series. In Chapter 5, we show the first demonstration of trapped AEA Rydberg states in red-detuned optical tweezers, utilizing the ion core polarizability.

In Chapter 6, we propose and demonstrate a novel scheme for controllably turning on and off Rydberg excitations and Rydberg-mediated entanglement, via light shifts induced by a beam near-resonant with a Yb^+ ion core transition. Finally, we briefly discuss future steps towards implementing quantum gates in ^{171}Yb ($I = 1/2$) nuclear spin qubits (Chapter 7).

Acknowledgements

I'd like to take the time of acknowledge all of the people who've helped me along the way in these past five years. First off, I want to thank my advisor, Jeff Thompson, without whom none of this work would have been even remotely possible. The breadth of Jeff's scientific knowledge and insights are remarkable to witness and the passion, precision, and innovation with which he conducts research have been crucial to this project every step of the way. When I started out on this project I had very little experience in the field and Jeff has helped guide me from the start with a willingness to walk me through any concept or technique that I had yet to understand. I will forever be a better researcher because of his mentorship and I am confident the Thompson Lab will continue to produce excellent research under his guidance.

Over the years I've worked with many incredible lab mates. Shuo and Alex have been crucial partners in this research for the last few years and their dedication has been instrumental in driving this project forward. I also want to acknowledge Rohit, Sattwik, Brandon, Yijian, Conner, and Francesco, all of whom have made important contributions to this research in one way or another. The REI team, especially Chris and Mouktik who have been here with me from the start of the Thompson Lab, have also been delightful colleagues to share a space with all of these years. But most of all I want to thank Jack, who I have spent every day with from the day we walked into a room with two empty optical tables. You have been not only a tremendous colleague and researcher, but also a wonderful friend.

I have also been blessed with a wonderful group of friends that have given me an incredible social circle over these many years in Princeton. There are simply too many of you to list, but I want to especially thank Aaron, Archit, Ben, and Dan for being incredible roommates over the years. I also want to thank all of my friends from outside of Princeton, whether it be from college or my childhood in NYC, all of

whom I've been incredibly lucky to stay so close with over the years.

Next I want to thank my family - Mom, Dad, and Sophie. There's simply no way I'd be here without your support not just during graduate school but for my entire life. I feel so lucky to have all of you and cherished my frequent weekend visits home during graduate school. I am so excited to finally be living in the same city once again. Finally, I want to thank Alyssa, who I am so unbelievably lucky to have met at Princeton. I am so thankful for you and all the support you have given and continue to give me. I am beyond excited to continue our lives together in NYC.

As a final aside I want to thank the ARO/LPS for their years of financial support through the Quantum Computing Graduate Research Fellowship.

Contents

List of Tables

List of Figures

Chapter 1

Introduction

1.1 Neutral atoms for quantum science

In the fields of quantum engineering and experimental quantum science a major goal is to create controllable and complex quantum systems. These two capabilities are highly desirable for a myriad of applications in quantum science, but most notably for the purposes of quantum computing and simulating many-body quantum physics. In the context of building a quantum computer it is desirable to be able to both control the quantum state of single qubits and engineer the coherence time of these states to be very long relative to the time it takes to manipulate the quantum state of the qubit. It is also necessary to have strong interactions (again relative to qubit coherence times) between qubits in order to implement multi-qubit gates. Similarly, local control and strong interactions between particles afford the capability to simulate complex Hamiltonians and study new regimes of many-body physics.

There is a massive and ever-growing landscape of research in the field of quantum science seeking to engineer quantum systems, which simultaneously achieve high single particle control and coherence and strong tunable and complex interactions between

quantum particles. While a plethora of candidate physical systems exist, I wish to divide the discussion of these myriad of methods into two possible approaches: bottom-up assembly and a top-down assembly of quantum systems.

Bottom-up assembly refers to engineering single quantum particles and building a quantum system by assembling many of these individual particles into a desired many-body geometry. This is typically the technique used for systems focused on quantum computing applications, as the requirements for the level of control over single qubits is often higher than what is necessary for quantum simulation. For example, the two leading platforms for quantum computation in terms of state of the art gate fidelities, superconducting qubits and trapped-ion qubits, are prime examples of the bottom-up approach.

The bottom-up approach towards building quantum systems is often accompanied by challenges to scale to very large quantum systems. Alternatively, top-down assembly takes the approach of starting with a very large number of quantum particles and engineering some aspects of single particle control and detection into the system. While this approach often allows for larger quantum systems compared to canonical bottom-up systems, it can be difficult to achieve comparable levels of single particle control in top-down systems.

The top-down approach is a popular method for studying many-body quantum physics with neutral atoms. Neutral atoms have long been at the forefront as a platform for studying many-body quantum systems due to the identical nature of each atom, the ability to precisely control the quantum states of atoms with lasers and microwaves, and the capability to laser cool and trap very large numbers of ultracold atoms. The first demonstration of a Bose-Einstein condensate [2, 3] sparked a massive interest in using ultracold atomic gases to achieve interesting and previously unobserved regimes of physics. A further important development in control over neutral atoms is the in-

troduction of optical lattices [4], which via periodic optical potentials, enable control over the geometry of ultracold quantum gases. However, at this point, study of the properties of these quantum systems was largely at the ensemble level, lacking single particle resolution and control. The introduction of quantum gas microscopes [5] enabled true top-down quantum system engineering with ultracold atoms, where atoms at individual optical lattice sites could be detected via a high-resolution microscope objective. Quantum gas microscopes have been used to study a vast array of interesting many-body physics such as single-site resolution of bosonic Mott insulators [6, 7], properties of the superfluid to Mott insulator phase transition [8, 9] antiferromagnetic spin-1/2 chains [10], and the Fermi-Hubbard model [11, 12, 13]

Another attractive property of neutral atoms is the ability to engineer long-range interactions via Rydberg states [14, 15, 16]. While the neutral atoms interact very weakly in the ground state, exciting an atom to a high principal quantum number Rydberg state creates a large effective electric dipole moment. Exciting multiple atoms to Rydberg states leads to strong long-range dipole-dipole interactions between these atoms. Notably, the fact that neutral atoms only exhibit strong interactions when they are excited to Rydberg states offers the highly desirable capability to turn on and off interactions in the system.

The introduction of optical tweezers [17] offers an alternative bottom-up approach to neutral atom quantum systems more akin to superconducting qubits and trapped-ion systems. Trapping single atoms in the optical potential of tightly-focused laser beams offers an extremely high degree of single-atom control via the ability to move individual atoms [18], control their quantum states [19, 20], individually detect atoms via fluorescence imaging [21], and cool atoms to their vibrational ground state [22, 23]. Furthermore, long-range and tunable interactions can be introduced to the system via exciting atoms to Rydberg states [14, 16], collisions [24, 25, 26], or optical cavities

[27, 28, 29].

Recent experimental progress has demonstrated the promise of neutral atom optical tweezer arrays as a platform for quantum computation and quantum many-body physics. Through the use of multi-tone acousto-optic deflectors or spatial light modulators, reconfigurable and defect-free arrays of atomic qubits trapped in optical tweezers can be constructed in 1D [30], 2D [31], and 3D [32]. Furthermore, long-range Rydberg interactions have been used to both implement two-qubit gates [15, 33, 34, 35, 36] and explore interesting many-body physics, such as ordered Rybderg crystals [37] and Ising spin-models [38].

Prior to the beginning of the work in this thesis all neutral atom tweezer arrays have been built using alkali atoms, such as Rubidium (Rb), with a single valence electron. However, alkaline-earth atoms, such as Ytterbium (Yb) and Strontium (Sr), due to a second valence electron offer additional electronic structure, and consequently many possible advantages. These advantages include ultra-long coherence nuclear spin states, due to the $J = 0$ electronic ground state, strong and narrow optical transitions for efficient laser cooling to much lower Doppler limits than are possible in alkalis, the ability to trap certain Rydberg states in conventional optical tweezer potentials via the polarizability of the ion core [39, 40], and strong hyperfine coupling in Rydberg states [41, 42, 43].

In this thesis I will discuss work to build complex quantum systems out of arrays of Yb atoms trapped in optical tweezers, with strong long-range interactions via excitation to Rydberg states. This work, concurrent with work in the Endres Lab at Caltech and Kaufman Lab at JILA in Sr tweezer arrays [44, 45, 46, 47, 48, 49, 50], represent the first generation of experiments utilizing alkaline-earth atoms in tweezer arrays to engineer quantum systems.

In the remaining parts of **Chapter 1**, I will elaborate on important details of optical

tweezers, Rydberg states and interactions, the advantages of utilizing alkaline-earth atoms in tweezer arrays, and some specific properties of Yb. In **Chapter 2**, I will discuss a host of technical details involved in building the experimental system. In **Chapter 3**, I will discuss our work trapping, cooling, and imaging single Yb atoms in optical tweezers. In **Chapter 4**, I will discuss our work performing Rydberg spectroscopy of some previously unobserved Rydberg series in Yb. In **Chapter 5**, I will discuss our work demonstrating the ability to trap Rydberg states in conventional optical tweezer potentials via the polarizability of the ion core. In **Chapter 6**, I will discuss our work demonstrating selective control of Rydberg excitations utilizing light-shifts on Rydberg states by driving the strong autoionizing ion core optical transition. In **Chapter 7**, I will discuss future steps for implementing high-fidelity quantum gates in ^{171}Yb I = 1/2 nuclear spin qubits.

1.2 Optical Tweezers

Optical tweezers provide a trapping force to atoms via an optical dipole force, where for a certain trap-wavelength the trapping potential for a given atomic state will come from the AC stark shift, given by:

$$U_{dip} = \sum_i \frac{\hbar \Omega_i^2}{4\Delta_i} \tag{1.1}$$

Here the subscript i refers to any electronic state for which there is a non-negligible dipole matrix element to the state for which one is calculating the trapping potential. In the case where the trap wavelength is red-detuned from a given atomic transition ($\Delta_i < 0$) the contribution to the trapping potential from that transition will be attractive (i.e. the atom will be attracted to regions of higher laser intensity). If the trap wavelength of the optical tweezer is chosen such that the net trapping potential

is attractive, then atoms will be trapped by the Gaussian intensity profile of a tightly-focused laser beam. The trapping potential is often rewritten in terms of the state-polarizability, α, and the beam intensity, I.

$$U(r,z) = -\frac{1}{4}h\alpha I(r,z) \tag{1.2}$$

For a Gaussian beam the spatial intensity profile is given by:

$$I(r,z) = \frac{2P_0}{\pi w(z)^2} e^{-\frac{2r^2}{w(z)^2}} \tag{1.3}$$

Here P_0 is the laser power, and $w(z)$ represents the beam-waist throughout the focus and is related to the beam-waist at the focus (w_0) by:

$$w(z) = w_0\sqrt{1 + (\frac{\lambda z}{\pi w_0^2})^2} \tag{1.4}$$

We define the trap depth, U_0, as the magnitude of trap potential at the center of its focus:

$$U_0 = U(r=0, z=0) = \frac{hP_0\alpha}{2\pi w_0^2} \tag{1.5}$$

A crucial condition for an atom being trapped in optical tweezers is that the temperature of the atom is much below the trap depth ($k_b T \ll hU_0$).

We can also calculate the radial and axial trap frequencies of the harmonic trapping potential:

$$\omega_r = \sqrt{\frac{2hP_0\alpha}{\pi m w_0^4}} \tag{1.6}$$

$$\omega_z = \sqrt{\frac{hP_0\alpha\lambda^2}{\pi^3 m w_0^6}} \tag{1.7}$$

One of the attractive capabilities of optical tweezers is the ability to arrange and reconfigure individual tweezers in different array geometries via the use of acousto-optic deflectors (AOD) and spatial light modulators (SLM). In the case of AODs multi-tone radio frequencies drive multiple diffracted beams, which each enter a high-NA microscope objective at a different angle, leading to a different position for each diffracted beam in the focal plane. Thus, through the use of an arbitrary waveform generator (AWG), one can design RF waveforms that allow for an arbitrary arrangement of many optical tweezers in 1D. Furthermore, due to the ability to rapidly change the AWG waveform driving the AOD, the geometry of 1D tweezer array can also be reconfigured during a given experimental sequence [30].

Dynamic reconfigurability of tweezer geometries is a necessary condition for generating large-scale defect free arrays of trapped atoms. Loading of optical tweezers from a cold atomic gas is a fundamentally stochastic process. Atoms are initially loaded in a Poisonnian manner from the background atomic gas, however, a process known as light-assisted collision will eject pairs of atoms by exciting them to a molecular bound state, leading to a parity projection, which leaves either 0 or 1 atom in each tweezer trap [17, 51]. A common technique to engineering defect-free 1D arrays is to take a fluorescence image of a loaded tweezer array, then turn off RF tones associated with empty sites, followed by ramping the RF tones of filled sites such that they occupy the desired positions in the final array [30].

Using a pair of orthogonal AODs allows for the creation of rectangular 2D arrays, however, the ability to reconfigure into defect-free arrays is complicated by the fact that turning off a single RF tone will turn off an entire row or column of tweezers, not just a single site. A solution to this problem is to combine the capabilities of a SLM

and a pair of orthogonal AODs. By varying the phase pattern on a SLM, arbitrary 2D geometries of optical tweezer arrays can be generated [52]. Unfortunately, the phase patterns of a SLM cannot be reconfigured at sufficient speeds to engineer a defect-free array from the initial stochastic loading process. As a solution, one can combine a fixed arbitrary SLM array with a set of moving optical tweezers, generated by orthogonal AODs, which can pick and move atoms throughout the fixed array generated by the SLM. Thus, after an initial image of the stochastically loaded fixed array is taken, a series of moves can be programmed for the moving tweezers to move atoms into the desired configuration for a defect-free array in the fixed SLM geometry [31].

1.3 Rydberg states and interactions

Here I briefly discuss some important details and properties of Rydberg states and their interactions. For an in depth review of Rydberg states and their application for quantum information I recommend Ref. [16].

The energy of the Rydberg series in Hydrogen as a function of the principal orbital quantum number (n) is given by:

$$E_H(n) = -\frac{\mathrm{Ry}}{n^2} \tag{1.8}$$

where $\mathrm{Ry} = \frac{m_e e^4}{8\epsilon_0^2 h^2}$, is the Rydberg energy constant.

For non-Hydrogen atoms we can no longer define the energy of a single Rydberg series as stated, however, in alkali atoms, the energy of a given Rydberg series can be parameterized by a quantum defect, δ_{nlj}, which accounts for its deviation from the Hydrogen model due to the effects of the valence electron's interaction with the core (generally for states with high orbital angular momentum ($L > 3$) the interaction of

the valence electron's orbit with the core becomes negligible and the quantum defect is zero):

$$E(n) = -\frac{\mathrm{Ry}}{(n - \delta_{nlj})^2} \tag{1.9}$$

The quantum defect for a given Rydberg series is determined from a phenomenological fit to Rydberg spectroscopic data, using the Rydberg-Ritz formula.

$$\delta_{nlj} = \delta_0 + \frac{\delta_2}{(n - \delta_0)^2} + \frac{\delta_4}{(n - \delta_0)^4} + ... \tag{1.10}$$

Notably, at sufficiently high principal orbital quantum number, n, the quantum defect of a Rydberg series becomes to good approximation independent of n ($\delta_{lj} \approx \delta_0$). Thus at sufficiently high n ($n > \sim 40$) we can define the energy of a given Rydberg series in the same way as in Hydrogen, but with an effective principal quantum number $n^* \approx n - \delta_{lj}$:

$$E(n^*) = -\frac{\mathrm{Ry}}{n^{*2}} \tag{1.11}$$

In two-valence electron atoms, we now define the quantum defect of a Rydberg series in terms of the quantum numbers, δ_{nslj}. Similar to alkalis, for many Rydberg series it holds to good approximation that δ_{nslj} will be independent of n at sufficiently high n. However, the core electron can lead to the existence of perturbing states, which cause certain Rydberg series to have quantum defects with large n-dependence, even at high n [53]. It is generally necessary to perform spectroscopy on an alkaline-earth Rydberg series to determine if its quantum defect is moving in n or "well-behaved" (n-independent at sufficiently high n).

Due to the large orbital radius of Rydberg states they possess large dipole matrix

elements to nearby Rydberg states with a dipole allowed transition ($l' = l \pm 1$), which scale with the effective principal orbital quantum number as $\boldsymbol{\mu} \propto n^{*2}$.

The large dipole moments cause Rydberg states to both have strong DC Stark shifts ($\propto n^{*7}$) and interact strongly through dipole-dipole interactions. The resonant dipole-dipole interaction between two Rydberg states with non-zero dipole matrix element between them is typically written in the form:

$$V_{dd} = \frac{C_3}{R^3} \tag{1.12}$$

The R^3 distance dependence is characteristic of a dipole-dipole interaction, with interaction coefficient $C_3 \propto n^{*4}$ ($\boldsymbol{\mu} \cdot \boldsymbol{\mu} \propto n^{*2} n^{*2}$).

If we consider two atoms in the same Rydberg state, $|r\rangle$, there will be no resonant dipole-dipole interaction between these states. However, there will be a second-order Van der Waals interaction mediated through pairs of nearby intermediate Rydberg states, with non-zero dipole matrix elements to $|r\rangle$. We write the Van der Waals interaction as:

$$V_{vdw} = \frac{C_6}{R^6} \tag{1.13}$$

The form of V_{vdw} can be understood as coming from second-order pertubation theory of the resonant dipole-dipole interaction, which yields an R^6 distance scaling and an interaction coefficient $C_6 \propto n^{*11}$ ($\frac{V_{dd} V_{dd}}{\Delta} \propto \frac{n^{*4} n^{*4}}{n^{*-3}}$, where the frequency spacing between adjacent Rydberg levels scales as n^{*-3}). Notably, the strength of Van der Waals C_6 coefficient is highly dependent on the detuning, Δ, of adjacent Rydberg pair states $|r'r''\rangle$ to the pair state $|rr\rangle$. Consequently, the strength of the C_6 coefficient for a specific series depends quite sensitively on the relative quantum defects between

that series and series with $|\Delta L| = 1$. In the case where a pair of intermediate Rydberg levels $|r'r''\rangle$ are very close in energy to the pair state $|rr\rangle$ ($V_{dd} \gg \Delta$), this will create what is known as a Förster resonance [54], and lead to an interaction of the form of the resonant dipole-dipole interaction.

We now consider the case where two atoms are simultaneously driven from a ground state, $|g\rangle$ to a Rydberg state, $|r\rangle$. If one atom populates $|r\rangle$, the second atom will be blocked from being driven to $|r\rangle$ in the case where the Van der Waals interaction is much greater than the Rabi frequency of the drive ($V_{vdw} \gg \Omega$). This regime is called the Rydberg blockade [14, 15], where instead of driving single atom Rabi oscillations between $|g\rangle$ and $|r\rangle$ at Rabi frequency, Ω, we will drive two atom oscillations between $|gg\rangle$ and the Bell state $\frac{1}{\sqrt{2}}(|gr\rangle + |rg\rangle)$ at an effective rabi frequency $\sqrt{2}\Omega$, since double-excitations to $|r\rangle$ are blocked by a Van der Waals shift to the pair state $|rr\rangle$. We define the blockade radius, R_b as the distance within multiple Rydberg excitations cannot occur, given by:

$$R_b = \left(\frac{C_6}{\Omega}\right)^{\frac{1}{6}} \tag{1.14}$$

In general, if we simultaneously drive N atoms within a blockade radius to the Rydberg state $|r\rangle$, then we will drive collective Rabi oscillations between the state $|gg...g\rangle$ and the many-body state $|W\rangle = \frac{1}{\sqrt{N}}(|rg...g\rangle + |gr...g\rangle + ... + |gg...r\rangle$ at an effective Rabi frequency of $\sqrt{N}\Omega$.

The Rydberg blockade has been utilized to implement two-qubit gates in neutral atom qubits encoded in hyperfine ground states. In the canonical Rydberg blockade gate, proposed in Ref. [15] and first demonstrated in Refs. [33, 55], a laser drives a transition between one of the qubit ground states $|1\rangle$ and the Rydberg state $|r\rangle$. First a π-pulse is driven on the control atom from $|1\rangle$ to $|r\rangle$. Next a 2π-pulse is driven on

the target atom, and finally a second π-pulse is driven on the control atom. In the case, where the control atom is in $|0\rangle$ it will be unaffected by either π-pulse and the target atom will pick up a π phase shift from the 2π-pulse, when it is in $|1\rangle$. However, if the control atom is in $|1\rangle$ it will be driven to the Rydberg state and the target atom will not be excited to the Rydberg state, even if it is in $|1\rangle$ due to the Rydberg blockade. Furthermore, the control atom will pick up a π phase shift from the two π-pulses. Thus the total effect of the pulse sequence acts as follows in the two-qubit basis: $|0_c0_t\rangle \rightarrow |0_c0_t\rangle$, $|0_c1_t\rangle \rightarrow -|0_c1_t\rangle$, $|1_c0_t\rangle \rightarrow -|1_c0_t\rangle$, $|1_c1_t\rangle \rightarrow -|1_c1_t\rangle$. This controlled-phase gate can easily be converted to a CNOT gate with single-atom $\pi/2$ rotations between $|0_t\rangle$ and $|1_t\rangle$ [56]. While this example of the Rydberg blockade gate requires local addressing of Rydberg excitation beams, high fidelity two-qubit gates utilizing the Rybderg blockade have also been achieved with a global Rydberg excitation beam via a more complex pulse sequence [36].

The fundamental limit on the fidelity of a two-qubit Rydberg blockade gate is proportional to the gate time, $\tau = \frac{2\pi}{\Omega}$, divided by the finite lifetime of the Rydberg state, τ_r [57]. The Rydberg state radiative lifetime scales as n^{*3}, however, in practice, in non-cryogenic environments, decay from Rydberg states is dominated by blackbody decay, which leads to a scaling of the Rydberg state lifetime of n^{*2}.

While the fundamental error rates can be quite small, in practice a number of other technical factors can lead to imperfect Rydberg blockade gates [58]. First, it is generally a technical challenge to drive single-photon transitions to Rydberg states, due to the extremely short wavelengths necessary to drive the transition. Thus, in practice Rydberg transitions are typically driven via two-photon transitions, with an intermediate state detuning, Δ, and effective Rabi frequency $\Omega_{\text{eff}} = \frac{\Omega_1\Omega 2}{\Delta}$. However, this leads to a spontaneous emission rate out of the intermediate state proportional to $\Gamma * (\frac{\Omega}{\Delta})^2$, where Γ is the scattering rate out of the intermediate state. Therefore, to minimize

the spontaneous emission rate it is often necessary to work at large intermediate state detuning, Δ, which in turn limits the effective Rabi frequency to the Rydberg state. A second technical limitation is dephasing between the ground and Rydberg state during the gate. In general dephasing is affected by atomic motion as result of the finite temperature of atoms, where the coherence depends on the atomic temperature as, $T_2 \propto \frac{1}{\sqrt{T}}$ (scaling with temperature is due to a phase error which is linear in the Doppler shift, with $v \propto \frac{1}{\sqrt{T}}$). A further source of decoherence is laser phase noise for the Rydberg excitation lasers [59]. In the following section, I will discuss how certain properties of alkaline-earth atoms can help overcome some of these technical limitations.

1.4 Advantages of alkaline-earth atoms

Alkaline-earth atoms, with a second valence electron, introduce additional electronic structure compared to alkali atoms, specifically, with the introduction of singlet and triplet spin states. This richer electronic structure leads to many features that can be leveraged for additional quantum control relative to alkali atoms.

First, due to the existence of total spin zero states the ground state of alkaline-earth atoms (^{1}S$_0$) has zero total angular momentum ($J = 0$). The lack of any electronic angular momentum enables ultralong coherence ground-state qubits stored in the nuclear spin states of fermionic alkaline-earth isotopes, such as ^{171}Yb (I = 1/2) or ^{87}Sr (I = 9/2). The magnetic moment of a nuclear spin is $\sim 1000\times$ smaller than that of an elecronic spin, leading to exceedingly small effects from magnetic field noise. Furthermore, there is an absence of differential light shifts from the optical tweezers on the nuclear spin qubit states, whereas in alkalis differential light shifts on the hyperfine qubit states can be the leading source of qubit decoherence [57]. The I = 1/2 nuclear spin in ^{171}Yb is a particularly attractive candidate for a long-lived

nuclear spin qubit.

Second, while alkali atoms have only broad allowed cycling transitions for laser cooling ($^2S_{1/2} \rightarrow ^2P_{1/2,3/2}$, $\Gamma \approx 2\pi \times 10$ MHz), alkaline-earth atoms contain both a broad cooling transition ($^1S_0 \rightarrow {}^1P_1$, $\Gamma \approx 2\pi \times 30$ MHz) and a forbidden narrow cooling transition ($^1S_0 \rightarrow {}^3P_1$, Yb: $\Gamma = 2\pi \times 182$ kHz, Sr: $\Gamma = 2\pi \times 7$ kHz). While the $^1S_0 \rightarrow {}^3P_1$, is in principle dipole forbidden due to $\Delta S = 1$, a small amount of singlet-triplet mixing between $^1P_1$ and $^3P_1$ leads to a sufficiently fast cycling transition for laser cooling applications. The existence of a narrow cooling transition allows alkaline-earth atoms to reach far colder temperatures through Doppler cooling alone ($T_D \propto \Gamma$) than alkalis. For comparison, the Doppler limit of Rb ($T_D = 146\ \mu K$) is $\sim 30\times$ bigger than Yb ($T_D \approx 5\ \mu K$) and $\sim 800\times$ bigger than Sr ($T_D \approx 200\ nK$). We also note that use of $^3P_1$ as the intermediate state for two-photon transitions to the Rydberg state reduces the problem of spontaneous emission compared to alkalis, since the rate of scattering errors out of the intermediate state is also proportional to Γ.

Third, in addition to the narrow $^3P_1$ transition, there exist two metastable states, $^3P_0$ and $^3P_2$, with radiative lifetimes of 10s of seconds. The ultra-narrow (<10 mHz) clock transition ($^1S_0 \rightarrow {}^3P_0$) in alkaline-earth atoms is widely utilized for metrology and is responsible for the highest-performance atomic clocks to date [60]. The clock state in Sr tweezer arrays has recently been utilized for metrology applications [47, 48, 49]. The long-lived clock state can also be utilized for quantum computation, either with a ground-clock state qubit or as an effective ground state for a nuclear spin qubit. The latter is especially attractive for a few reasons. First, the clock state is also $J = 0$, so all the long coherence advantages of the atomic ground state will exist in the clock state as well. Second, when quantum information is stored in a clock state nuclear spin qubit it will be unaffected by laser light resonant with electronic transitions out of the ground state. This could allow for schemes to cool,

image, and load atoms in specific sites of a tweezer array, without disturbing the quantum state of atoms at other sites. Third, using the clock state as an effective ground state allows for somewhat more experimentally achievable optical wavelength for single-photon transitions to Rydberg states (302 nm in Yb, 317 nm in Sr vs. 296 nm in Rb). Single-photon transitions are highly attractive as their use eliminates the problem of spontaneous emission from the intermediate state, and in turn allows one to achieve significantly faster Rabi frequencies to the Rydberg state. Single photon transitions from the clock state to a Rydberg state have been utilized in a Sr tweezer array to achieve state of the art Bell state fidelities via Rydberg blockade [50].

Fourth, a major limitation of alkali tweezer systems is that the Rydberg electron has the polarizability of an essentially free electron, and consequently feels a repelling force from an optical tweezer. Thus, in existing alkali tweezer experiments, the tweezers are turned off during excitation to the Rydberg state. However, due to the non-zero temperature of the atoms, the time during which the tweezers can be turned off is limited so that the atoms can be recaptured before they leave the region of the trap. This time is generally limited to 10-20 μs, which is notably at least an order of magnitude smaller than typical lifetimes of relevant Rydberg states (100s of μs). This severely limits the number of possible gate operations or the amount of time one can probe Rydberg dynamics below the fundamental limit of the Rydberg state lifetime.

However, in alkaline-earth atoms the remaining ion core also has a polarizability that for Rydberg states of sufficiently high-n (further details are in Chapter 5) can have a larger attractive force than the ponderomotive repulsive force on the Rydberg electron, leading to a net trapping force on an atom in the Rydberg state [61]. The capability to trap Rydberg states in optical tweezers can enable interrogation of the Rydberg state for the full state lifetime. Furthermore, while the blackbody lifetimes of

low orbital angular-momentum Rydberg states are on the scale of 100s of μs, circular Rydberg states in cryogenic environments can have lifetimes exceeding 1 second. Proposals to use circular Rydberg atoms as the basis for a quantum computer [62] can leverage the trapping capabilities of alkaline-earth Rydberg states to take advantage of the extremely long circular state lifetimes.

Fifth, unlike alkalis, where there is a single valence electron, there exist strong optical transitions in the ion core of alkaline-earth Rydberg states. The ion core transition can be used for very high-fidelity Rydberg state detection via rapid loss through autoionization decay [63, 50]. Autoionization loss rates faster than 10 ns can easily be achieved in Yb, enabling Rydberg detection fidelities > 0.9999 assuming a 100 μs Rydberg state lifetime and perfect atom detection. Furthermore, the autoionizing ion core transition can be used to implement local control over Rydberg state excitations in a tweezer array via light-shifting the Rydberg state out of resonance with global Rydberg excitation beams (further details are in Chapter 6).

Sixth, contrary to alkalis, where the hyperfine coupling in the Rydberg states scales as n^{*-3} ($\sim$80 kHz at $n = 80$ in Rb [64]), there is strong, n-indepedent, hyperfine coupling for fermionic alkaline-earth isotopes in the Rydberg state due to the constant contact interaction of the core electron with the nucleus [41, 42, 43]. The presence of strong hyperfine coupling creates interesting and complex structure in the Rydberg states that could potentially be used for new multi-qubit gate schemes or accessing a different set of interaction terms in spin Hamiltonians.

1.5 Properties of Yb

Figure 1.1 shows the electronic level structure of ^{174}Yb for states relevant to our experiment. While the electronic structure of the bosonic isotopes of Yb and Sr are quite similar an important and relevant difference is the broader $^1\mathrm{S}_0 \rightarrow {}^3\mathrm{P}_1$ linewidth

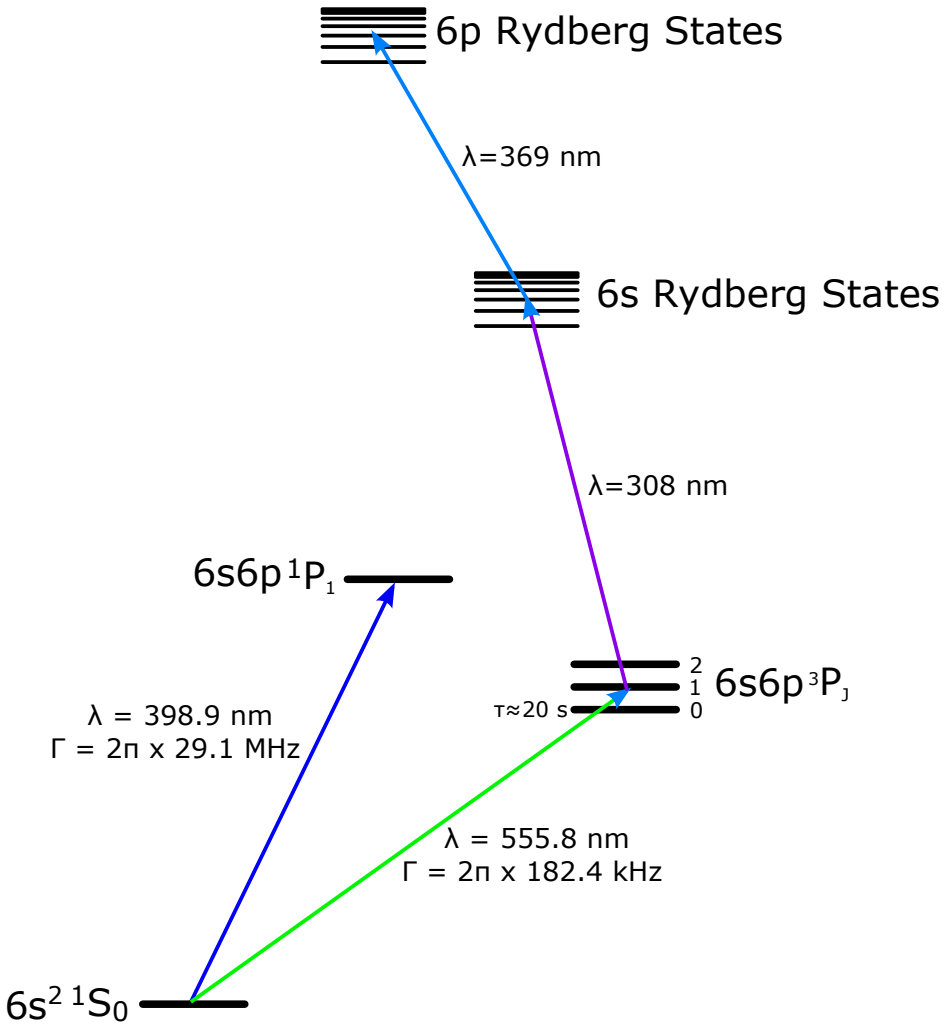

Figure 1.1: Level diagram of relevant states and transitions in Yb.

in Yb ($\Gamma = 2\pi \times 182$ kHz) compared to Sr ($\Gamma = 2\pi \times 7$ kHz). Furthermore, the fermionic isotope of Yb most suitable for quantum information protocols, ^{171}Yb, has a nuclear spin of I = 1/2, compared to ^{87}Sr, which has a nuclear spin of I = 9/2.

Table 1.1 shows some important properties of the two main cycling transitions in Yb, $^1S_0 \rightarrow {}^1P_1$ and $^1S_0 \rightarrow {}^3P_1$.

	$^1S_0 \rightarrow {}^1P_1$	$^1S_0 \rightarrow {}^3P_1$
λ	398.9 nm	555.8 nm
$\Gamma/2\pi$	29 MHz	182 kHz
I_{sat}	60 mW/cm^2	0.14 mW/cm^2
T_D	700 μK	4.4 μK

Table 1.1: Important properties of singlet and triplet cycling transitions in Yb.

Chapter 2

Experimental System

In this chapter I will discuss many of the technical details that went into building and operating the experiment, including vacuum chamber design, laser systems, and the process of loading laser cooled atoms into optical tweezers.

2.1 Vacuum Chamber

In this section I consider the general design principles for our vacuum chamber, with some specific details for building a high-flux and long-lasting oven for Yb.

2.1.1 Design Principles

Fig. 2.1 shows a CAD model of our vacuum chamber and an image of the chamber as it exists in our experiment. The design for our vacuum chamber consists of three crucial sections. First, we have an oven, which typically operates at 440 °C, yielding a hot Yb gas with vapor pressure 3×10^{-3} Torr. The hot Yb atoms traverse an array of thin nozzles (described in detail in subsection 2.1.2), which collimate the atoms along the plane of a 2D cross. Second, in an initial stage of laser cooling, light from a 399 nm laser, resonant with the singlet transition, propagates along both arms of

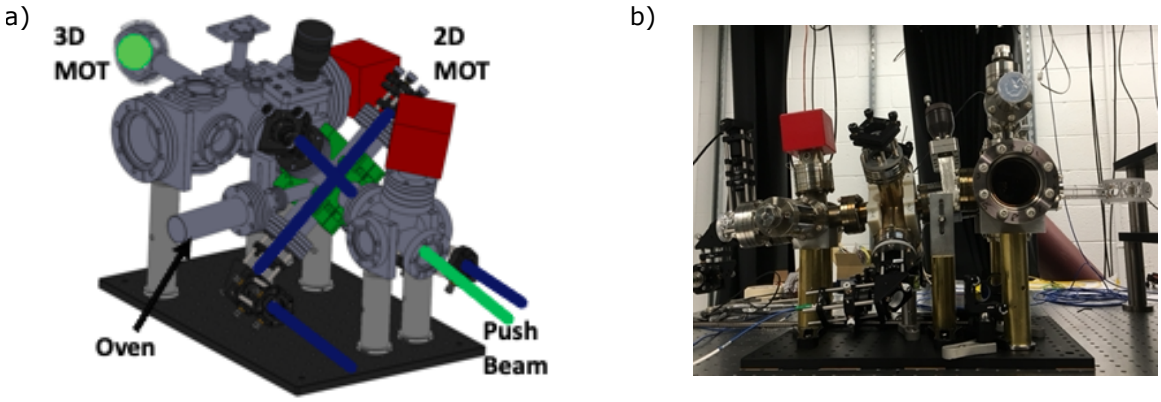

Figure 2.1: a) CAD model of vacuum chamber. b) Picture of vacuum chamber.

the cross to capture atoms from the oven in a 2D MOT. We then use light at 556 nm, resonant with the intercombination line, to push atoms out of the 2D MOT and through a differential pumping tube. UHV ion pumps (SAES NEXTorr D200, D500) are placed on either side of the differential pumping tube, where we achieve pressures of $\sim 10^{-9}$ Torr and $\sim 10^{-11}$ Torr, respectively. Finally, the pushed atoms are captured and cooled in a final laser cooling stage in a narrow-line 3D MOT using 556 nm light, where we achieve a density of $\sim 10^{11}$ atoms/cm^3 in 100 ms loading time. Crucially, the capture velocity of the 3D MOT is low enough (7 m/s) such that gravity will have a non-negligible effect on atoms traversing the differential pumping section of the vaccum chamber at that velocity. In order to overcome this constraint we designed the differential pumping tube to be at a $\sim 7°$ degree angle relative to the science cell, such that the pushed atoms can be pushed slightly upward to account for the downward force of gravity during the trajectory of the atoms (details for how this angle was chosen are discussed in more detail in Section 2.6).

2.1.2 Oven

The Yb oven consists of ∼30 g of solid Yb deposited in a vacuum tube, which we heat to 440 °C leading to a vapor pressure of 3×10^{-3} Torr. Between the oven and the

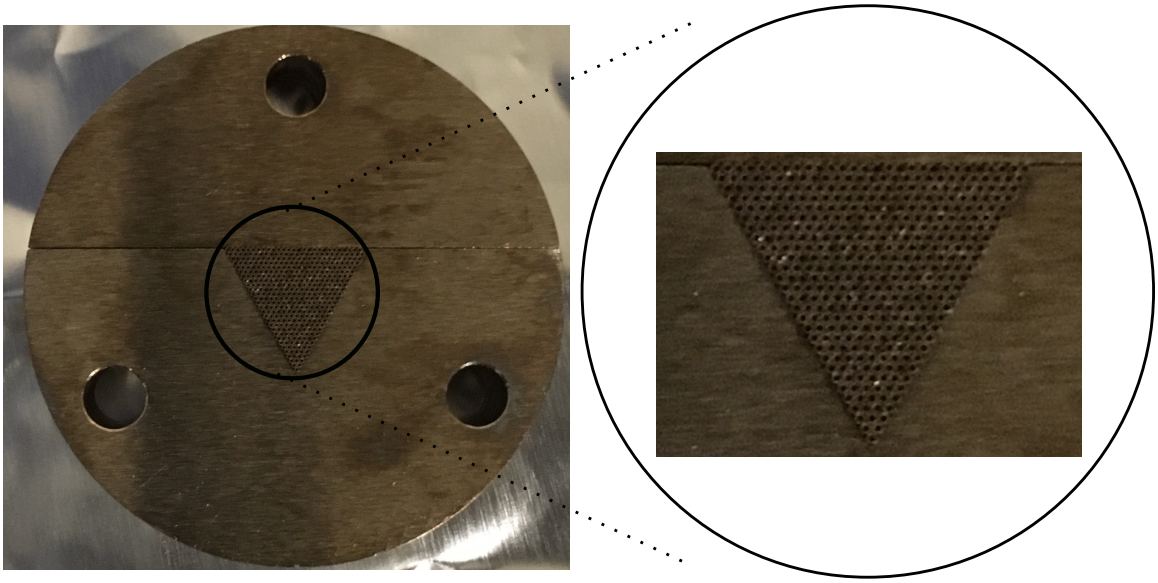

Figure 2.2: A picture of the microtube array in its mount and with a zoomed in look at the array itself.

2D MOT we have a triangular array of 400 stainless steel microtubes (30RW gauge ($d \approx 0.15$ mm), $L \approx 7.5$ mm) (A picture of the array of tubes is shown in Fig. 2.2), an approach developed in Ref. [65]. The high aspect ratio ($L/d = 50$) of the microtubes makes it so that of the hot cloud of atoms that enter the tubes, the distribution of velocities for atoms that end up transmitting through the tubes towards the 2D MOT will have a large percentage of atoms within the capture angle of the MOT beams ($\sim 3°$), effectively sending a collimated beam of hot atoms towards the 2D MOT to be cooled and captured. On the other hand, the large majority of atoms whose velocities are not within the capture angle of the 2D MOT and would've been wasted, are instead not transmitted through the array of microtubes and recycled back into the oven. Another consideration is that atoms with large velocity angles relative to the 2D MOT capture region can end up colliding with and coating the vaccuum windows through which the 2D MOT beams enter. We always keep the region of the oven with the microtube array 30 °C hotter than the rest of the oven to ensure that atoms don't stick to the walls of the microtubes and clog the pathway to the 2D MOT.

We run Monte Carlo simulations of the trajectory of atoms from a hot atomic vapor entering a microtube with aspect ratio of 50. The initial velocity distribution is taken from the 3D Boltzmann distribution for T = 440 °C, and when atoms collide with the walls of the tube the reemission angle is sampled according to Knudsen's cosine law [66]. The simulations find that only $\sim 7\%$ of atoms incident with the entrance to a 50 aspect ratio microtube will be transmitted, however, $\sim 40\%$ of those atoms will have a velocity vector below the capture angle of the 2D MOT, compared to $\sim 3\%$ in the case where the atoms travel straight from the oven to the 2D MOT region. Thus the total flux of atoms, which can be captured by the 2D MOT, is kept roughly constant by including the microtube array but the lifetime of the oven is increased more than ten-fold by recycling atoms that would not intersect with the 2D MOT capture region. We estimate given the initial amount of Yb deposited in the oven that our oven can operate for a few decades.

When we first assembled our vaccuum chamber the microtubes were mounted in a triangular cut region machined at the center of a vacuum flange, which connected our oven elbow to the 2D MOT cross in our vacuum chamber. However, to heat the microtube we needed to directly heat the flange. In the process of temperature cycling the oven a vacuum leak was introduced at the flange connection that contained the microtubes. To avoid future temperature cycling on a vacuum flange connection, for the second version of our oven we machined a similar triangular mounting piece for the microtubes, however the piece was mounted inside the oven tube so the heating of the microtubes occurred before the flange connection. After this design change we have never encountered a vaccuum leak in any part of our chamber.

2.2 Blue Laser System

The first requirement in our experimental system is the ability to laser cool hot Yb atoms to temperatures on the scale of ∼1 mK. Due to the narrow linewidth of the triplet transition, its cooling force is too weak to efficiently cool and capture a large density of atoms from a hot gas. Thus, it is necessary to first perform an initial stage of laser cooling using the broad singlet transition at 399 nm.

The two main requirements for our blue laser system are that it has a low-noise and stable single-frequency output, and that the laser output is high power. Since, the saturation intensity of the singlet transition is fairly high (60 mW/cm^2), and our MOT on the singlet transition consists of two ∼1 cm diameter beams, we ideally would want >100 mW of blue laser power in our MOT. Taking into account approximately 50% losses due to fiber coupling and other lower power uses for our blue light this would require a laser diode which outputs 200-250 mW of 399 nm light to achieve our goals. At 399 nm, there are not commercially available laser diodes, which can achieve this high of a power output in a stable single-frequency mode. For example, our commercial Moglabs external cavity diode laser (ECDL), which satisfies the requirements of a single-frequency and low-noise blue light source, is only able to output <100 mW at maximum current.

2.2.1 Injection Locking

To achieve higher laser powers we implement a technique called injection locking, where using a small amount of light from our commerical Moglabs ECDL laser (master laser) we are able to seed a high-noise high power laser diode (slave laser) and get it to output light in the same frequency mode as our master laser. Given that the bare diode frequency of the slave laser is sufficiently close to the master, injection locking should allow the entirety of the slave laser's high-power output to take on the

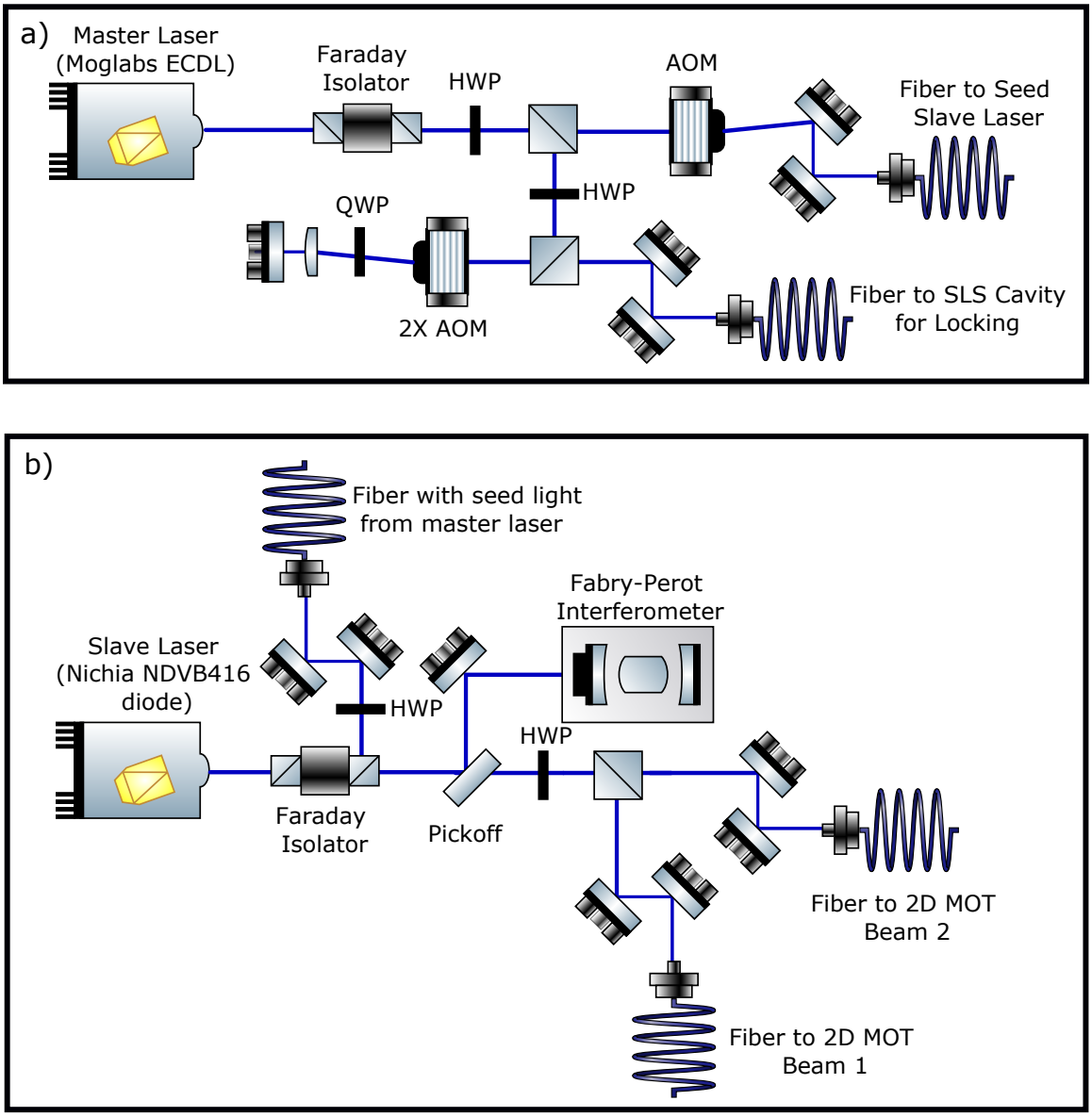

Figure 2.3: a) A schematic of the optics for the 399 nm master laser. b) A schematic of the optics for the 399 nm injection-locked slave laser.

single-frequency mode output of the master laser.

We follow [67] in setting up our injection locking for the blue laser. We started by building a mount for the slave laser diode (Nichia NDVB416) that consists of a mounting cube for a Thorlabs laser diode collimation package and a base plate, between which a peltier cooler is placed to control the temperature of the diode. The diode has a center wavelength between 400 and 401 nm at room temperature so

in order to injection lock we lower the temperature to blue shift the diode's center wavelength and bring it closer to the wavelength of our Moglabs laser. We operate the injection locking with the laser diode set at ~ 18 °C, however to avoid condensation on the mount, we are careful not to decrease the temperature below the dew point of the lab.

The setup involves taking ~ 2 mW of fiber coupled light from the Moglabs ECDL and aligning it back through a commercial Faraday isolator (Thorlabs IO-5-405-LP), whose output polarizer is replaced by a high power PBS (Thorlabs PBS12-405-HP) to seed the slave diode. The seed light is optimally mode-matched with the slave diode by coupling light from the slave diode along the reflected path of the PBS into the fiber that launches the seed light along the same optical path.

We determine the extent to which the slave diode is lasing in the single-mode of the Moglabs ECDL by looking at the transmission signal of the slave diode light through a Fabry-Perot interferometer (Thorlabs SA200-3B). A large single peak, in the cavity transmission, would suggest that the slave diode is lasing in a single-frequency mode. One observes that full injection locking to a single-frequency mode is only fully successful at very specific laser diode currents. The transmission signals through the cavity at non-optimal diode currents are characterized by smaller side peaks in other frequency modes, or by a broad emission spectrum, with no single-frequency peaks. At points where smaller side peaks appear, the height of the main injection-locking peak decreases.

A cavity transmission signal consistent with full injection locking, shown in Fig 2.4a, is first observed at approximately 160 mA of slave diode current. The injection current threshold for the slave diode is approximately 30 mA, so the slave diode must be operated at a power far above threshold for full injection locking to occur. Above the first identified diode current, at which full injection locking occurs, we observe full

injection locking at approximately evenly spaced intervals in the slave diode current of 9-10 mA. At full injection locking points in the diode current, one can observe the full injection locking signal in a region of ∼0.2 mA. One can observe partial injection locking, as is shown in Fig. 2.4b/c, in the region of ∼0.2 to ∼2.5 mA above the current point of full injection locking. No injection locking, which is characterized by the broad emission spectrum in Fig. 2.4d, is observed immediately below the current point of full injection locking. A broad emission spectrum continues to be observed, as the diode current is decreased, until the next point of partial injection locking is reached.

A surprising feature of injection locking is that the full injection-locking signal is bistable and can only be achieved by *decreasing* the slave diode current to the optimal current point. If one tries to approach the optimal current point from below, by increasing the slave diode current, there will be no injection locking signal at all, until a partial injection locking signal occurs in the range of 1-2 mA above the optimal diode current. Then, to reach the full injection locking signal, one must decrease the slave diode current back to the optimal current point from any current above the point where the partial injection locking signal occurs on the increasing current curve.

The optimal slave diode current at which injection locking occurs is extremely sensitive, as small changes in the temperature of the diode or mechanical vibrations can cause the injection lock to be lost. We have at times observed the injection locking signal to remain stable for up to an hour without any feedback, and at other times observed the injection locking signal to only remain stable for seconds at a time. One clear factor in the stability of the injection locking is the length of time since the slave diode has been turned on. This has also been observed in Ref. [68], and is attributed to large variations in the temperature profile of the slave diode in the time nearly following it being turned on.

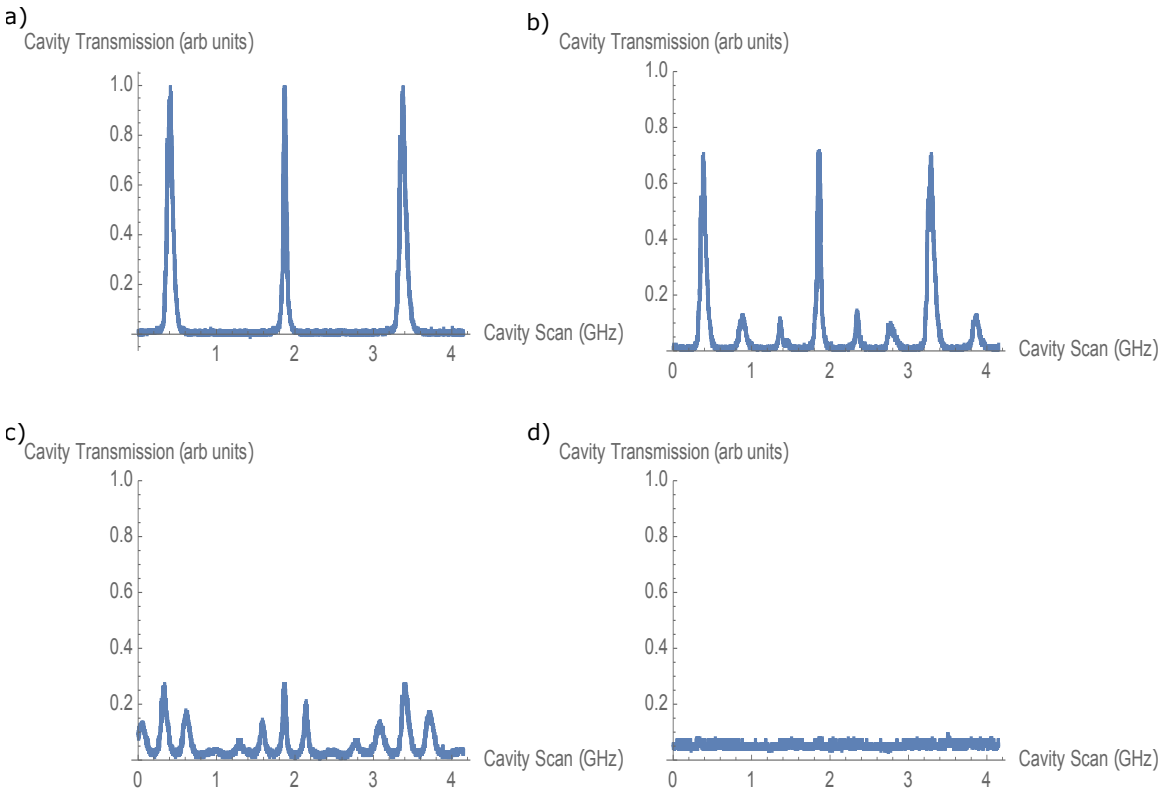

Figure 2.4: a) A cavity transmission plot when the slave diode fully injection locked in a single-frequency mode. This is characterized by one single sharp peak. The free spectral range of the cavity is 1.5 GHz. b) A cavity transmission plot when the slave diode is partially injection locked. There is still a relatively large peak in the frequency mode of the master laser, but smaller side peaks corresponding to other frequency modes also arise. c) Another cavity transmission plot when the slave diode is partially injection locked. In this case the injection locking to the master laser frequency mode is weaker and the slave laser is nearing a broad emission spectrum. d) A cavity transmission plot when there is no injection locking. This is characterized by a broad slave diode emission spectrum and no obvious peaks corresponding to single frequency modes.

Stabilizing the injection locking is extremely cumbersome because each time the injection lock is lost one must manually adjust the slave diode current to regain the optimal injection point. If the injection is repeatedly lost on the scale of minutes then this could become a major impediment to successfully running experiments with the injection locked light. For this reason, we implement a protocol for active stabilization of the injection lock.

The hysteresis in the injection locking signal presents an added difficulty to imple-

menting a stabilization protocol. Since full injection locking can only be achieved by approaching the optimal diode current point from above, standard PID algorithms, which rely on a linear relationship between an error signal and control input, cannot be used. If the PID overshoots the optimal current point, then it will be unable to regain the injection lock, since the injection lock point cannot be approached from below.

Thus, we implement a stabilization protocol, based on a scheme described in Ref. [68], which is designed to overcome the inconveniences of the hysteresis loop. The protocol uses the following sequence: (1) A Labview program continually scans the piezo voltage of the Fabry-Perot cavity, through an FPGA output. (2) The transmission through the cavity is monitored on a photodiode and fed as an FPGA input into the program, and the peak height of the injection locking signal is continually recalculated as the maximum photodiode signal from the scan. (3) We define a threshold peak height, such that a peak height above the threshold is consistent with a full injection locking signal, and a peak height below the threshold is consistent with either no or partial injection locking. (4) If the peak height is above the threshold the protocol does nothing; however, if the peak height falls below the threshold then the program will implement a recovery protocol. In the recovery protocol, the slave diode current is jumped up approximately 2 mA (so that the partial injection locking signal is reached from the increasing current side), then decreased in intervals of approximately 0.1 mA until the peak height is again above threshold.

Fig 2.5 shows the peak height as a function of the slave diode current in the region near one of the optimal current points for injection locking. It is evident that there is an approximately 0.2-0.3 mA wide plateau where full injection locking is satisfied. Furthermore, we see on the higher current side of the plateau there is a gradual decrease in the peak height, corresponding to the partial injection locking region;

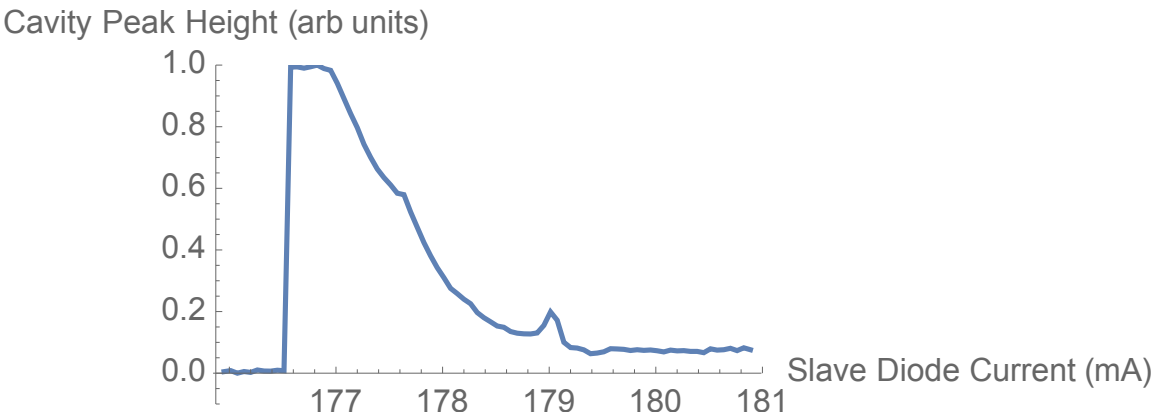

Figure 2.5: A plot of the cavity peak height as the slave diode is decreased. The plateau region identifies the region of full injection locking. The hysteresis of the injection locking is evident as the right side of the plateau is characterized by a declining slope in the cavity peak height, corresponding to a region of partial injection locking, while the left side of the plateau is characterized by a rapid drop to no injection locking.

whereas, on the lower current side of the plateau there is a sharp drop to no peak height, corresponding to a broad emission spectrum from the slave diode laser. The threshold peak height is defined at approximately the height of the plateau.

2.2.2 Locking

For initial experimental implementation we locked the blue laser using a saturated absorption spectroscopy technique, with a signal generated using Yb vapor from a hollow cathode lamp. However, upon purchase of a Stable Laser Systems ULE Cavity we locked using a transmission signal from the cavity.

Hollow Cathode Lamp

To generate a saturated absorption signal for the Yb singlet transition we take approximately 7 mW of light from the master laser for the spectroscopy setup. A polarizing beamsplitter is used to give variable control over the relative powers in the pump and probe beams. The probe beam is transmitted through the PBS and

is then directed through a Yb hollow cathode lamp, which contains an atomic vapor of Yb. We find that the saturated absorption signal is maximized when the power in the pump (probe) beam is 6 mW (1 mW). Since the beam diameter is ∼3 mm, the pump beam is close to the saturation intensity for the singlet transition (∼ 60 mW/cm^2).The transmitted probe beam is then transmitted through another PBS and the signal is read on a photodiode. The pump beam is reflected off the first PBS; then, two mirrors and the reflected path of the second PBS are used to align the pump beam in the counter-propagating direction of the probe beam.

An error signal from the transmission signal of the probe beam is generated by modulating the laser frequency at a modulation frequency of 250 kHz, as the laser frequency is scanned through the Yb singlet atomic resonance, to generate a derivative of the SAS signal. The absolute laser frequency is then locked to the zero-crossing of the error signal.

Stable Laser Cavity

We transition to locking the blue laser via a transmission signal from a ULE Stable Laser Systems cavity. Similar to the saturated absorption signal scheme, the error signal is generated by modulating the laser frequency at 250 kHz to generate a derivative of the transmission signal. After a few months of operating with the SLS cavity we began to observe issues where the resonance of the cavity would experience jumps on the scale of a 1 MHz (this was measured from measuring the resonance of the $^3P_1$ state via fluorescence imaging). While the cavity resonance will slowly drift on the scale of ∼10 kHz per day these sorts of instantaneous jumps in the resonance are unexpected. Furthermore, we noticed in measuring the transmission of 556 nm light in the cavity that the cavity finesse at that wavelength had degraded.

There has been discussion in the literature that suggests vacuum-induced degradation of dielectric mirror coatings can cause the degradation of cavity finesse [69]. We also

theorize that high powers of near-UV 399 nm light could cause damage to the mirror coatings [70]. Ref. [69] shows that damage to the mirror coatings can be reversed by flooding the vacuum chamber with oxygen and illuminating the mirrors with light at 422 nm. We follow this technique (illuminating with 399 nm light instead) and observe a ∼6x improvement in cavity finesse at 556 nm. To prevent damage to the mirror coatings from 399 nm in future use we generate our transmission signal using very low 399 nm powers (∼100 nW), measuring transmission with a Si APD (Thorlabs APD430A) to achieve good signal to noise. After this change we have not observed large resonance jumps in the cavity for almost 2 years of operation.

2.3 Green Laser System

Engineering a highly stable and low-linewidth laser system at 556 nm is necessary for exciting the narrow ($\Gamma = 2\pi\times$ 182 kHz) intercombination line of Yb. This laser system is crucial for a four main applications in our experiment: 1) The scattering force from the transition is used to push atoms across the chamber from the 2D MOT to the science cell. 2) It is responsible for the second stage of laser cooling in a narrow-line 3D MOT in the science cell. 3) Cycling on the intercombination line allows for simultaneous Doppler cooling and photon scattering for single atoms in optical tweezers, enabling high-fidelity imaging of single atoms. 4) Excitation to Rydberg states is done through a two-photon process using $^3P_1$ as the intermediate state. Fig 2.6a shows the optics setup for delivering 556 nm light for each application.

2.3.1 Sum Frequency Generation

We generate 556 nm light using a sum frequency generation technique, where we combine pump light at 1563 nm fiber laser and probe light at 862 nm. The pump light comes from a high-power (10 W) EDFA fiber laser (Koheras Boostik). The

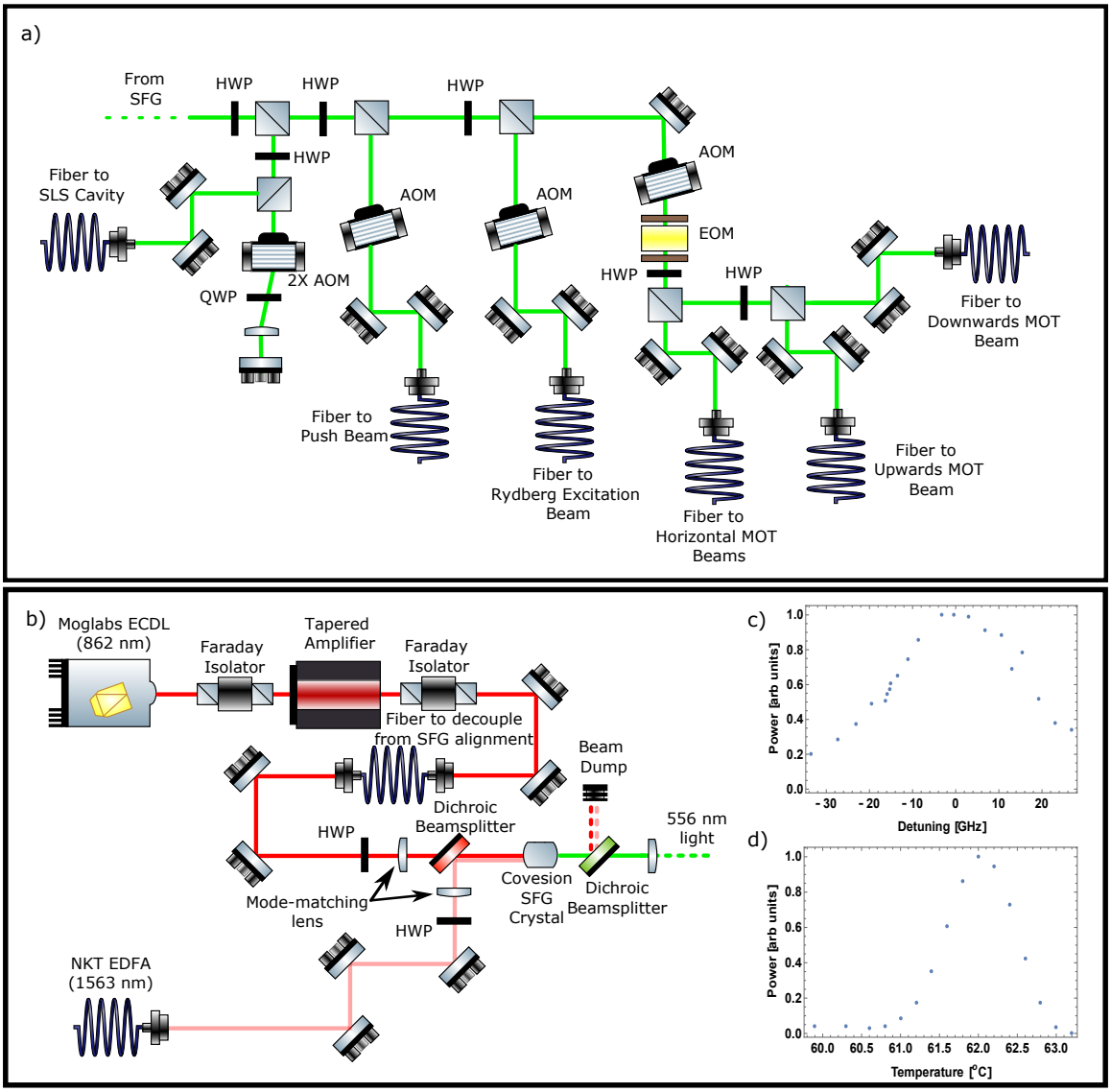

Figure 2.6: a) A schematic of the optics for the 556 nm laser system. b) A schematic of the optics for the sum frequency generation process to produce 556 nm light. c) Dependence of the sum frequency conversion efficiency on the frequency of the pump laser at a fixed temperature. d) Dependence of the sum frequency conversion efficiency on the temperature of the PPLN crystal at fixed frequency.

probe light is generated by sending light from an ECDL (Moglabs cateye ECDL) through a tapered amplifier (Dilas), which generates ∼2 W of light at 862 nm. The sum frequency generation process occurs through a non-linear process in a PPLN (Periodically Poled Lithium Niobate) crystal (Covesion).

The crystal (40 mm length) is housed in an oven which allows temperature tuning

and stabilization in order to maximize the efficiency of the sum frequency generation process through mode-matching. Fig 2.6c,d show the frequency and temperature dependence of the sum frequency generation output efficiency. To achieve optimal sum frequency efficiency it is recommended in Ref. [71] that each beam is focused into the PPLN crystal using focusing parameter, $l/b = 2.84$, where $l = 40$ mm, is the length of the PPLN crystal, and $b = \frac{2\pi}{w_0^2}$ is the confocal parameter. This condition requires 45 μm and 60 μm beam waists, for the 862 nm and 1562 nm light respectively. In choosing lenses to achieve these beam waists inside the PPLN crystal it is necessary to take into account the refractive index of the crystal. The focused beams are spatially overlapped using a dichroic beamsplitter at the input of the PPLN crystal. Furthermore, half-waveplates are used for both beams to get the appropriate polarization for the sum frequency generation process. Another dichroic beamsplitter is placed at the output of the PPLN crystal to separate out any leakage of 862 nm and 1563 nm light from the generated 556 nm light. Fig. 2.6b shows a diagram of the optical setup for sum frequency generation process.

The efficiency of the sum frequency generation process is generally quoted in units of %/(W $\cdot$ cm), where Efficiency $= \frac{P_{556}}{P_{862} \cdot P_{1563} \cdot L_{\mathrm{PPLN}}}$. We achieve a sum frequency generation efficiency of 3% $(\mathrm{W} \cdot \mathrm{cm})^{-1}$, which is consistent with previously achieved efficiencies [72], and allows us to generate $\sim$250 mW of 556 nm light.

2.3.2 Locking

We lock the green laser frequency with a Pound Drever Hall (PDH) error signal generated via a reflection signal from 556 nm light input to the SLS cavity [73]. We use a homebuilt EOM driven at 18.3 MHz to apply the two frequency sidebands. In order to lock the frequency of 556 nm light to the desired frequency the PDH error signal is used for active frequency stabilization of the 862 nm ECDL used for sum frequency generation of the green light. We note that for driving high coherence

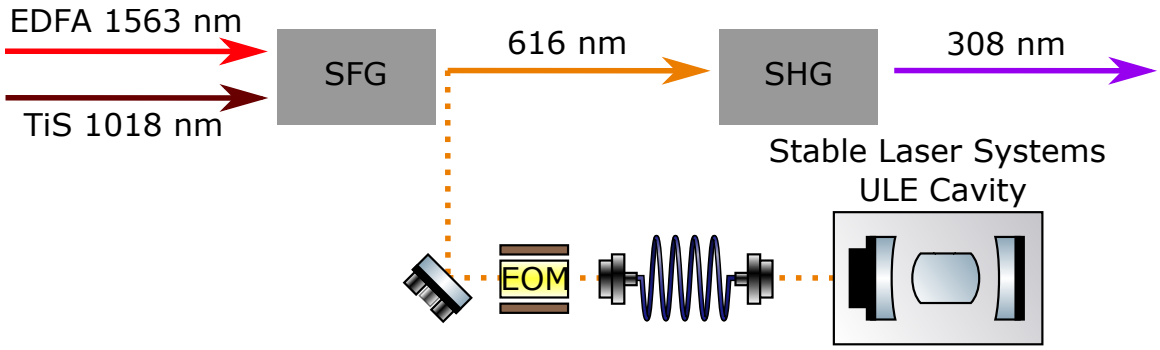

Figure 2.7: A diagram of the process for generating and locking 308 nm UV light for Rydberg excitation. First 616 nm orange light is generated via a SFG process in a PPLN crystal. The orange light is then frequency doubled in a bow-tie configuration doubling cavity with a BBO crystal. A second path of the orange light is sent through a Fiber EOM, to which we apply tunable sidebands that allow us to frequency stabilize the UV light over a very large tunable frequency range by using a PDH error signal generated from a reflection signal of the optical sideband from the SLS cavity.

Rydberg Rabi oscillations the frequency noise of the ECDL laser lock is too high (linewidth of a few 100 kHz) so we replace the ECDL with a Titanium-Sapphire (Ti:Sa) laser (M-Squared), which we operate at 862 nm. In this scheme we also use the PDH error signal to stabilize the frequency of the Ti:Sa laser. While the SLS ULE cavity resonances are highly stable they can undergo slow drifts on the order of roughly 10 kHz a day. At the week-long time scale these drifts can be on order as large the $^3P_1$ linewidth. Thus, it is often necessary to slightly tune the RF frequency of the AOM, which sends locking light to the cavity, in order for the experimental light to remain at the right frequency relative to the atomic transition.

2.4 UV Laser System

We generate 308 nm light for Rydberg excitation in a two-step process. First we use the same SFG process that we use to generate 556 nm light to generate orange light at 616 nm. Second we use a doubling cavity to convert the orange light to the desired UV frequency.

2.4.1 Sum Frequency Generation

The method for sum frequency generation is identical to the one described for the green laser system. Here we used an identical 10 W pump source (fiber laser model) and for the probe source we use light from a Ti:Sa (M-Squared) at $\sim$ 1018 nm. The Ti:Sa generates $\sim$1.3 W at this wavelength allowing us to achieve 616 nm powers of $>$500 mW ($\sim$3% $(\mathrm{W} \cdot \mathrm{cm})^{-1}$). Notably, the wavelength of the Ti:Sa is highly tunable allowing us to access any Rydberg state with principal quantum number greater than $\sim$30. This tunability both allows us to perform spectroscopy over a wide range of Rydberg levels and access any desired Rydberg states for quantum science applications.

2.4.2 Second Harmonic Generation

For our initial generation of UV light, we generate 308 nm light via a second harmonic generation (SHG) process in a Brewster cut nonlinear BBO crystal [74] within a homebuilt bow-tie configuration doubling cavity [75]. The cavity resonance is actively stabilized via feedback on an error signal generated by the Hansch-Couillaud method [76].

After operation of the cavity for a couple months we began to experience an issue where after optimizing the SHG conversion efficiency through internal alignment of the cavity and BBO crystal, the output power of the doubling cavity continuously drops over the scale of a few hours (shown in Fig. 2.8a). Interestingly, the drop in the SHG efficiency of the cavity has a strong wavelength dependence. Fig. 2.8b shows the output power of the doubling cavity as a function of the wavelength of the TiSa used as the probe beam in the orange SFG process. We observe a feature $\sim$ .04 nm in width centered at the wavelength, where the power output degradation initially occurred. Furthermore, when we change the wavelength away from where

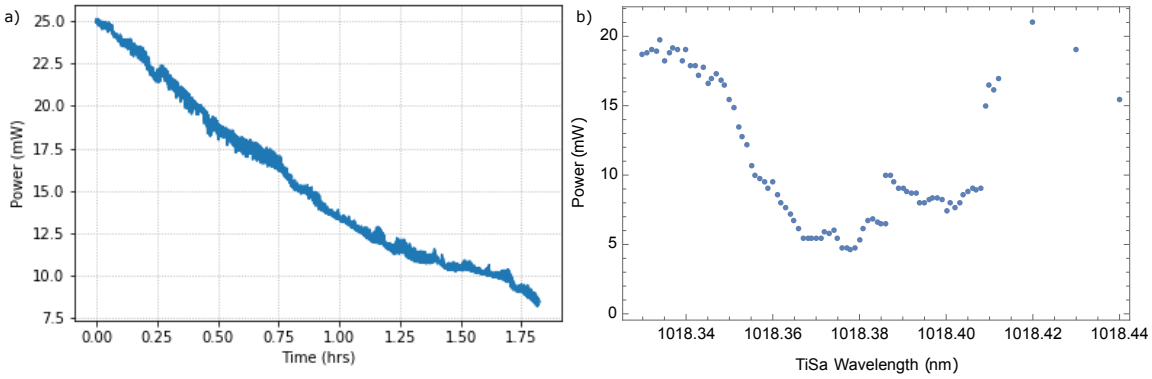

Figure 2.8: a) Output power of the UV doubling cavity over time. We observe a continuous and steady drop over the time-scale of a few hours. b) Dependence of UV output power on TiSa wavelength showing strong frequency dependence of output efficiency degradation, centered at the wavelength where the degradation occurred.

the degradation occurred it initiates a similar output power degradation process at the new wavelength and over a similar time-scale the output power at the original degraded wavelength will return to prior non-degraded efficiencies. Another way to reverse the degradation is to translate the BBO crystal so that the 616 nm light propagates through the BBO crystal at a different location on the crystal.

We theorize that what we are observing is a consequence of a photorefractive effect induced in the BBO crystal [77], where a standing wave of a given wavelength of light induces a periodic refractive index in the crystal. This periodic refractive index leads to an effective diffraction grating seen by the light as it propagates through the BBO crystal, which consequently can cause back-reflection and a reduction in cavity finesse, leading to the drop in output efficiency. Under this hypothesis, changing the wavelength of the input light leads to the effective diffraction grating being out of phase with the light removing the drop in output efficiency. The spectral width of the drop in efficiency is roughly consistent with what one would expect from the length of the BBO crystal. As further evidence of this hypothesis, changing the temperature of the crystal, which in turn changes the index of refraction in the crystal making the

effective grating similarly ineffective, reverses the degradation of the cavity efficiency.

Eventually, we upgraded our doubling cavity to a commerical doubler from LEOS and no longer observe this issue. With the LEOS cavity we can generate > 100 mW of UV light with approximately 500 mW of input orange light. Notably, the doubling efficiency of the cavity is quadratic in the input power so any gains in orange power output should lead to large gains in UV power output.

2.4.3 Locking

We lock the UV laser frequency with a Pound Drever Hall (PDH) error signal generated via a reflection signal from orange 616 nm light input to the SLS cavity [73]. The orange light is first sent through a fiber EOM where we apply tunable sidebands at a frequency of a few GHz. Importantly, the tuning range of the sideband frequency is greater than the free spectral range of the SLS cavity (1.5 GHz), which allows us to lock the UV light at arbitrary frequencies. This capability is important for being able to explore and utilize the full range of Rydberg states. A PDH error signal, from the optical sidebands, is generated using a different homebuilt EOM than in the green locking setup (driven at a different modulation frequency so both signals can be read from the same photodiode in reflection), and used for active feedback on the frequency of the Ti:Sa laser, operating at 1018 nm, used in sum frequency generation of the 616 nm orange light.

2.5 2D MOT

A common technique for atomic physics apparatus which require powerful laser cooling forces for a hot atomic vapor and the ability to generate a high flux of laser-cooled atoms is a Zeeman slower [78]. While Zeeman slowers often achieve state of the art laser-cooled atomic fluxes, they come with drawback of requiring a large amount of

space and substantial engineering of magnetic field coils. An alternative and more compact approach is an initial stage of laser cooling from a hot atomic vapor with a 2D MOT coupled with a push beam to transfer a flux of cold atoms to the science chamber [79].

For the design of our 2D MOT we closely follow the design from [80]. The 2D MOT beams consist of two perpendicular input beams each oriented at 45 degrees relative to the transverse push beam axis. The beams are input at the bottom windows of a cross in the vaccuum chamber and are each individually retroreflected at the corresponding upper windows of the cross. Due to the high saturation intensity of the $^1S_0 \rightarrow {}^1P_1$ transition (60 mW/cm^2), we require high optical powers in each beam to maximize the cooling force of the beams. Using light from the injection locked slave laser described in Section 2.2, we can achieve ~ 40 mW per beam.

In choosing the beam waist, w_0, of the 2D MOT beams we aim to maximize the capture velocity, v_c, in order to maximize the fraction of atoms we can capture from the hot atomic beam coming from the oven. There are two competing scalings to consider: (1) Larger beam waists allow the beams to exert a cooling force over a larger distance and longer time thus leading to a higher capture velocity ($v_c \propto w_0$). (2) A smaller beam waist leads to a higher saturation parameter ($s \propto 1/w_0^2$), which in turn leads to a higher capture velocity ($v_c \propto \frac{s}{s+1}$). Notably, in the regime where the saturation parameter is much greater than 1 (i.e. the intensity is far above the saturation intensity) then one gains from making the beam waist as large as possible. However, as mentioned above, the high saturation intensity of this transition means we operate well below this regime. Thus, we operate at a compromise between these two considerations and use a beam waist of $w_0 \approx 0.7$ cm.

In order to engineer a truly two-dimensional trapping force we need to engineer a magnetic field environment such that there is a gradient in the plane of the MOT

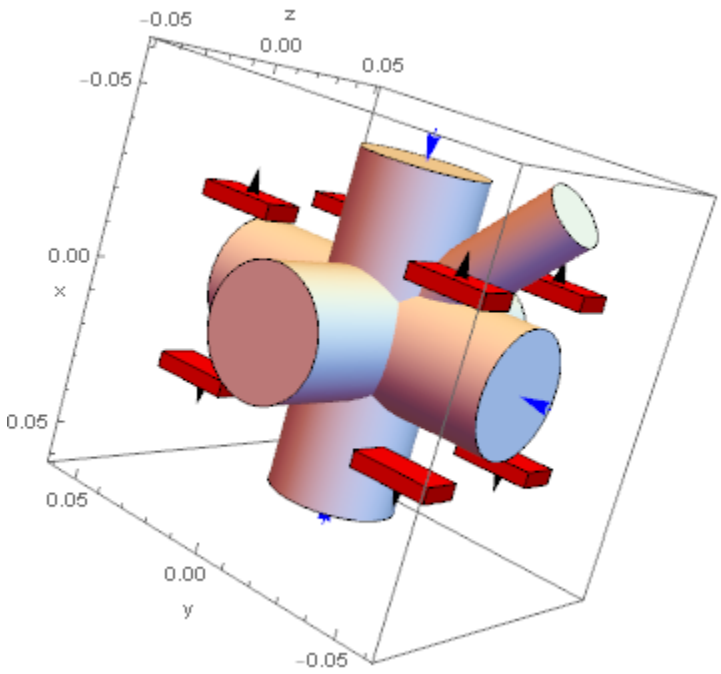

Figure 2.9: Configuration of magnets to achieve desired magnetic field gradients for 2D MOT. The tubes with blue arrows at the edges represent the axis of the MOT beams.The push beam is along the Z axis, and the small tube is the oven. The arrows on each magnet (red rectangular blocks) indicate its polarity.

beams, but no gradient in the transverse dimension. We achieve this with the configuration of magnets shown in Fig. 2.9. Each magnet in the figure represents 3 1/8" permanent magnets stacked together. Two stacks of magnets are mounted on either end of four 3D printed plastic mounts (for a total of 8 magnet stacks), which are in turn each fastened to a tube on the vacuum chamber to position the magnets in the proper positions relative to the intersection of the 2D MOT beams. We calculate magnetic field gradients of ~ 80 G/cm in the plane of the MOT beams (x and y axes in Fig. 2.9) and a transverse gradient (z axis in Fig. 2.9) of less than 1 G/cm.

A flux of hot Yb atoms are directed through the nozzle array at the end of our Yb oven (described in Section 2.1) in the plane of the 2D MOT beams to be trapped at the intersection of the MOT beams. Fig. 2.10a shows an image of the fluorescence from the 2D MOT. One can see a cross of blue fluorescence from atoms fluorescing

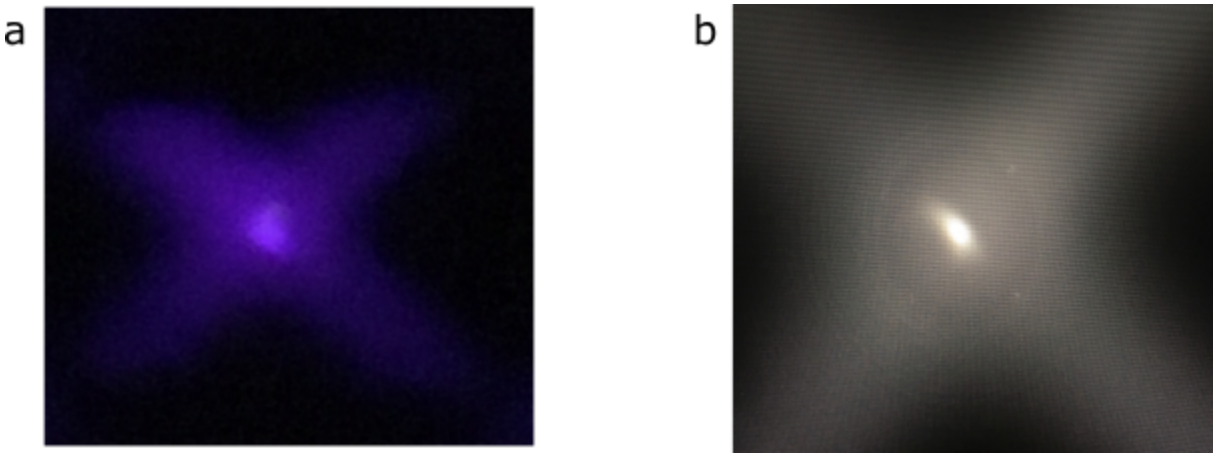

Figure 2.10: a) An iPhone camera image of the fluorescence from the 2D MOT beams. b) Fluorescence image taken through imaging telescope lens onto Thorcam camera used to monitor 2D MOT and estimate fraction of fluorescence in trapped region. Circular outline behind MOT is the differential pumping tube.

in the MOT beams, which are not trapped in the 2D MOT, and a brighter spot of fluorescence at the center of the beams which comes from the trapped atoms. We estimate the steady state number of atoms trapped in the 2D MOT by measuring the power of fluorescence collected by a lens from the window where the push beam enters the chamber. The expected power per atom is $P = \Gamma \frac{s}{s+1} \frac{\text{solid angle of lens}}{4\pi} \frac{hc}{\lambda}$. We then analyze an image of the fluorescence (shown in Fig. 2.10b) to determine what fraction of the fluorescence comes from the trapped atoms compared to the untrapped atoms fluorescing in the MOT beams. This allows us to estimate, at an oven temperature of 400 °C, that we have a steady state of ∼500,000 atoms in our 2D MOT.

2.6 Push Beam

We use a push beam, which applies a scattering force via the $^1S_0 \rightarrow {}^3P_1$ transition, to transfer atoms from the 2D MOT across the differential pumping stage of the vacuum chamber to the science cell, where they can be trapped in a narrow-line 3D MOT. An important consideration in designing both the vacuum chamber and the logistical function of the push beam is that due to the narrow linewidth of the

intercombination line ($\Gamma = 2\pi\times$ 182 kHz), the cooling force of the narrow-line MOT is relatively weak and thus the MOT will have a low capture velocity. For example, assuming a maximum scattering force on $^1S_0 \rightarrow {}^3P_1$ transition (a = 2.4 $\times 10^3$ m/s^2) and a MOT beam diameter of 1 cm would suggest a capture velocity of $v_c \approx 7$ m/s for the narrow-line MOT.

It is necessary to to push the atoms across the vacuum chamber at a velocity below the 3D MOT's capture velocity. Due to the slow capture velocity of the narrow MOT, and the distance that the atoms must be pushed from the 2D MOT to the center of the science cell ($\sim$0.4 m), gravitational forces will have a non trivial effect on the trajectory of the atoms while they traverse the vacuum chamber. In the time it would take to travel 0.4 m at 7 m/s an atom with zero initial velocity in the direction of gravity would drop 1.6 cm over the course of its trajectory. This distance is greater than the radius of a window in the science cell and thus it is infeasible to design the vacuum chamber such that the center of the science cell (i.e. the position of the 3D MOT) is collinear with the 2D MOT position.

In order to account for gravitational sag during the travel time of the atoms across the vacuum chamber we design the 2D MOT section of the vacuum chamber and the differential pumping tube to be at $\sim 7^\circ$ angle relative to the science cell, which is parallel to the optical table. The push beam pushes the atoms along the axis of the differential pumping tube supplying them with both the horizontal velocity to push them across the vacuum chamber and a slight upwards vertical velocity to counteract gravitational sag. The angle is chosen such that the trajectory of atoms pushed at a velocity of 5.5 m/s (chosen to be safely below the capture velocity of the 3D MOT) will intersect with the center of the science cell. A schematic of the atom trajectory is shown in Fig. 2.11.

Due to the finite Doppler temperature of atoms in the 2D MOT ($T_D \approx 700\mu$K), there

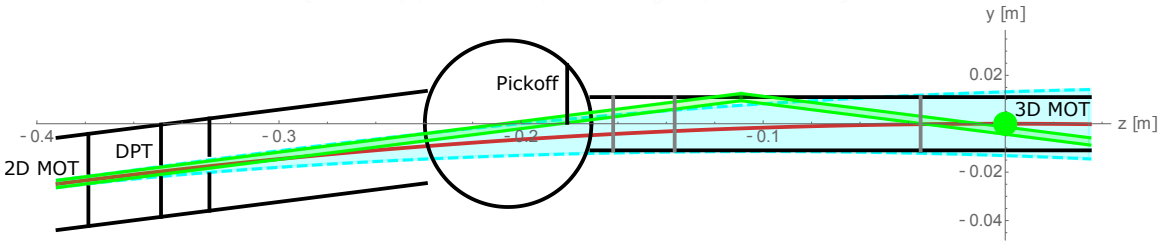

Figure 2.11: A schematic of the trajectory of pushed atoms across the chamber with mean pushing velocity of 5.5 m/s and T = 700μK. The atoms begin in the 2D MOT and the scattering force of the push beam (green trace) pushes the atoms through the differential pumping tube (DPT) at an angle of $\sim 7°$ relative to the science cell. The red trace shows the mean atom trajectory, while the light blue region shows the atom trajectories for atoms with an initial vertical velocity within 1σ for the Boltzmann distribution with T = 700μK. The push beam is picked off by a pickoff mirror in the differential pumping stage of the vacuum chamber (circular region), however, we display the path of the push beam if it were not picked off. The green circle shows the region of the 3D MOT beams to demonstrate the overlap of the pushed atomic cloud with the desired trapping region.

will be a Boltzmann distribution of initial velocities in the plane transverse to the pushing direction, causing the atomic cloud of pushed atoms to expand during the trajectory across the chamber. The red trace in Fig. 2.11 shows the mean trajectory of atoms pushed at 5.5 m/s, while the light blue region contains the trajectories of atoms with initial vertical velocities within 1σ for a Boltzmann distribution with $T = 700\mu$K. Given the atomic cloud expansion we predict $\sim 7\%$ of pushed atoms will intersect with MOT beams of 1 cm and be captured by the 3D MOT.

Furthermore, we install a pickoff mirror before the entrance to the science cell to reflect the push beam out of a side window of the differential pumping section of the vacuum chamber. Given the divergence between the push beam path and mean atom trajectory due to gravitational sag of the atoms, the pickoff mirror does not block atoms whose paths will intersect with the 3D MOT beams. The ability to pickoff the push beam is attractive so that the light, which is resonant with the $^1S_0 \rightarrow {}^3P_1$ transition, will not disturb atoms in the science cell.

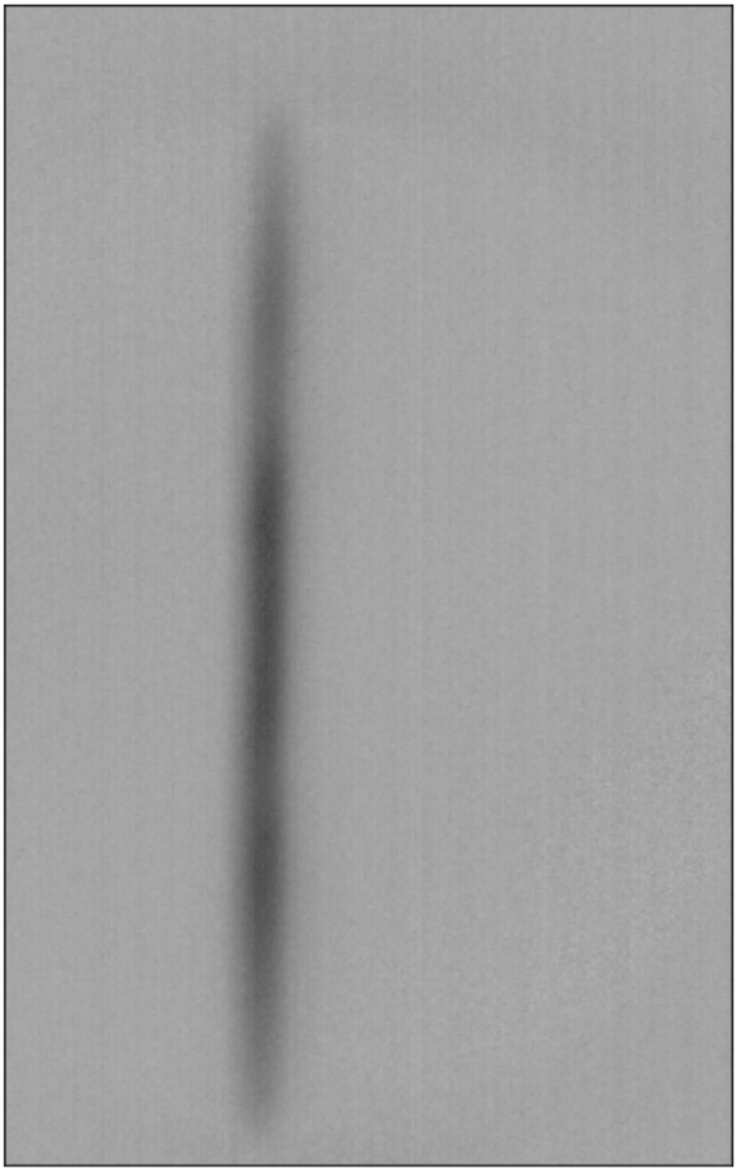

Figure 2.12: An image of fluorescence (dark streak) of pushed atoms from a probe beam on the $^1S_0 \rightarrow {}^1P_1$ propagating transversely to the pushing direction in the metal chamber directly after the differential pumping tube.

In order to characterize the performance of the push beam we image fluorescence from pushed atoms (shown in Fig. 2.12) excited by a probe beam resonant with the broad $^1S_0 \rightarrow {}^1P_1$ propagating transversely to the trajectory of the atoms. The probe beam enters the vaccuum chamber through a small window on the top of the region directly after the differential pumping tube. To estimate the velocity of the atoms we pulse on

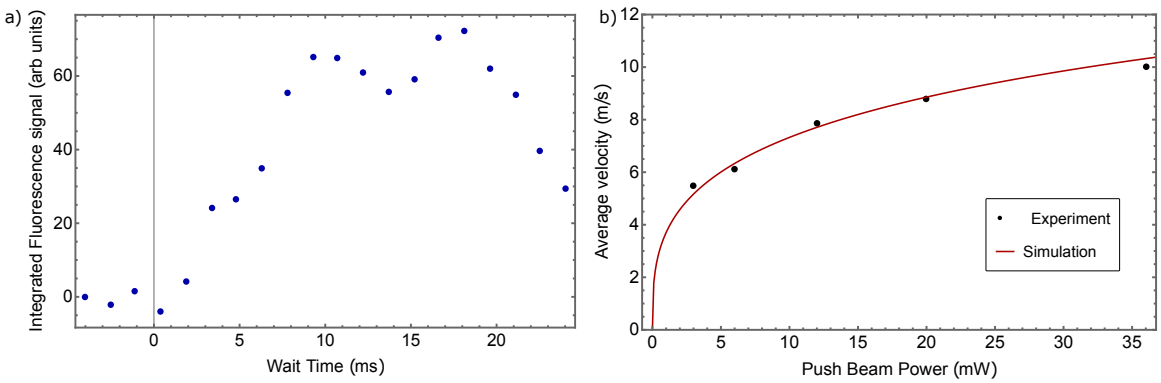

Figure 2.13: a) A measurement of the integrated fluorescence signal from the 0.5 ms probe beam pulse as a function of the wait time after the 20 ms push beam pulse is turned off (negative wait times refer to the probe beam being turned on while the push beam is still on). We can infer the velocity distribution of the pushed atoms from the rising edge of the signal and the known distance between the 2D MOT and the probe beam. b) The average pushed velocity as a function of the push beam power. The red curve shows the theoretical expectation of the average pushed velocity based on a simulation of the scattering force from the power broadened transition.

the push beam for 20 ms and then pulse on the probe beam for 0.5 ms at varying delay times and measure the integrated fluorescence signal collected from atoms scattering via the probe beam. Given a known distance between the 2D MOT and the probe beam we can infer the velocity distribution by the measured fluorescence as a function of the wait time after the atoms are pushed. A representative measurement is shown in Fig. 2.13a. The wait time is from the end of the 20 ms push beam pulse so negative wait times suggest that the probe beam is pulsed on while the push beam is still on. We first start to see a fluorescence signal at 2-3 ms after the end of the push beam pulse (22-23 ms after the start of the pulse) and then see the fluorescence signal rise to a maximum at 30 ms after the push beam is turned on. Finally the signal begins to drop which corresponds to the entire pushed cloud of atoms passing by the region of the probe beam before the probe beam has been turned on.

Given the design of the vacuum chamber at a specific angle it is crucial that we have fine control over the velocity we push the atoms at. Due to the narrow linewidth of the $^1S_0 \rightarrow {}^3P_1$ transition, there is also a narrow velocity range ($v = \frac{\Gamma}{k} \approx 0.1$ m/s)

over which atoms will not be Doppler shifted out of resonance with the push beam. That is, if we illuminate the push beam on resonance with the atoms after the atoms are accelerated to a velocity such that $kv > \Gamma$ they will be Doppler shifted out of resonance with the push beam and the scattering force of the push beam on the atoms will become exceedingly small. However, if we power broaden the transition ($I_{\text{sat}} \approx 0.14$ mW/cm^2) then the maximum velocity at which the scattering force of a resonant beam will be felt by the atoms will grow. If the push beam is operated at a saturation parameter, s, then the maximum velocity the atoms will be accelerated to will be $v_{max} \propto \frac{\sqrt{s}\Gamma}{k}$. Thus we can have fine control over the average velocity of the pushed atoms by simply changing the operating power of the push beam. Fig. 2.13b shows the average measured velocity as a function of push beam power and the simulated pushing velocity from the scattering force.

Finally, we can use the image of the fluorescence to estimate the number of photons collected and infer from the scattering rate of the probe beam ($\Gamma = 2\pi \times 29$ MHz) and the velocity of the atoms, the flux of pushed atoms, which we estimate to be 6 $\times 10^7$ atoms/s, at an oven temperature of 410 °C, measured directly after the differential pumping tube.

2.7 3D MOT

The final stage of laser cooling in our experiment is a 3D narrow-line MOT on the $^1\text{S}_0 \rightarrow {}^3\text{P}_1$ transition ($\Gamma = 2\pi \times 183$ kHz, $T_D = 4.4\mu$K) in the vacuum chamber science cell, which captures and cools atoms pushed across the chamber by the push beam. There are two retro-reflected beams in the parallel plane of the science cell, each at 45 degrees relative to the propagation direction of the pushed atoms. The vertical MOT beams consist of two separate beams, an upward propagating beam, and a downward propagating beam, which is sent through the microscope objective (NA = 0.6) used

to project the optical tweezers into the science cell. The high NA of the microscope objective makes it difficult to engineer a large collimated beam out of the objective, so the downward propagating beam has a smaller beam waist ($\sim$2 mm) than either the horizontal beams or the upwards vertical beam (1 cm). Since the vertical beams are not in a retro-reflected configuration, and have different beam waists it is necessary to operate them at different powers in order to have balanced cooling forces in the vertical direction of the MOT.

A magnetic field gradient is achieved via identical coils positioned on the top and bottom of the science cell with counter-propagating currents. These coils are calculated to achieve magnetic field gradients of 0.96 (G/cm)/A in the axial direction and 0.48 (G/cm)/A in the radial direction. We operate the MOT with a current of $\sim$4 A in the gradient coils. Due to the small magnetic field gradients necessary for operating the narrow-line MOT (a few G/cm) it is necessary to have a high degree of control over the stray magnetic field environment since stray fields of a few Gauss could move the null field point of the field gradient outside of the region of the MOT beams, causing the trapping of the MOT to cease to work. In order to achieve this control we add three pairs of bias coils oriented in three perpendicular axes to allow us to control the field environment at the center of the MOT beams. Notably, we spent many weeks trying to observe a 3D MOT before the installation of bias coils and were unable to until the bias coils were installed.

The coils are fabricated out of 16 AWG magnet wire, wrapping around 1/2" Thorlabs posts screwed into a breadboard. The breadboard was a custom-machined aluminum plate with hole patterns for the exact desired coil sizes. We applied Epotek T7110 epoxy after every layer, and cured the entire plate assembly on a hotplate for 1.5-2 hours or overnight. The hotplate was set to 250C, but the plate temperature appeared to be around 100 C as measured with IR thermometer. For the last few coils, we

discovered that using a sheet of vacuum bag material to line the breadboard is the easiest way to remove the coils. Also, to maintain the desired outer dimensions, we hammered on the sides of the coil with a wooden block and mallet to flatten them out. Doing this during the coil winding is dangerous as it can impact the layer stacking, but doing it afterwards is just as effective. There are eight coils: two each for X,Y,Z bias fields and two for the quadrupole field gradient. However, to save space and curing time, the quadrupole and z coils are wound together: the first three layers of this coil are the Z coil, and the next 6 layers are the quadrupole. A summary of the calculated magnetic fields at the position of the MOT for the geometry of each coil pair is shown in Table 2.1.

Coil Pair	Field/Current
X	7.5 G/A
Y	2.4 G/A
Z	4.3 G/A
Quadrupole	0.96 (G/cm)/A

Table 2.1: Theoretical calculation of magnetic fields given coil geometry.

In a given experimental sequence atoms are loaded into the 3D MOT and then transferred into an array of optical tweezers by projecting a tweezer array onto the cooled cloud of atoms. The loading process of the MOT is divided into two stages: a loading stage and a compression stage.

In the loading stage the MOT captures and cools atoms pushed across the chamber by the push beam. As discussed in the push beam section, due to the narrow linewidth of the intercombination line, the scattering force from this transition is only felt by atoms in a very narrow velocity class ($\sim$0.1 m/s) because of Doppler shifts. To maximize the cooling force and capture velocity of the MOT it is necessary to ensure that all atoms with velocity smaller than the incoming pushed velocity ($v \leq 5.5$ m/s) observe a scattering force from the transition. In the case of the push beam we overcame this problem by power broadening the transition, however, for the MOT beams we operate

with a larger beam waist so the power requirements of this method are much greater. As an alternative approach we engineer a multi-frequency MOT by sending all MOT light through a strongly-driven EOM (Qubig), which drives many sidebands spaced by 139 kHz, so that any atom with velocity below the capture velocity will feel a cooling force from one of the sidebands. We operate the center of the frequency comb at a detuning of $\Delta \approx -4$ MHz. It is important that all sidebands are red-detuned from resonance or else atoms will be heated and lost by the blue-detuned sidebands. The MOT beams are operated far above the saturation intensity at $\sim$20 mW per 1 cm horizontal beam in order to ensure that the power per sideband is above saturation.

Since we effectively broaden the cooling transition during the MOT loading phase the trapped atoms will not come close to reaching the low Doppler temperature ($T_D = 4.4\,\mu$K) of the transition. Thus, after a sufficient number of atoms have been captured in the loading phase, the MOT undergoes a compression phase, where the EOM sidebands are turned off, and the single-frequency of the MOT is ramped towards resonance until it reaches an optimal cooling detuning of $\Delta \approx -\frac{\Gamma}{2}$. Simultaneously, the power in the MOT beams is ramped down so that single-frequency MOT operates below the saturation intensity for optimal cooling. The ramping of the frequency and beam powers during the compression process occurs in 10 ms. The compression process has two main effects: first, the atoms are cooled considerably compared to their temperature during the loading phase, allowing them to reach near the Doppler temperature. Second, due to the atoms being considerably colder the relevant spatial extent of the MOT trapping forces also become considerably smaller. As a result the spatial extent of the MOT cloud, which is a few mm in diameter during the loading phase, is significantly reduced to $\sim 100\,\mu$m in diameter.

We characterize the temperature and density of the compressed MOT (cMOT) via absorption imaging on the broad $^1\mathrm{S}_0 \rightarrow {}^1\mathrm{P}_1$ transition. A probe beam with diameter

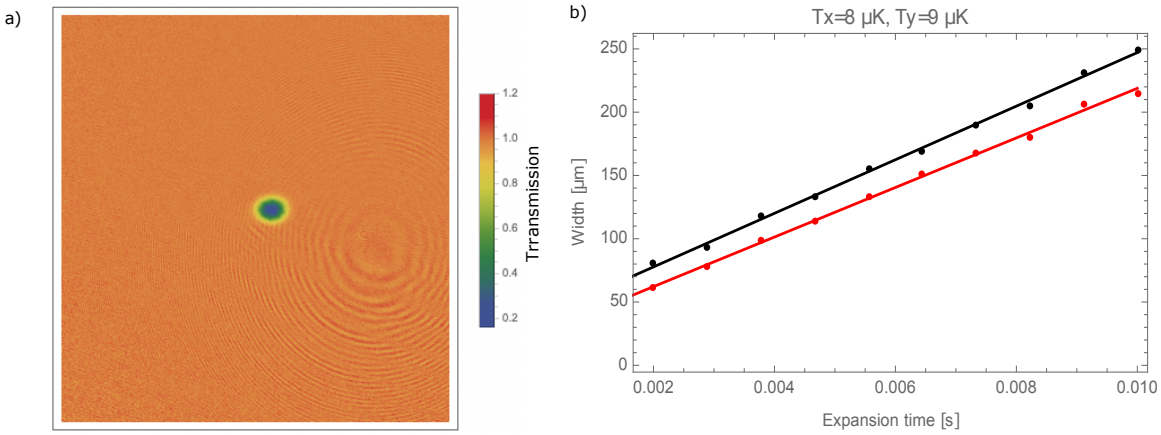

Figure 2.14: a) A characteristic absorption measurement of the cMOT. The orange corresponds to full transmission of the blue probe, while the small blue region corresponds to lower transmission due to absorption from atoms in the cMOT. b) A measurement of the atom cloud radius, via absorption imaging, as a function of the cloud expansion time. From the measured cloud radii we extract a cMOT temperature of 8 (9) μK in the horizontal (vertical) direction.

$\sim$7 mm and power $\sim$1 mW ($\sim$0.01 I_{sat}), is imaged on a camera and we measure the spatially-dependent dip in transmission to both infer the spatial distribution and density of the cMOT. To measure the temperature of the cMOT we perform time of flight measurements, where we turn off the MOT beams and then measure the width of the atomic cloud via absorption imaging at varying expansion times after the beams have been turned off. The rate of expansion is related to the average velocity of atoms in the cMOT, which in turn allows us to infer the temperature of atoms in the cMOT. Fig. 2.14a shows a characteristic absorption image and Fig. 2.14b shows a temperature measurement. We infer a temperature of roughly twice the Doppler temperature in both the horizontal and vertical direction of the cMOT. The absorption signal also allows us to infer a MOT loading rate of $\sim 10^6$ atoms/s. In the cMOT, for 1 s loading time, this corresponds to an atom density of $\sim 10^{12}$ atoms/cm^3.

Once the MOT has been loaded and compressed it is necessary to overlap it with the focus of the optical tweezers to load atoms from the cMOT cloud into the tweezers.

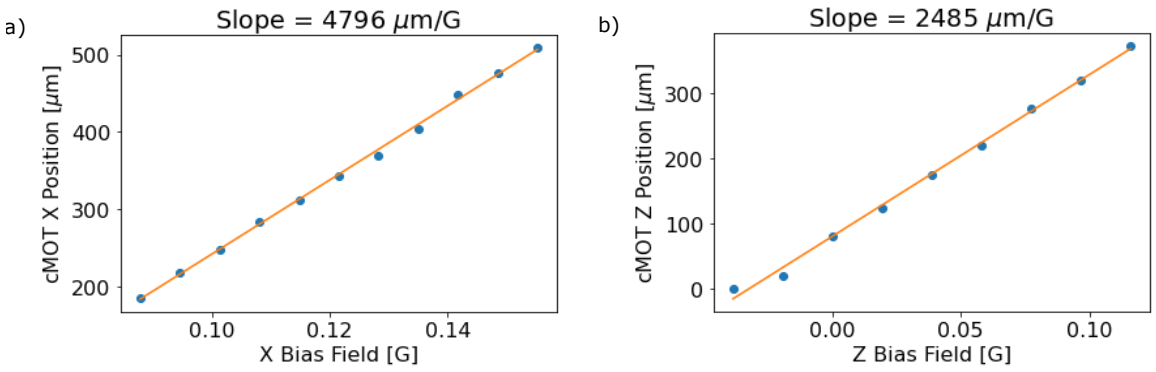

Figure 2.15: A measurement of the dependence of the cMOT position on the bias magnetic field in the a) X and b) Z directions. The roughly double slope in the X direction is consistent with the magnetic field gradient being twice as large in the Z direction. The zero point for the X and Z positions is arbitrary.

In order to accomplish this we can fine tune the position of the cMOT into the focus of the optical tweezers by tuning the field of the bias magnetic field coils. By tuning the bias field we change the null point of the field gradient and thus move the position of the cMOT. Fig. 2.15 shows the dependence of the position of the cMOT in the X and Z directions as a function of the bias field. The slope of the position dependence on bias field is approximately double in the X direction vs the Z direction, which is consistent with the magnetic field gradient being twice as large in the axial (Z) direction.

2.8 Optical Tweezers

Our trapping light for generating optical tweezers comes from a 12 W Verdi Laser at 532 nm. The light is sent through an AOM for the ability to rapdidly switch the tweezers on and off, and then coupled into a fiber which decouples the Verdi output from the alignment of the tweezer optical system. To generate 2D rectangular arrays of optical tweezers light is send through a vertical AOD followed by a 1:1 telescope, and then sent through a horizontal AOD followed by a 4x telescope to increase the beam size prior to entering a 0.6 NA Special Optics microscope objective

which focuses the array of optical tweezers into the science cell with a beam waist of $w_0 \approx 650$ nm. Prior to entering the objective the light passes through a dichroic beamsplitter, which transmits light at 532 nm, but reflects light at 556 nm and 399 nm. Fluorescence from atoms trapped in the tweezers is collected back through the same high-NA objective and reflected off the dichroic beamsplitter prior to entering a tube lens (200 mm) used to image the tweezer array on a low noise sCMOS camera (Photometrics Prime BSI). Fig 2.16 depicts a schematic of the tweezer optical system.

In order to load atoms from the 3D MOT into the optical tweezer array we must overlap the cMOT with the focus of the tweezers. As is described in Section 2.7 we can controllably move the position of the cMOT by changing the bias magnetic field in the science cell. To maximize tweezer loading we scan the loading probability of the array as a function of the bias field in all three axes. After atoms are loaded into the optical tweezers a 20 ms pulse red-detuned from the $^1S_0 \rightarrow {}^3P_1$ transition drives a light-assisted collision process, which ejects pairs of atoms and leaves each tweezer with either 0 or 1 atom [17, 51]. Finally we image single atoms by collecting fluorescence from driving the narrow $^1S_0 \rightarrow {}^3P_1$ transition (Further details on high-fidelity imaging of single Yb atoms in optical tweezers are described in Chapter 3). At optimal loading conditions the experimental cycle time is $\sim$200 ms, enabling rapid data collection.

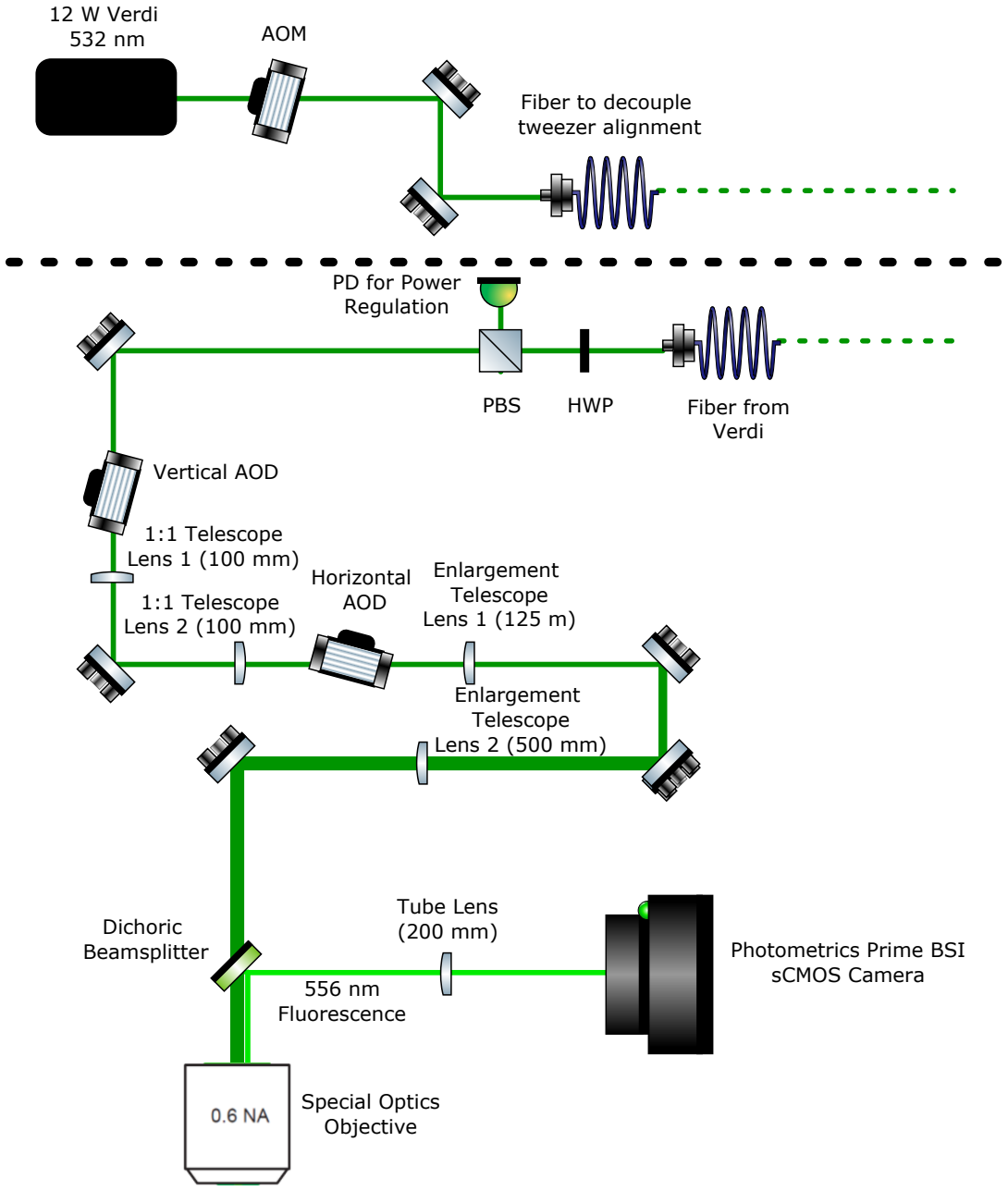

Figure 2.16: A schematic of the optical system for the tweezers and fluorescence imaging

Chapter 3

Trapping and Imaging ^{174}Yb in Optical Tweezers

Much of the work described in this chapter is also presented in Ref. [81]

In this chapter, we demonstrate an approach to produce large-scale arrays of individual alkaline-earth-like Yb atoms trapped in optical tweezers. Both cooling and imaging are performed on the narrow $^1S_0$-$^3P_1$ intercombination line ($\lambda = 556$ nm, linewidth $\Gamma_{556} = 2\pi \times 182$ kHz), enabled by the convenient "magic" trapping condition for these states with 532 nm trapping light [1]. The use of a narrow transition allows rapid cooling to temperatures of 6.4(5) μK, near the theoretical Doppler temperature of 4.4 μK for this transition. In contrast to most previous single-atom detection schemes relying on polarization gradient [17], Raman sideband [82, 83, 84] or EIT [85, 86] cooling during imaging, the narrow linewidth enables high fidelity imaging in shallow traps using Doppler cooling alone. Individual Yb atoms have previously been imaged in quantum gas microscope experiments using the strong $^1S_0$ transition at 399 nm ($\Gamma_{399} = 2\pi \times 29$ MHz), overcoming the high Doppler temperature (700 μK) by simultaneously cooling on the $^3P_1$ transition [1] or by using very deep (> 30 mK) op-

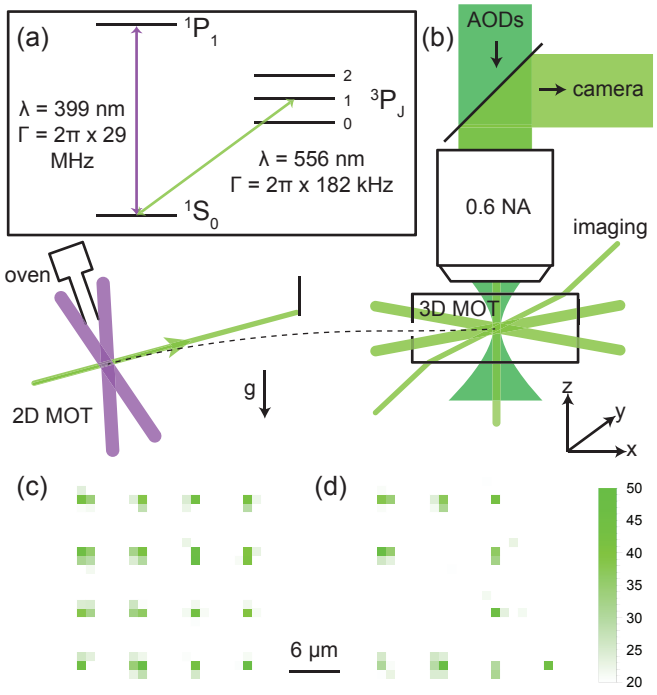

Figure 3.1: (a) Relevant energy levels for ^{174}Yb, with transition wavelengths (λ) and linewidths (Γ) indicated. (b) Diagram of experimental setup indicating the geometry of the cooling, imaging and trapping beams. Two of the 3D MOT beams are in the xy-plane, while the third propagates through the objective lens along the z-axis. The angled imaging beam is in the xz-plane. For other details, see text. (c) Average and (d) single-shot images of atoms in a 4x4 tweezer array, with 6 μm spacing (35 ms exposure time). The color bar indicates the number of detected photons on each pixel.

tical potentials without cooling [87]. The present technique is the first to demonstrate very high-fidelity, low-loss imaging in shallow traps, as required for rearrangement-based generation of uniformly filled tweezer arrays. As an outlook, we demonstrate a 144-site (12x12) tweezer array, stochastically loaded with atoms.

3.1 Light Shifts and Magic Conditions

To characterize the cooling and imaging properties of the 556 nm transition, we first measure the differential light shift of the $^1S_0$ and $^3P_1$ states in the optical tweezers (Fig. 3.2a). In the absence of a magnetic field and with linearly polarized trapping

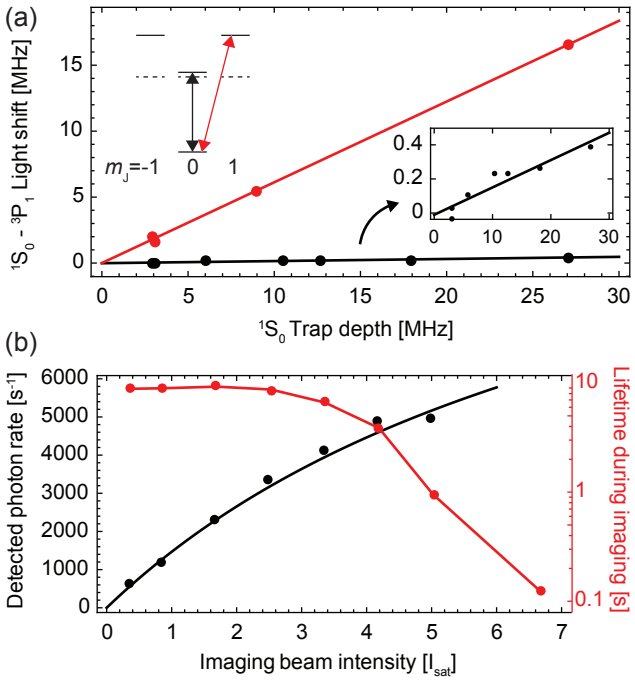

Figure 3.2: (a) Differential light shift of the $^1S_0$ - $^3P_1$ transition as a function of the ground state optical tweezer depth. The tensor light shift lifts the degeneracy of the $^3P_1$ m_J levels, resulting in different potentials for the $m_J = 0$ (black) and $m_J = \pm 1$ (red) excited states. The light shift for the $^1S_0$ - $^3P_1$ $m_J = 0$ transition is 1.6% of the ground state trap depth, corresponding to a shift of only $\Gamma_{556}/2$ under typical trapping conditions. The horizontal axis is calibrated using the previously measured value of the $^3P_1$ $m_J = \pm 1$ polarizability at 532 nm [1]. (b) Lifetime and scattering rate of trapped atoms under various imaging intensities at a typical imaging detuning of $\Delta \approx -1.5\Gamma_{556}$. The black curve is a fit to a saturation model. The lifetime decreases exponentially with increasing imaging power above $I/I_{sat} \approx 4$ (red line guides the eye). We find $I/I_{sat} \approx 3$ to be the optimal balance of photon scattering rate and lifetime for this detuning.

light, the tensor light shift lifts the degeneracy of the $^3P_1$ m_J states, resulting in different potentials for the $^3P_1$ $m_J = 0$ and $m_J = \pm 1$ states (here, m_J refers to the projection of the electronic angular momentum J onto the x axis, which is parallel to the optical tweezer polarization). We measure the transition frequency between $^1S_0$ and the $^3P_1$ $m_J = 0$ and $m_J = \pm 1$ states by blowing atoms out of the trap with resonant light before imaging. The differential shift of the $^1S_0$ and $^3P_1$ $m_J = 0$ states is approximately 1.6% of the ground state trap depth, in agreement with previous measurements [1]. Under typical trapping conditions, the transition frequency is blue-

shifted $2\pi \times 90$ kHz $\approx \Gamma_{556}/2$ in the trap. The positive sign and small magnitude of this shift facilitates efficient loading of atoms from the $^3P_1$ MOT into the tweezers.

3.2 High Fidelity Imaging

After loading the tweezers and applying a brief pulse to remove multiple atoms (20 ms, $\Delta \approx -2\Gamma_{556}$, $I/I_{sat} \approx 5$), we measure an atomic temperature of 6.4(5) μK (using the release-and-recapture technique [88]). In order to determine the optimal fluorescence imaging parameters, we study the lifetime of the trapped atoms in a 0.29 mK deep potential under continuous illumination from the imaging beam as a function of intensity at a detuning $\Delta = -1.5\Gamma_{556}$ (Fig. 3.2b). The lifetime decreases exponentially with intensity (above $I/I_{sat} \approx 4$), consistent with a linear increase in temperature [89] and exponentially-activated tunneling over a barrier; however, at moderate intensities ($I/I_{sat} \approx 3$) we achieve lifetimes near 10 seconds with a photon scattering rate that we estimate to be $0.29 \times \Gamma_{556}/2$ based on the observed saturation of the fluorescence with increasing intensity. The measured temperature during imaging is 13(2) μK, consistent with Doppler theory. In deeper traps, we observe longer lifetimes at high imaging intensities, consistent with the model of heating-induced loss.

An important metric for initializing large-scale low-entropy arrays and performing high-fidelity qubit readout is the fidelity with which a single atom can be imaged. To quantify this, we take repeated images of a 9-site (3x3) array for 5 seconds under continuous illumination, with varying exposure time and negligible delay between images. A histogram of the number of detected photons on a single site during a 30 ms exposure is shown in Fig. 3.3a. In each image, we classify each site to be either bright or dark, indicating the presence or absence of an atom; ideally, this would remain unchanged across multiple images. We quantify the imaging performance by the probability of either of two events to occur: $P_{b\to d} = P(n_{i+1} = d|n_i = b)$, indicating

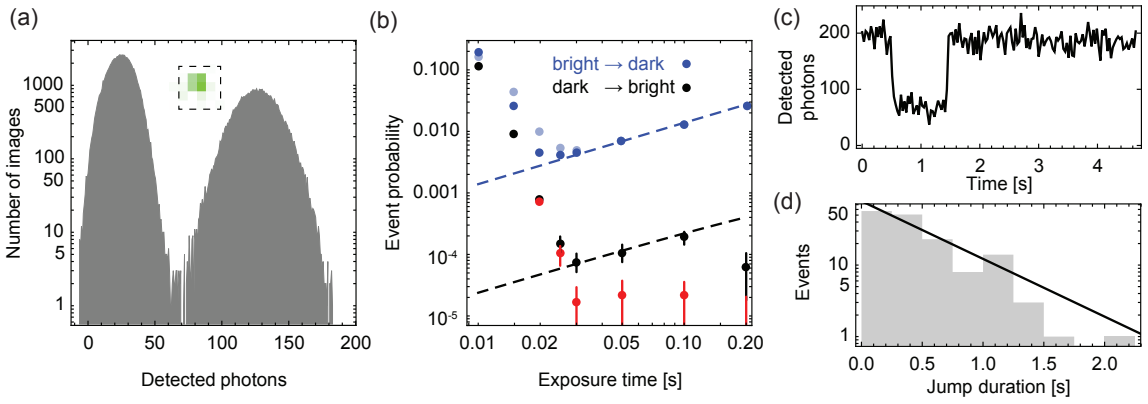

Figure 3.3: (a) Histogram of detected photons at a single site for an exposure time of 30 ms ($\sim$ 136,000 images), revealing clear separation between fluorescence counts for 0 and 1 atom occupancy. Inset: Typical image of single atom, with integration region indicated. (b) Imaging fidelity, quantified by the probability of disagreement between two subsequent images of the same array. Two event types are classified: blue points show the probability of bright sites appearing dark in the next image [$P_{b\to d} = P(n_{i+1} = d|n_i = b)$, where $n_i = \{d, b\}$ denotes the state in image i] and black points show the probability of a dark site appearing bright in the next image [$P_{d\to b} = P(n_{i+1} = b|n_i = d)$]. The light blue symbols show the classification using a simple count threshold, while the other points (blue, black, red) use a pixel-wise Bayesian classifier that has approximately half the error rate. For exposure times greater than 20 ms, $P_{b\to d}$ is dominated by atom loss, consistent with the independently measured lifetime (7.2 s) for these imaging conditions (blue curve). $P_{d\to b}$ reaches a floor below 1×10^{-4} that originates from quantum jumps out of a metastable state. A representative jump event is shown in panel (c): a tweezer initially loaded with an atom goes dark, but spontaneously becomes bright one second later, though the MOT is off the entire time. The duration of these events [panel (d)] is consistent with a metastable state lifetime of $\tau_m = 0.54(7)$ s (exponential fit is shown in black). The black dashed curve in (b) is a fit to $P_m(1 - e^{-t/\tau_m})$, which describes the rate of these events for an average metastable state population P_m, which we infer to be $P_m = 4 \times 10^{-3}$. The red points in (b) show $P_{d\to b}$ with conclusively identified quantum jump events removed.

that a bright site transitions to dark in the next image, and $P_{d\to b} = P(n_{i+1} = b|n_i = d)$, indicating that a dark site appears bright in the next image.

At short exposure times, both events occur often because of noise. At exposure times greater than 20 ms, $P_{b\to d}$ is limited by loss from the traps, in a manner consistent with the independently measured lifetime of 7.2 s for these imaging conditions. The minimum value ($P_{b\to d} = 4.5(3) \times 10^{-3}$, averaged across all sites in the 3x3 array)

occurs at 20 ms imaging time.

For longer exposure times, $P_{d\to b}$ continues to improve, reaching a minimum of $7(3) \times 10^{-5}$ at 30 ms exposure time, suggesting a false-positive rate for atom detection below 10^{-4}. Interestingly, the $d \to b$ events contributing to this rate are not primarily classification errors, but are characterized by the sudden appearance of an atom as shown at $t = 1.5$ s in the sequence of images in Fig. 3.3c. We believe these events correspond to quantum jumps of atoms from trapped, metastable states back into the ground state. An alternative interpretation, loading of new atoms from the background vapor, is ruled out by the fact that these events are nearly always preceded by a $b \to d$ transition. A histogram of the dark state duration of many such events (Fig. 3.3d) reveals the metastable state lifetime to be $\tau_m = 0.54(7)$ s. This value is consistent with the measured $^3\mathrm{P}_0$ state lifetime in the tweezer [90] (shorter than the free-space value because of Raman scattering of the dipole trap light), suggesting that the metastable state may be $^3\mathrm{P}_0$, although we cannot rule out $^3\mathrm{P}_2$ or another long-lived state involving excitation of $4f$ electrons [91]. Removing $d \to b$ events identified as quantum jumps from the dataset (red points in Fig. 3.3b) leads to an improved statistical false-positive atom detection rate of $3(3) \times 10^{-5}$.

The quantity $P_{b\to d}$ is important because it sets an upper bound on the size of the atom array that can be filled without defects ($N_{max} \approx 1/P_{b\to d}$), since atoms must survive the initial image (additional contributions arise from the rearrangement process itself [30, 31]). Our value, $P_{b\to d} = 4.5(3) \times 10^{-3}$ ($N_{max} \approx 220$) is comparable to the lowest directly measured quantity reported in the literature, despite our use of a narrow transition for imaging (previously, values around 0.006-0.01 have been reported [30, 92]). The imaging fidelity, defined as the probability to correctly determine what the occupancy of a tweezer was at the *beginning* of the imaging period, is not a directly measurable quantity. We conservatively estimate it to be 0.9985 (at 25 ms exposure)

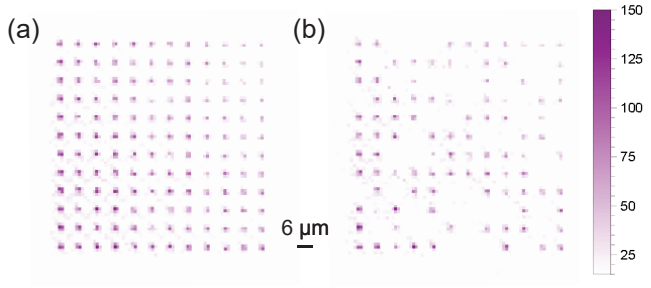

Figure 3.4: (a) Average and (b) single-shot images of a 12x12 tweezer array, with 6 μm spacing, using simultaneous $^1P_1$ imaging and $^3P_1$ cooling. The detected photon rate is much lower for this imaging method, so the exposure time is 500 ms. The color bar indicates the number of detected photons on each pixel. Over repeated single-shot images, the average (worst) site has loading probability $p = 0.49$ ($p = 0.35$).

by modeling the probability for an atom to be lost before scattering enough photons to rise above a count threshold, assuming a constant loss rate during the imaging period. The imaging error rate is a factor of 80 lower than previous results for Yb imaging in shallow traps [1]. These results show that narrow lines with $\Gamma \approx 2\pi \times 200$ kHz are a "sweet spot" for single-atom fluorescence imaging in optical traps, offering a balance between photon detection rate and low temperatures during imaging. This may be applied to optical tweezer arrays and quantum gas microscopes based on other atomic species with similar transitions, including Er [93] and Dy [94].

As an outlook, we demonstrate stochastic loading of a 144-site (12x12) array of optical tweezers (Fig. 3.4). Auto-fluorescence in the objective housing from the trapping light results in spatially uniform background noise on the camera proportional to the total number of tweezers, preventing us from imaging this array at 556 nm using the techniques described above. However, there is very little trap-induced fluorescence at 399 nm (higher in energy than 532 nm), which enables us to image scattered light from the $^1P_1$ transition while simultaneously cooling on the $^3P_1$ transition, following Ref. [1]. After this work we had Special Optics color the inside of the objective housing black which greatly reduced the background from auto-fluorescence.

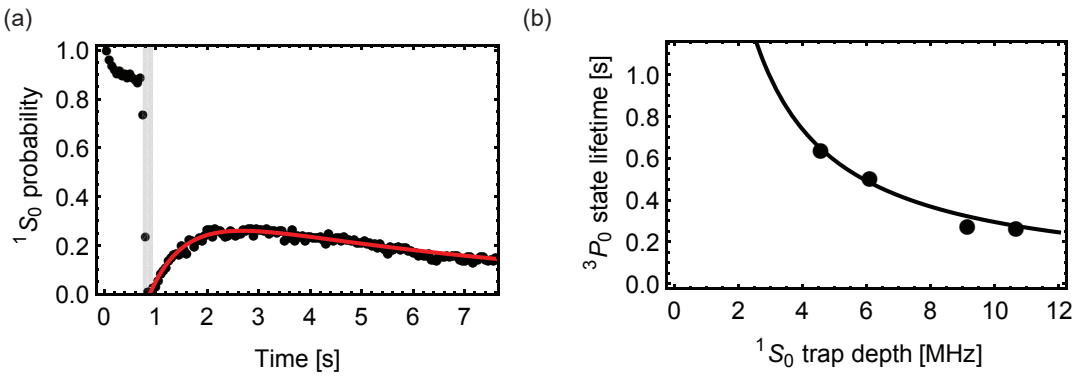

Figure 3.5: (a) A representative measurement of the ^{3}P$_0$ state lifetime, taken at 4.5 MHz trap depth. The 1539 nm optical pumping light is on for 200 ms (indicated by shaded gray region), while the atoms are continuously imaged. The rise in the ground state population after the pulse is caused by atoms leaving ^{3}P$_0$ and returning to the ground state, while the longer time scale decay is due to the finite lifetime ($\sim$7 s) of atoms in the tweezers. The red line is a fit to a two-state rate equation model. (b) The ^{3}P$_0$ lifetime varies inversely with trap depth. The black line is a fit to $\tau_m \propto 1/U$, where τ_m is the ^{3}P$_0$ lifetime and U is the trap depth.

Note While completing this work, we became aware of related publications on Strontium optical tweezer arrays [44, 45].

3.2.1 Measurement of Metastable State Lifetime

We measured the lifetime of the metastable ^{3}P$_0$ state in the tweezers by pumping atoms into this state using the ^{3}P$_1$ - ^{3}D$_1$ transition at 1539 nm. ^{3}D$_1$ decays into all of the ^{3}P$_J$ states, but the ratio of the ^{3}P$_0$ and ^{3}P$_2$ branching ratios is $\sim$ 65 [95], so nearly all atoms are pumped into ^{3}P$_0$. Continuously imaging the ground state population reveals the timescale for depopulation of ^{3}P$_0$ (Fig. 3.5a). The inverse dependence of the lifetime on the tweezer depth suggests that Raman scattering of dipole trap photons is responsible for depleting ^{3}P$_0$ (Fig. 3.5b). Approximately half of the atoms do not return to the ground state, presumably because they decay into other, untrapped metastable states (*i.e.*, certain sublevels of ^{3}P$_2$, or states with $4f$ electron excitations).

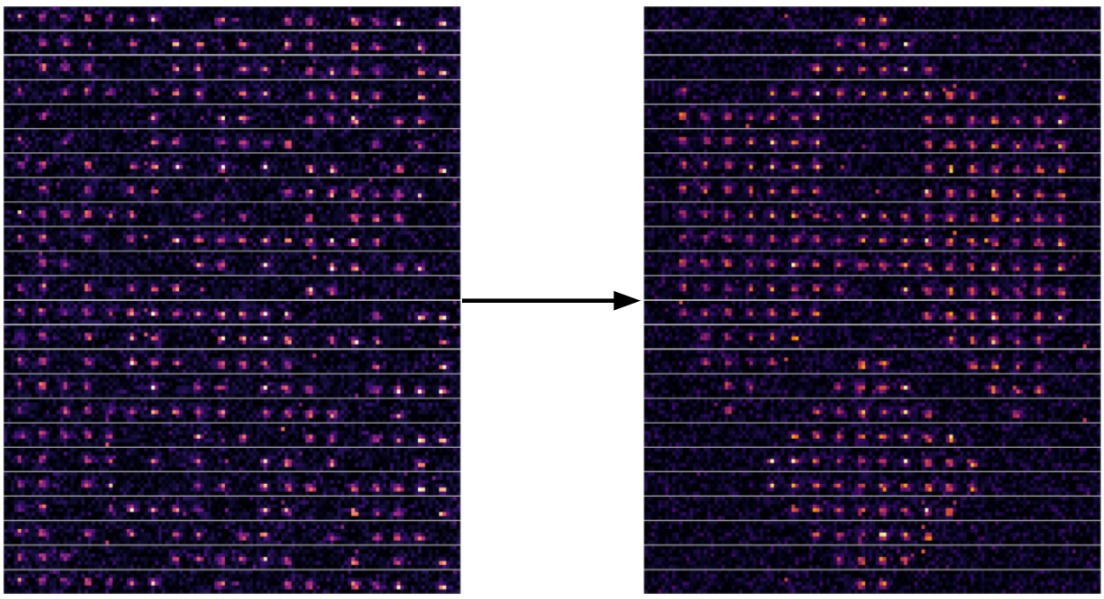

Figure 3.6: We demonstrate the rearrangement protocol by taking 25 randomly loaded 1D arrays and deterministically rearranging each array into a pattern that can be stacked to replicate the Princeton University shield logo.

The similarity of the measured $^3P_0$ lifetime at 6 MHz trap depth (0.51(2) s) and the lifetime of the metastable state described in Fig. 2.3 (0.54(7) s) suggests that the observed state is $^3P_0$. Definitive proof could be obtained by repumping the $^3P_0$ level, but we do not currently have a suitable laser available.

3.3 Tweezer Rearrangement

Work to implement rearrangement in our experimental system was led by Shuo Ma.

Our high-fidelity imaging enables us to create large 1D defect-free arrays with high-fidelity. After the tweezers are loaded a fluorescence image is taken to determine which sites of the array have an atom. Following the initial image the RF tones associated with empty sites are turned off and a waveform is calculated to move the the RF tones of the filled sites to the desired position in the final array. The trajectory of each atom is designed to follow a minimum-jerk trajectory, which ensures the position and

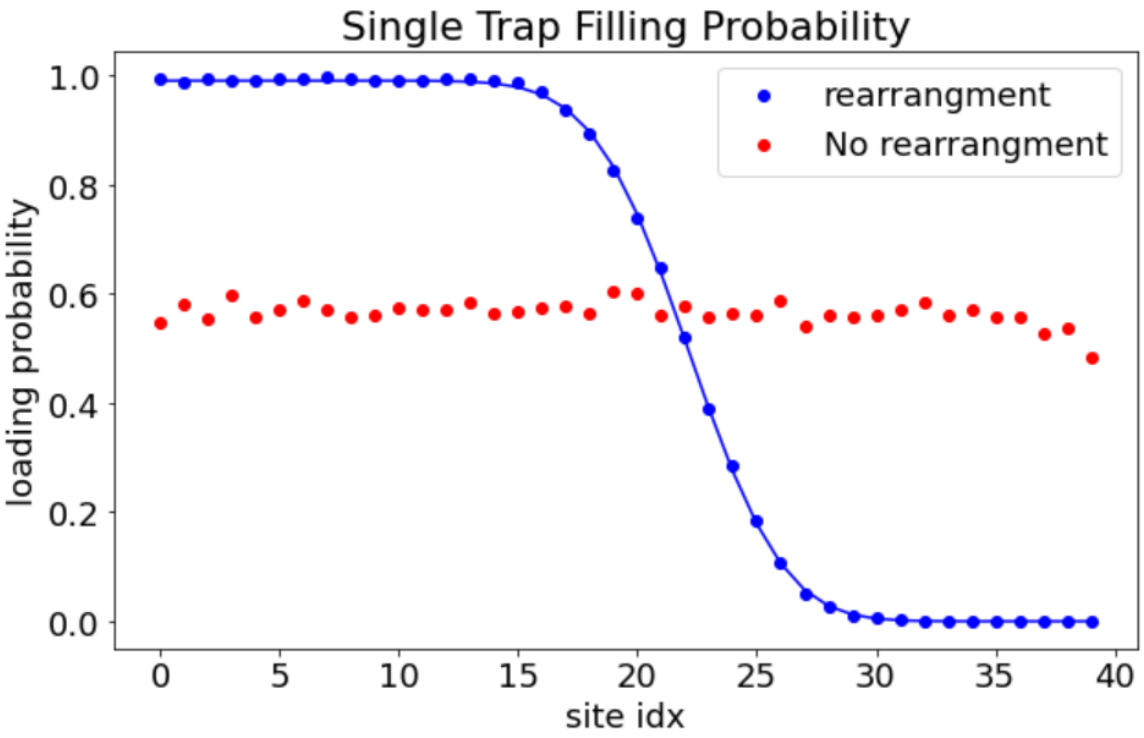

Figure 3.7: We compare the occupation probability of each site in a 40 site array before and after rearrangement. The average initial occupation of the 40 sites (red points) is about 55%. After rearrangement the left most sites are filled with almost unity probability and the occupation probability of the n^{th} is consistent with the binomial distribution suggested by the initial loading probability, indicating an extremely low-loss rearrangement process

velocity of the atom is changed as smoothly as possible to minimize loss during the rearrangement process. The rearrangement waveform must be calculated as quickly as possible to minimize the probability of atom loss during the waveform calculation. To achieve fast computation times we utilize a parallel GPU computing architecture Nvidia CUDA (Compute Unified Device Architecture) to leverage the 1500 GPU cores in the Nvidia 1650Ti card used in our experiment. The ability to use parallel GPU computation leads to a computation time linear in the number of trajectories we need to calculate, with a roughly 50 μs calculation time per trajectory.

Fig. 3.6 shows an example of the rearrangement protocol where we separately rearrange 25 randomly loaded 1D arrays to deterministically generate the Princeton

University shield when the rearranged 1D arrays are stacked into a single image. We also measure the efficacy of the rearrangement by stochastically loading a 40 site array and moving all filled sites to one side of the array (Fig. 3.7). The average initial occupation of each site is $\sim 55\%$ prior to rearrangement. After rearrangement the occupation of the n^{th} site follows the binomial distribution with an initial loading probability of 55%, indicating a low-loss rearrangement process.

Chapter 4

Rydberg Spectroscopy

After high-fidelity single site imaging and control of ^{174}Yb, the next crucial ingredient for engineering complex quantum systems in an Yb tweezer array is introducing long-range interactions through Rydberg states. However, complete spectroscopy of low angular momentum Rydberg states in ^{174}Yb is incomplete in the literature. Notably, the $^3S_1$ series, which is a natural candidate for two-photon Rydberg excitation using $^3P_1$ as an intermediate state, was previously unobserved. This motivated our study of the spectroscopy of ^{174}Yb Rydberg states.

We measure the energies of ^{174}Yb Rydberg states using MOT depletion spectroscopy [96, 97]. First, we load a MOT on the $^1S_0$ to $^3P_1$ transition in Yb. After compressing the MOT to $\sim$ 200 μm by ramping the power and detuning, we image the MOT on a camera while exposing it to a UV laser (about 5 mW in a $\sim$ 1 mm beam). Exciting atoms from $^3P_1$ to a Rydberg state reduces the MOT fluorescence amplitude in the image. As detailed in section 2.4, we generate UV light at 308 nm by summing the output of a Ti:Sapphire laser with a 1565 nm fiber laser and doubling the 616 nm output light in a resonant cavity. To perform high resolution spectroscopy, we change the frequency of the TiS and measure the frequency of the 616 nm output

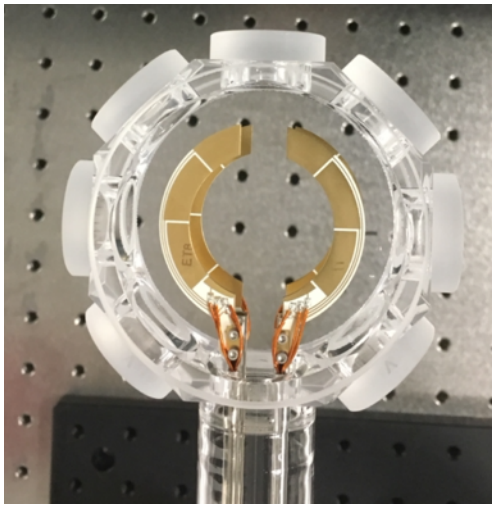

Figure 4.1: An image of the intra-vacuum electrodes used to control the electric field environment of the atoms.

on a wavemeter with 2 MHz (3σ) accuracy (Toptica WS8-2). The wavemeter is calibrated with the ^{174}Yb $^1S_0$ to $^3P_1$ transition frequency (539386602.225 MHz). A typical spectrum is shown in Fig. 4.3a for $n = 49$ $^3S_1$.

4.1 Electric Field Dependence and Control

Due to their large dipole moments Rydberg states are extremely sensitive to DC electric fields. As mentioned in the Section 1.3, the magnitude of DC stark shifts scale as n^{*7}, so any non-zero static electric fields will quickly disturb spectroscopic measurements of high-n Rydberg states.

In order to control the electric field observed by the atoms, we have 16 intra-vacuum electrodes that allow us to zero the electric field in the region of the atoms (shown in Fig. 4.1).

To null the fields we tune the voltages of the electrodes in the X (V_x), Y (V_y), and Z (V_z) axes of our experiment. We set the voltages of the 16 electrodes as is shown in Table 4.1.

Electrode	Voltage
1	$\frac{1}{2}(-V_x + V_y + V_z)$
2	$\frac{1}{2}(-V_x + V_y + V_z)$
3	$\frac{1}{2}(V_x + V_y + V_z)$
4	$\frac{1}{2}(V_x + V_y + V_z)$
5	$\frac{1}{2}(-V_x - V_y + V_z)$
6	$\frac{1}{2}(-V_x - V_y + V_z)$
7	$\frac{1}{2}(V_x - V_y + V_z)$
8	$\frac{1}{2}(V_x - V_y + V_z)$
9	$\frac{1}{2}(-V_x + V_y - V_z)$
10	$\frac{1}{2}(-V_x + V_y - V_z)$
11	$\frac{1}{2}(V_x + V_y - V_z)$
12	$\frac{1}{2}(V_x + V_y - V_z)$
13	$\frac{1}{2}(-V_x - V_y - V_z)$
14	$\frac{1}{2}(-V_x - V_y - V_z)$
15	$\frac{1}{2}(V_x - V_y - V_z)$
16	$\frac{1}{2}(V_x - V_y - V_z)$

Table 4.1: Voltage on each electrode as a function of the desired voltage in all three orthogonal axes.

Then for each axis of the experiment we vary $V_{x(y,z)}$ and measure the resonance of a $^3S_1$ Rydberg state. We fit a quadratic function to the measured resonances as a function of $V_{x(y,z)}$ and take the minimum of the quadratic fit to be the electrode voltage at which the electric field is zeroed in that axis. An example for the n = 85 $^3S_1$ state is shown in Fig. 4.2a.

However, a complication in the process of zeroing the electric fields is that changing the potential on the electrodes results in an extremely long (10-30 minutes) settling time for the electric field seen by the Rydberg atoms, which we believe arises from significant field penetration into the glass and slow redistribution of charges there. In practice, this makes finding and maintaining a precise null difficult. For example, we may measure a set of voltage-dependent resonances to find the quadratic minimum of the stark shift in electrode voltage and then when we try to return the electrode voltage to the point of minimum stark shift, the change in voltage may activate a charge redistribution process which makes the previously measured null field point

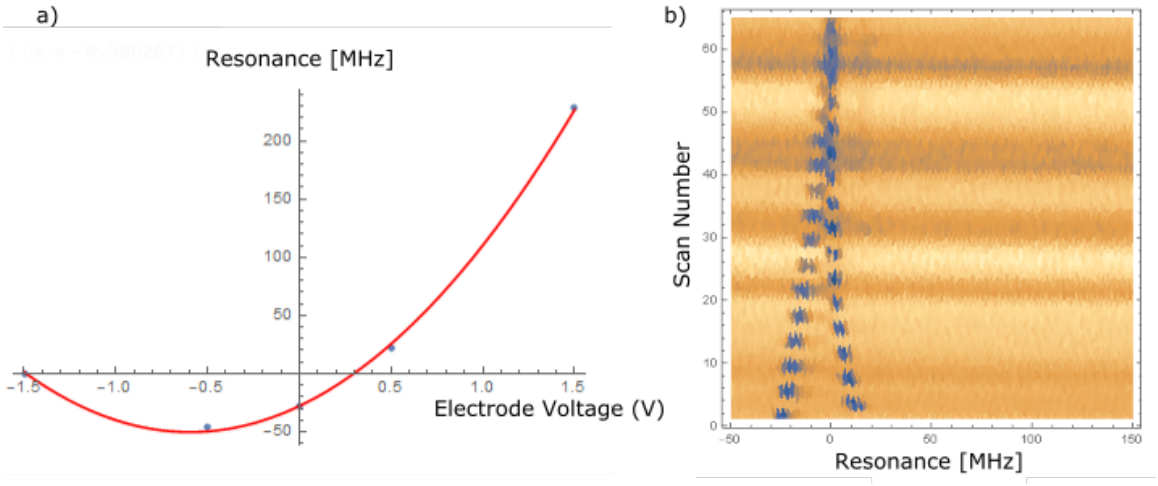

Figure 4.2: a) A measurement of the n = 85 $^3S_1$ resonance as a function of the electrode voltage along the x-axis (Absolute measurement of resonance has arbitrary offset). We fit the resonance to a quadratic function of the electrode voltage to find the null-field point. b) An example of repeated measurement of n = 85 $^3S_1$ resonance as electrode voltage is toggled repeatedly between $V_1 = -0.95$ and $V_2 = +0.05$ V. The first resonance scan is at the bottom of the figure, where the blue regions indicate a resonance feature. At first there is a significant difference between the resonances at the two fields (∼40 MHz), however, as we repeatedly scan the resonance (∼30 s per scan) the two resonances begin to move towards each other until they eventually settle to be equal after 20-30 minutes. Returning to $V_{null} = \frac{V_1+V_2}{2}$ achieves the null-field point without re-initiating a charge distribution process.

no longer the null field point.

We study the long time-scale settling of the fields by repeatedly toggling between two electrode voltages (V_1 and V_2) in a single axis and measuring the resonance of the Rydberg state. The idea behind this method is to keep the average electric field experienced by the slow moving charges in the glass cell constant, while allowing us to change the field at the atoms on a shorter time scale. The initial toggling will initiate a change in the average electric field and thus activate a long time-scale redistribution of charges. However, if we could toggle the voltages such that after the initial redistribution of charges $\frac{V_1+V_2}{2} = V_{null}$, then after the measurement we could return the voltage to the zero-field point (V_{null}) without activating a charge redistribution process in the glass cell, since the average field experienced by the

cell will not have changed over relvant time scales. The signature of the condition $\frac{V_1+V_2}{2} = V_{null}$ would be if the resonance condition E(V_1) = E(V_2) is met after the initial charge redistribution.

This process is demonstrated in Fig. 4.2b, where the resonance is continuously measured while toggling V_x between -0.95 and +0.05 V. These resonances initially drift due to charge redistribution in the glass cell and then settle after 20-30 min such that E(V=-0.95) = E(V=+0.05). This allows us to estimate the null voltage to be $V_{null} = -0.45$ V.

As a solution to the problem of long time-scale electric field drifts, we found that the field settling time can be shortened dramatically by illuminating the glass cell with a ∼1 W UV LED at 365 nm (Ref. 27 of [59]). After changing the electrode voltages while the UV LED is illuminating the glass cell, we observe no change in Rydberg state resonances from repeated measurements (10s of seconds per measurement), suggesting an upper bound on the field settling time of a few seconds. We believe the UV light ionizes charge traps in the glass cell, resulting in much faster equilibration of the charge distribution when the electrode potentials are changed. This allows field cancellation at the mV level. The resulting offset potentials are stable for weeks, which will allow for more precise study of the high-n spectroscopy in the future.

4.2 Spectroscopy of $^3S_1$ ^{174}Yb Rydberg Series

We perform spectroscopy on the previously unmeasured $^3S_1$ ^{174}Yb Rydberg series. Table 4.3 presents the measured energies for the $^3S_1$ series. The high resolution wavemeter gives an accuracy of 4 MHz in UV laser frequency. To determine the absolute energy of the levels, we add the ^{174}Yb $^1S_0$ to $^3P_1$ transition frequency, determined from ^{171}Yb $^1S_0$ $F = 1/2$ to $^3P_1$ $F = 3/2$ frequency (539390406.833 MHz) measured in [98], along with the isotope and hyperfine shifts from [99]. By fitting the measured

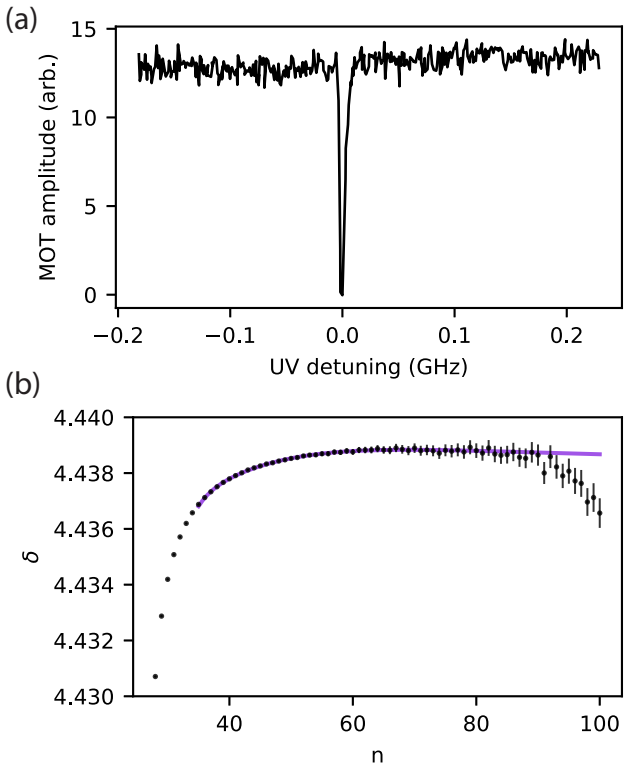

Figure 4.3: (a) Example spectrum for the $^3S_1$ Rydberg line at $n = 49$. (b) Measured quantum defects of the $^3S_1$ Rydberg series vs. principal quantum number. Error bars show uncertainties in the defects from the 4 MHz uncertainty in the measured UV frequencies. The purple line is a fit to an extended Rydberg-Ritz model for $35 < n < 80$.

energies to $E_I - \frac{Ry}{(n-\delta)^2}$ in the region $60 \leq n \leq 80$, we determine the ^{174}Yb ionization energy to be $E_I = 50443.07074(4)$ cm^{-1}, within 10 MHz from the value reported in Ref. [100] (Ry is the Rydberg constant).

The measured quantum defects for $n = 28$ to $n = 100$ are shown in Fig. 4.3b. To obtain a practical model for the defect at lower n, we fit them to the extended Rydberg Ritz formula:

$$\delta(n) = \delta_0 + \frac{\delta_2}{(n-\delta_0)^2} + \frac{\delta_4}{(n-\delta_0)^4} + ... \tag{4.1}$$

The fit parameters for the region $35 < n < 80$ are summarized in Table. 4.2, and the

fitted energies are within our experimental uncertainty in this range.

Fit Parameter	Value
δ_0	4.4382(2)
δ_2	6(1)
δ_4	-1.8(4)$\times 10^4$
δ_6	1.8(5)$\times 10^7$
δ_8	-7(2)$\times 10^9$

Table 4.2: Parameters for the fit to the extended Rydberg-Ritz model in Eq. (4.1), for $35 < n < 80$.

The measured defects are flat around $\delta = 4.439$ from $n = 40$ to $n = 80$. At high n ($n > 85$), we observe a systematic deviation of the energies to higher values. One possible explanation for this would be DC Stark shifts from stray electric fields, which scale as n^{*7}. The dependence of the high-n deviations, however, is closer to n^{*12} than the expected n^{*7} scaling from DC Stark shifts. The deviations could instead be explained by a drifting electric field in time, or could point to something else.

n	Energy (cm^{-1})	n	Energy (cm^{-1})
28	50245.5285	64	50412.1374
29	50261.2497	65	50413.1505
30	50275.1772	66	50414.1147
31	50287.5688	67	50415.0329
32	50298.6401	68	50415.9083
33	50308.5712	69	50416.7432
34	50317.5130	70	50417.5402
35	50325.5925	71	50418.3016
36	50332.9169	72	50419.0294
37	50339.5773	73	50419.7256
38	50345.6515	74	50420.3921
39	50351.2064	75	50421.0303
40	50356.2995	76	50421.6420
41	50360.9806	77	50422.2285
42	50365.2929	78	50422.7914
43	50369.2741	79	50423.3316
44	50372.9574	80	50423.8507
45	50376.3717	81	50424.3495
46	50379.5425	82	50424.8291
47	50382.4925	83	50425.2906
48	50385.2417	84	50425.7348
49	50387.8079	85	50426.1625
50	50390.2071	86	50426.5745
51	50392.4533	87	50426.9718
52	50394.5593	88	50427.3548
53	50396.5366	89	50427.7242
54	50398.3955	90	50428.0809
55	50400.1451	91	50428.4254
56	50401.7940	92	50428.7578
57	50403.3496	93	50429.0794
58	50404.8190	94	50429.3902
59	50406.2082	95	50429.6906
60	50407.5232	96	50429.9813
61	50408.7690	97	50430.2627
62	50409.9505	98	50430.5352
63	50411.0720	99	50430.7988
64	50412.1374	100	50431.0545

Table 4.3: Measured energies of the ^{174}Yb $6sns\ ^3S_1$ Rydberg series from $n = 28$ to $n = 100$.

Series	δ_0	δ_2	δ_4
$^3D_1$	2.75241(2)	3(3) $\times 10^{-1}$	-1(1) $\times 10^2$
$^3D_2$	2.74832(4)	-5(1) $\times 10^{-1}$	3.0(4) $\times 10^2$
$^1D_2$	2.7114(2)	-3.6(4)	3.4(2) $\times 10^3$

Table 4.4: Fitted quantum defects for D Rydberg series.

4.3 Spectroscopy of D ^{174}Yb Rydberg Series

We also perform spectroscopy on a set of L = 2 Rydberg series, $^3D_1$, $^3D_2$, and $^1D_2$. $^1D_2$ is only accessible out of $^3P_1$ due to singlet-triplet mixing with $^3D_2$. The measured quantum defect as a function of the principal orbital quantum number, n, for each series is shown in Fig. 4.4. In the range $40 \leq n \leq 60$ the quantum defect of each series is flat, showing that each of these series is not affected by a perturbing state in this region. The measured quantum defects for $^3D_2$ and $^1D_2$, shown in Table 4.4 are in good agreement with previously measured quantities by Ref. [100], which performed spectroscopy with a two photon excitation process through the $^1P_1$ state. We also show the first measurement of the $^3D_1$ Yb Rydberg series, which is inaccessible out of $^1P_1$.

However, at large principal quantum numbers the measured lines begin to look far more complex. First, at $n \approx 64$ the $^3D_2$ series begins to split into two lines, which we attribute to stray electric fields causing variable Stark shifts on different m_j levels. Similarly, we see the $^1D_2$ series begin to split into two lines at $n \approx 90$. Furthermore, we observe the appearance of additional lines (black and red points in Fig. 4.4). These lines appear to form an avoided crossing like feature near n = 80. We hypothesize that this line is a signature of the highly-perturbed $^3P_1$ Rydberg series, which has previously been measured to have a moving quantum defect, which crosses through the resonance of the $^3D_1$ and $^3D_2$ series near n = 80 [101]. In principle we should not be able to excite to the 6sns $^3P_1$ series out of 6s6p $^3P_1$, however, with even small stray electric fields the $^3P_1$ series can strongly mix with $^3D_1$ leading to the avoided crossing

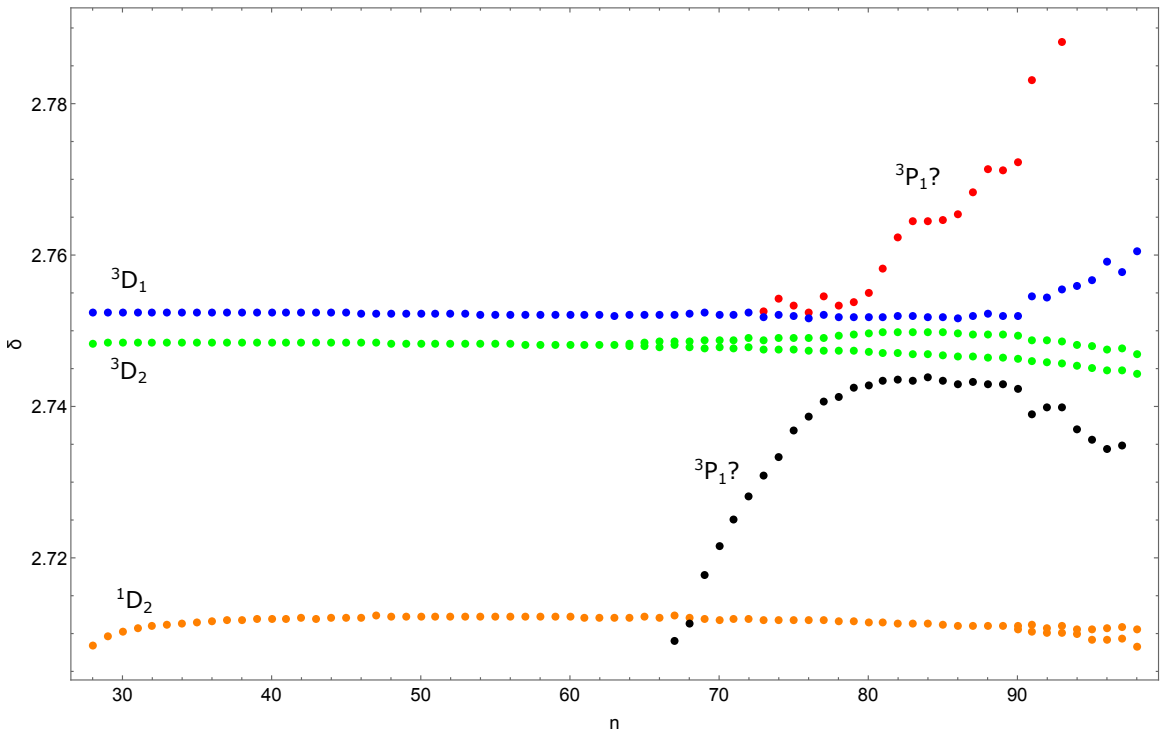

Figure 4.4: Quantum defect, δ of the $^3D_1$ (blue points), $^3D_2$ (green points), and $^1D_2$ (orange points) versus principal quantum number n. For $n < 60$ the quantum defects are flat, indicating a non-perturbed Rydberg series. At higher n we theorize that stray electric fields lead to m_j dependent Stark shifts causing splitting of lines. Furthermore, we begin to observe an additional line which has a highly-n dependent quantum defect, which we hypothesize is related to the strongly perturbed $^3P_1$ series.

type feature, which we observe.

Chapter 5

Trapped alkaline earth Rydberg atoms in optical tweezers

The work described in this chapter is also presented in Ref. [40]

A central challenge to experiments with Rydberg atoms in standard, red-detuned optical tweezers is that they are repelled from the intensity maximum. This repulsion arises from the ponderomotive potential of the essentially free Rydberg electron, described by the polarizability $\alpha_p = -e^2/m_e\omega^2$ (ω denotes the frequency of the trap light, and e, m_e are the electron charge and mass), which is always negative [102]. To mitigate this effect, the vast majority of experiments operate with the tweezers turned off during the Rydberg excitation, which limits the interaction time to 10-20 μs because of the expansion of the atoms at typical temperatures of 10-20 μK. This is significantly below the typical room temperature Rydberg state lifetime of 100-300 μs for $n = 60 - 100$ S states [103, 16], and far below the tens of seconds achievable with circular states in cryogenic cavities [104]. Furthermore, heating associated with modulating the trap may impact the gate fidelity in sequential operations.

In recent work, it has been demonstrated that the ponderomotive potential can

be used to trap Rydberg atoms in a 3D intensity minimum. Rubidium Rydberg states have been trapped for up to 200 μs in "bottle beams" generated by focusing a Laguerre-Gauss beam with orbital angular momentum [105], while simultaneous trapping of Rydberg states has been achieved in a lattice of blue-detuned light sheets, with 50 μs dwell time for atoms in Rydberg states [106]. The stability of these traps requires that the spatial extent of the intensity minimum be large compared to the Rydberg electron orbit ($R_e = 3n^2a_0/2 \approx 0.8\,\mu$m for $n = 100$). This necessitates a large-waist optical trap, a corresponding increase in total optical power per trap, and imposes a maximum principal quantum number that can be trapped for a given power, of order $n = 90$ in Refs. [105, 106]. Ensembles of Rydberg atoms have been trapped using several approaches [107, 108, 109, 110, 111].

In this chapter, we demonstrate an alternate approach: leveraging the polarizability of the Yb^+ ion core to directly trap Yb Rydberg atoms in conventional, red-detuned optical tweezers at 532 nm. Unlike alkali atoms, the ion core of alkaline earth atom Rydberg states has significant polarizability at typical laser trapping wavelengths. The ponderomotive potential of the Rydberg electron contributes an anti-trapping effect, but it is small for short wavelengths and high-n Rydberg states where the beam waist is comparable to or smaller than R_e. We demonstrate trap lifetimes exceeding 100 μs for $n = 75$ with less than 10 mW of optical power per trap. Trap-induced losses from photo-ionization are negligible for S states, but slightly shorten the lifetime of P and D states. We study the interplay of the ponderomotive and Yb^+ core potentials in detail, including the dependence on the Rydberg level, and observe that "magic" trapping is possible for certain pairs of Rydberg states. A theoretical model is presented to efficiently calculate the trapping potentials based on a decomposition of the optical tweezer into irreducible tensor operators. We study the coherence properties of a superposition of trapped Rydberg levels, achieving $T_2 = 59$ μs, limited by finite temperature and the differential light shift of the two states in

the trap but exceeding the lifetime of the Rydberg atom in the absence of the trap. This work also presents the first measurement of the lifetime of high-n Yb Rydberg states.

5.1 Calculation of Rydberg Trapping Potentials

To calculate the potential seen by a Rydberg atom in an optical tweezer, we compute the energy as a function of the position of the atomic nucleus $\boldsymbol{R}$. To make the calculation tractable, we restrict our calculation to states with electron configuration $6snl$, and make the approximation that the inner $6s$ and outer nl electrons can be treated separately [61].

The inner electron polarizability is dominated by the Yb^+ ion $6s-6p$ transitions. For linearly polarized trapping light, there is only a scalar polarizability, which has been computed at 532 nm to be $\alpha_c = 96$ atomic units (a.u.) for the $^2S_{1/2}$ ground state [112], giving rise to a potential $U_c = -\frac{1}{2\epsilon_0 c}\alpha_c I$. α_c is around 35% of the ground state ($6s^2$) polarizability (275 a.u. [113] or 226 a.u. [114]), indicating that suitably deep traps can be reached with the same powers used to trap ground states. Intriguingly, it is also very close to the calculated polarizability of the metastable Yb^0 $6s6p$ $^3P_0$ level (95 a.u. [113] or 91 a.u. [114]), which may enable magic-wavelength trapping [39] of high-n Rydberg states and the upper clock state.

The ponderomotive potential of the outer, Rydberg electron is given by Eq. 5.11, reproduced here:

$$U_r = -\frac{1}{2\epsilon_0 c}\alpha_p \int d^3\boldsymbol{r}|\psi(\boldsymbol{r})|^2 I(\boldsymbol{r}+\boldsymbol{R}). \tag{5.1}$$

where $\alpha_p = -e^2/m_e\omega^2$ is the ponderomotive polarizability, $\boldsymbol{r}$ is the coordinate of the electron with respect to the nucleus at $\boldsymbol{R}$, and $\psi(\boldsymbol{r})$ is the electronic wavefunction.

The evaluation of the integral is simplified if $I(r)$ can be expanded in irreducible tensor operators; then, the Wigner-Eckart theorem allows U_r to be expressed for any state in terms of angular factors and fewer than $L+1$ radial integrals. For a lattice, this expansion can be done analytically [61, 115]; however, for a tweezer or other, arbitrary potential it must be done numerically. Specifically, we seek an expansion in spherical harmonics centered on the nuclear coordinate $\boldsymbol{R}$:

$$I(\boldsymbol{r}+\boldsymbol{R}) = \sum_{kq} I_q^{(k)} = \sum_{kq} f_{kq}(r;\boldsymbol{R}) C_q^{(k)}(\hat{r}). \tag{5.2}$$

Here, $C_q^{(k)}(\hat{r}) = \sqrt{\frac{2k+1}{4\pi}} Y_q^{(k)}(\hat{r})$ is the normalized spherical harmonic and $r = |\boldsymbol{r}|$ and $\hat{r} = \boldsymbol{r}/r$, and $f_{kq}(r)$ are the coefficients to be found representing I. These functions, which have $\boldsymbol{R}$ as a parameter, can be computed by exploiting the orthonormality of the spherical harmonics as:

$$f_{kq}(r;\boldsymbol{R}) = \sqrt{\frac{2k+1}{4\pi}} \iint d\Omega I(\boldsymbol{R}+\boldsymbol{r}) Y_q^{(k)}(\theta,\phi). \tag{5.3}$$

Here, the angular integration is performed with respect to $\boldsymbol{r}$.

With the potential decomposed in this way, we can evaluate the matrix element between arbitrary states with quantum numbers $n'l'm'$ and nlm using the Wigner-Eckart theorem:

$$\langle n'l'm'|I|nlm\rangle = \sum_{kq} \langle n'l'm'|I_q^{(k)}|nlm\rangle = \sum_{kq} (-1)^{l'-m'} \begin{pmatrix} l' & k & l \\ -m' & q & m \end{pmatrix} \langle n'l'||I_q^{(k)}||nl\rangle. \tag{5.4}$$

The reduced matrix element (with prefactor f_{kq}) is given by

$$\langle n'l'||I_q^{(k)}||nl\rangle = (-1)^{l'}\sqrt{(2l'+1)(2l+1)}\begin{pmatrix} l' & k & l \\ 0 & 0 & 0 \end{pmatrix} \times \int drr^2 R_{n'l'}(r)R_{nl}(r)f_{kq}(r;\boldsymbol{R}), \quad (5.5)$$

and the potential for a given state is

$$U_r = -\frac{1}{2\epsilon_0 c}\alpha_p\langle nlm|I|nlm\rangle. \quad (5.6)$$

This calculation describes the action of U_r in the nlm basis, but the Rydberg states of real alkali and alkaline atoms have significantly resolved fine structure splittings. Therefore, these expressions must be re-derived in the appropriate basis. Before proceeding further, we note several properties of the potential that are already apparent. First, the contribution of odd-k terms vanishes between states of the same l. Second, $f_{kq} = 0$ when $q \neq 0$ for $\boldsymbol{R}$ on the z-axis, since the potential is cylindrically symmetric. Lastly, only terms with $k \leq l$ have non-vanishing contributions, in order to satisfy the conservation of angular momentum (here, l is the total angular momentum, but in the fine structure basis, this will be replaced by $j = l + s$).

Taken together, these allow the potential U_r for low-l states at $\boldsymbol{R} = 0$ to be evaluated from a small number of f_{kq}, with k even and $q = 0$. At high-l (i.e., circular states) it appears that a large number of f_{kq} contribute to the potential. However, the radial matrix elements and angular coefficients of high-l states decay rapidly with k, fundamentally as a consequence of the fact that a Gaussian beam does not have significant angular momentum, and we find that truncating the calculation to the lowest few values of k is an excellent approximation.

Additionally, we note that some of the off-diagonal matrix elements $\langle n'l'm'|I|nlm\rangle$ are of similar magnitude to the diagonal elements, and in this sense Eq. 5.6 is only the first order term in a perturbative calculation of the energy shift. For the trap depths considered here, the total ponderomotive potential is smaller than the spacing between all of the unperturbed energy levels (including m levels, as we apply a 4.5 G magnetic field), such that the next order terms do not change the potential significantly. However, in the absence of external fields, the off-diagonal terms in m can be significant. More generally, the terms between different l, m may be exploited to drive transitions between Rydberg states in an intensity-modulated beam, where the modulation is resonant with the energy difference between the initial and final states. This could be particularly useful in connection with high-order Laguerre-Gauss beams to create large k terms to efficiently excite circular states (following Ref. [116]). Unlike two-photon electric dipole transitions, which are limited to $k \leq 2$, the ponderomotive potential can drive many angular momentum quanta in a single step.

We now consider the evaluation of the reduced matrix elements separately for alkali atoms and alkaline earth atoms.

5.1.1 Alkali atoms

To compute the potential for alkali atoms, the matrix elements are needed in the spin-orbit (fine structure) basis: $\langle nsljm|I|nsljm\rangle$. As before, we start with the Wigner-Eckart theorem:

$$\langle nsljm|I_q^{(k)}|nsljm\rangle = (-1)^{j-m}\begin{pmatrix} j & k & j \\ -m & q & m \end{pmatrix}\langle nslj||I_q^{(k)}||nslj\rangle. \quad (5.7)$$

Then, we reduce the matrix element again to one only acting on l [117]:

$$\langle nslj||I_q^{(k)}||nslj\rangle = (-1)^{s+l+j+k}(2j+1)\begin{Bmatrix} l & j & s \\ j & l & k \end{Bmatrix}\langle nl||I_q^{(k)}||nl\rangle. \quad (5.8)$$

The reduced matrix element here is the same as Eq. (5.5), and the coefficients are tabulated in Table 5.1.

5.1.2 Alkaline earth atoms

In the case of divalent Yb, we are interested in calculating the trapping potential for Rydberg states with term symbols $^{2S+1}L_J$ and $6snl$ electronic configurations. The LS-coupled basis is a close approximation to the true eigenbasis: in Yb the measured single-triplet mixing arising from spin-orbit coupling in high-n $^3P_1$ states is approximately 6% [118], and this effect is presumably smaller in lighter alkaline earth atoms such as Sr. The ponderomotive potential only acts on the outer electron, so we need to reduce the matrix elements to account for this.

Using the Wigner-Eckart theorem, we calculate the diagonal matrix elements between LS-coupled states with S, L, J denoting the total electronic spin, orbital angular momentum and overall angular momentum, and M the z-projection of J:

$$\langle nSLJM|I_q^{(k)}|nSLJM\rangle = (-1)^{J-M}\begin{pmatrix} J & K & J \\ -M & q & M \end{pmatrix}\langle nSLJ||I_q^{(k)}||nSLJ\rangle. \quad (5.9)$$

Then we reduce the matrix element further to one acting on total L:

$$\langle nSLJ||I_q^{(k)}||nSLJ\rangle = (-1)^{L+S+J+k}(2J+1)\begin{Bmatrix} L & J & S \\ J & L & k \end{Bmatrix}\langle nL||I_q^{(k)}||nL\rangle. \quad (5.10)$$

Now, we would like to reduce $\langle nL||I^{(k)}||nL\rangle$ to a matrix element on the outer electron. However, since we are only interested in states where the inner electron is in $6s$ ($l_i = 0$), we have the situation that $L = l_0$ and we can just replace L with l_r in the above expression. Therefore, the final result for the ponderomotive potential for alkaline Rydberg states of the form $msnl$ is the same as for alkali atoms, using the *total* angular momentum quantum numbers $SLJM$ instead of those for the Rydberg electron alone, $sljm$.

5.1.3 Numerical evaluation of radial integrals

To evaluate the potential numerically, the radial integrals must be performed. $f_{kq}(r)$ is computed using the Gaussian solution to the paraxial wave equation [119]. In the literature, several different approximations have been employed to find Rydberg wavefunctions for the computation of matrix elements using experimentally determined quantum defects, including Coulomb functions and numerical integration of the Schrödinger equation. In this work, we observe that the reduced matrix elements $\langle nl||I_q^{(k)}||nl\rangle$ depend only on the square modulus of the wavefunction and vary extremely slowly with n and l. Therefore, we compute the reduced matrix elements for integer n using hydrogen radial wavefunctions R_{nl}, and interpolate between them to compute the effective matrix element for $n^* = n - \delta_{nSLJ}$, where δ_{nSLJ} is the measured

quantum defect.

5.1.4 Angular dependence

Since the n and l dependence of the radial integrals is small, the variation of the trapping potential between nearby Rydberg states arises primarily from the angular factors in the Wigner-Eckart theorem and the reduction of the dipole operator (Eq. 5.9 and 5.10). These are tabulated for alkali and alkaline earth atoms in Table 5.1. In the alkali case, states of the same j have the same angular factors and therefore approximately the same trapping potential [105]. In the alkaline case this is no longer true; however, the states $^1S_0$, $^3S_1$ and $^3P_0$ have the same (purely scalar) potential.

Term	$k=0$	$k=2$	$k=4$
$^2S_{1/2}$	1	0	0
$^2P_{1/2}$	1	0	0
$^2P_{3/2}$	1	1/5	0
$^2D_{3/2}$	1	1/5	0
$^2D_{5/2}$	1	8/35	2/21
$^1S_0$	1	0	0
$^3S_1$	1	0	0
$^1P_1$	1	2/5	0
$^3P_0$	1	0	0
$^3P_1$	1	-1/5	0
$^3P_2$	1	1/5	0
$^1D_2$	1	2/7	2/7
$^3D_1$	1	1/5	0
$^3D_2$	1	1/7	-4/21
$^3D_3$	1	8/35	2/21

Table 5.1: Angular factors in U_r, expressed as the coefficient of the radial integral involving f_{k0} for the $m=0$ state.

5.2 Lifetime of Trapped ^{174}Yb Rydberg States

The trapping potential for Ytterbium Rydberg states with the configuration $6snl$ arises from separate contributions from the $6s$ core and nl Rydberg electrons [61].

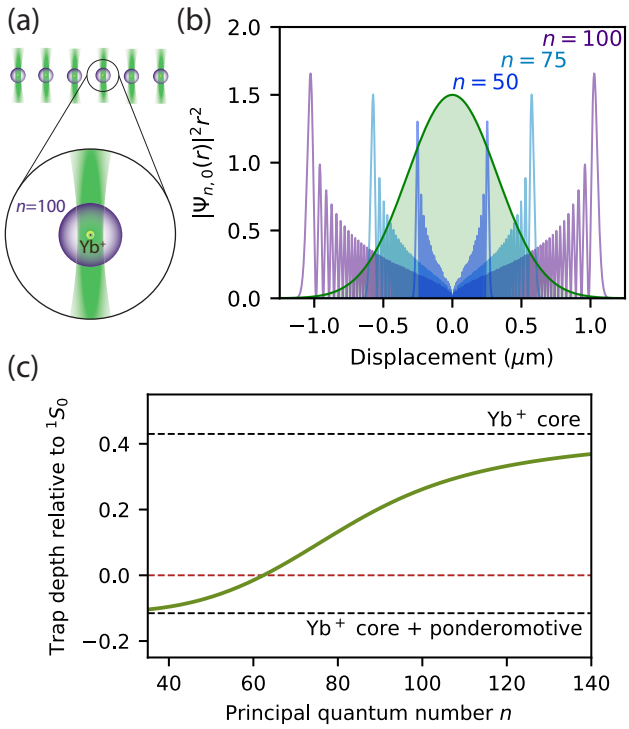

Figure 5.1: (a) Cartoon of the experiment, showing a six-tweezer array, the Rydberg electron wavefunction, and the Yb^+ ion core. (b) Radial probability distributions of Rydberg wavefunctions relative to the optical tweezers (green). (c) Calculated trap depth, normalized to the $^1S_0$ ground state for the same power and beam waist (here, 0.65 μm).

In SI units, the core potential $U_c(\boldsymbol{R}) = -\frac{1}{2\epsilon_0 c}\alpha_c(\omega)I(\boldsymbol{R})$ is derived from the dynamic electric dipole polarizability $\alpha_c(\omega)$ of the Yb^+ ion $6s\ ^2S_{1/2}$ state (here, $I(\boldsymbol{R})$ is the light intensity at the nuclear coordinate $\boldsymbol{R}$, ϵ_0 is the permittivity of free space, and c is the speed of light). For 532 nm light, this is of the same order of magnitude as the Yb^0 ground state potential, as the principal Yb^+ transitions (369, 329 nm) are not too far from the principal Yb^0 transition (399 nm). The nearly free Rydberg electron experiences a ponderomotive potential that depends on the spatially-averaged intensity seen by the Rydberg electron as [102]:

$$U_r(\boldsymbol{R}) = -\frac{e^2}{2\epsilon_0 c m_e \omega^2}\int |\psi_{nl}(\boldsymbol{r})|^2\, I(\boldsymbol{r}+\boldsymbol{R})d^3\boldsymbol{r}. \tag{5.11}$$

Here, $\psi_{nl}(\boldsymbol{r})$ is the wavefunction of the nl electron ($\boldsymbol{r}$ is the electron coordinate relative to the nucleus) (Fig. 5.1b). In Fig. 5.1c, the sum of these contributions for the $^3\mathrm{S}_1$ Rydberg states in an optical tweezer ($\lambda = 532$ nm, $1/e^2$ radius $w_0 = 650$ nm) is shown as a function of the principal quantum number n. For low n where the Rydberg wavefunction is significantly smaller than the beam waist, the total polarizability is just $\alpha_c(\omega) - e^2/m\omega^2$, while at high n it asymptotes to $\alpha_c(\omega)$, as the overlap of the Rydberg electron with the tweezer decreases.

We characterize the trapping potential for Yb Rydberg states using an array of six optical tweezers loaded with single ^{174}Yb atoms as described previously in Ref. [81]. A large array spacing ($d = 24\,\mu$m) minimizes the influence of interactions on the spectroscopy. We excite atoms to Rydberg states using sequential single-photon π pulses on the $^1\mathrm{S}_0 \rightarrow {}^3\mathrm{P}_1\,(m_J = -1)$ and $^3\mathrm{P}_1\,(m_J = -1) \rightarrow 6sns\,{}^3\mathrm{S}_1\,(m_J = -1)$ transitions; this configuration is somewhat inefficient because of the finite lifetime of the intermediate state (860 ns), but avoids noise on our 556 nm laser system that was not designed for coherent two-photon excitation. The 308 nm light for the Rydberg transition is generated by summing the output of a Ti:Sapphire (TiS) laser with a 1565 nm fiber laser and doubling in a resonant cavity. We have generated more than 100 mW in this configuration, but experiments described here used approximately 5 mW focused to 10 μm. We primarily study the Yb $^3\mathrm{S}_1$ state, which has not been previously observed to the best of our knowledge. The series is relatively unperturbed at high-n, with a quantum defect of approximately 4.439 (additional details are provided in section 4.2). For this state, we achieve a Rabi frequency of $\Omega = 2\pi \times 2.5$ MHz.

We measure the trapped lifetime of a Rydberg atom by imaging the array of ground state atoms, exciting to a particular Rydberg state, waiting a variable time τ, and de-exciting using a second UV laser pulse before acquiring a second image. If the Rydberg atom leaves the trap or changes states between the UV pulses (i.e. from

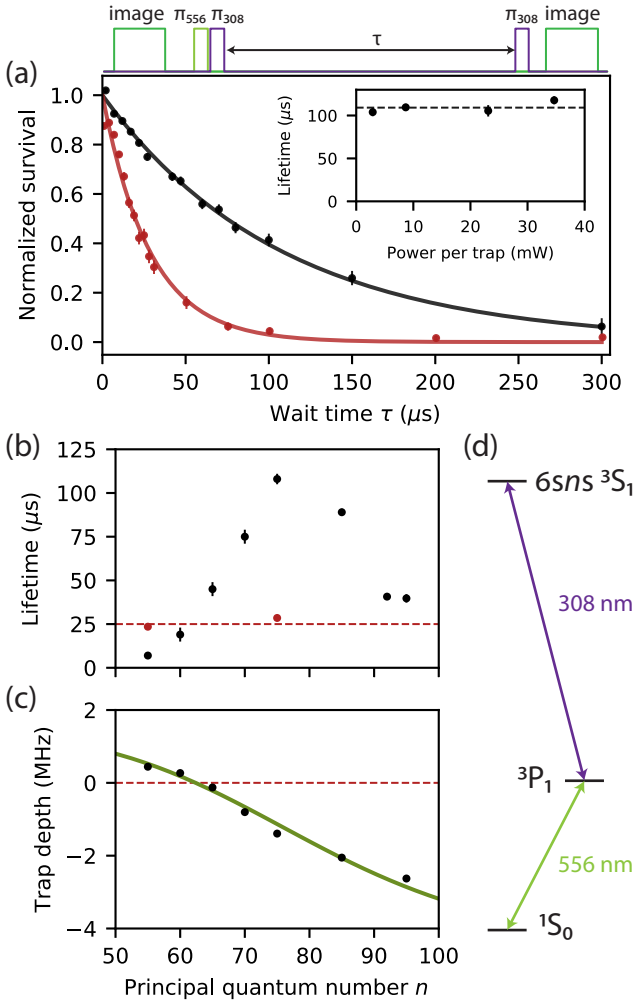

Figure 5.2: (a) Survival probability of the $n = 75$ $^3S_1$ state with (black, $\tau = 108$ μs) and without (red, $\tau = 28$ μs) the traps. Inset: Trapped Rydberg lifetime τ of the $^3S_1$ Rydberg state vs. trap power at $n = 75$. (b) Trapped Rydberg lifetime of the $^3S_1$ state vs. principal quantum number n, with (black) and without (red) the trap. The dashed red line shows the untrapped lifetime of a ground state atom under the same conditions. (c) Trap depth of the $^3S_1$ Rydberg state vs principal quantum number. The green line is the theoretical trap depth using the calculation from Fig. 5.1c. (d) Relevant Yb energy levels for Rydberg excitation.

spontaneous decay or interaction with blackbody radiation), it will not be de-excited by the second pulse and will be recorded as an atom loss between the two images. A typical trace for the $n = 75$ $^3S_1$ state is shown in Fig. 5.2a using 9 mW per trap (12 MHz ground state trap depth). If the trap is turned off between the UV pulses, the Rydberg atom survives for 28 μs, consistent with the measured ground state lifetime

in the absence of a trap. When the trap is on between the UV pulses, the lifetime is extended to 108 μs. To investigate the role of trap-induced loss processes such as photo- or auto-ionization, we measure the lifetime as a function of the trap depth, shown in the Fig. 5.2a inset. We observe no influence of the trap depth on the lifetime over a wide range of powers.

We repeat these measurements at several values of principal quantum number n. At low n (e.g. $n = 55$), the lifetime with the trap is shorter than without the trap, suggesting that these atoms are repelled. Above $n \approx 60$, the trapped lifetimes are longer, consistent with trapping. Curiously, they reach a maximum at $n = 75$ and then decrease, although the intrinsic Rydberg lifetimes are expected to increase monotonically as n^2. We do not observe any trap power dependence of the lifetime between $n = 70$ and $n = 95$, ruling out trap-induced losses. We conjecture that noise or cavity effects from our in-vacuum electrodes may play a role in the reduction of the lifetime.

To study the interplay of the ponderomotive and core ion polarizabilities, we measure the trap depth as a function of n using the AC stark shift of the UV $^3\mathrm{P}_1$ to $^3\mathrm{S}_1$ transition. We measure a crossover from anti-trapped to trapped around $n = 60$, consistent with the lifetime increase. To obtain the absolute shift of the Rydberg state in the trap, we subtract the $^3\mathrm{P}_1$ trap depth, which we infer from the measured $^3\mathrm{P}_1$ -$^1\mathrm{S}_0$ light shift in the trap (7.54 MHz) and the ratio of the polarizabilities of these states $R = \alpha_{^3P_1}/\alpha_{^1S_0} \approx 0.39$ [1]. Because of uncertainty in R, there is a systematic uncertainty of ~ 0.2 MHz in the Rydberg trap depth, which allows the crossover n between trapping and anti-trapping to vary between 56 and 63. Fixing it at $n = 62$ gives good agreement with a model with $w_0 = 650$ nm and $\alpha_c(532\text{ nm}) = 107$ a.u., within 12% of the value calculated in Ref. [112].

Next we study the state-dependent nature of the trapping potential by driving mi-

crowave transitions between Rydberg states following optical excitation to a $^3S_1$ state (Fig. 5.3). The shift of the microwave transition when the dipole trap is applied probes the differential polarizability of these states. The $^3S_1$ and $^3P_0$ states have nearly vanishing differential polarizability: on top of an estimated trap depth of 1.4 MHz, the transition frequency shifts less than 10 kHz. This is in agreement with a theoretical prediction that the $^1S_0$, $^3P_1$, and $^3P_0$ states should experience the same, purely scalar, ponderomotive potential, and the fact that the ion core polarizability is independent of the state of the Rydberg electron. In contrast, the $^3P_2$ state has a strong m_J-dependent shift arising from the rank-2 (tensor) component of the ponderomotive potential (Fig. 5.3b). Intuitively, this is caused by the different orientations of the m_J angular wavefunctions with respect to the tweezer potential, which is not spherically symmetric. The observed tensor shift of 300 kHz is close to the computed value of 400 kHz using the model parameters discussed above.

We have also measured the lifetimes of several P and D states, presented in Table 5.2. Near $n = 75$, the $^3P_2$ and $^1D_2$ lifetimes are similar to $^3S_1$, while the $^3P_0$ lifetime is nearly 10 times shorter, presumably because this series is very strongly perturbed [101]. However, both P and D states experience a moderate reduction in lifetime with increasing trap power, attributable to photo-ionization in agreement with previous calculations for Rb [57].

To demonstrate the utility of trapping Rydberg states for quantum simulation and quantum computing, we probe the coherence properties of a superposition of Rydberg levels. In Fig. 5.4a, we show Rabi oscillations between the $n = 74$ and $n = 75$ $^3S_1$ states, driven by a two-photon microwave transition detuned by 40 MHz from the $^3P_0$ intermediate state. The oscillations persist for more than 60 μs, more than twice the lifetime of an untrapped Rydberg atom. The coherence time is quantified using a Ramsey sequence (Fig. 5.4b) and found to be $T_2^* = 22\,\mu$s, which is in agreement with

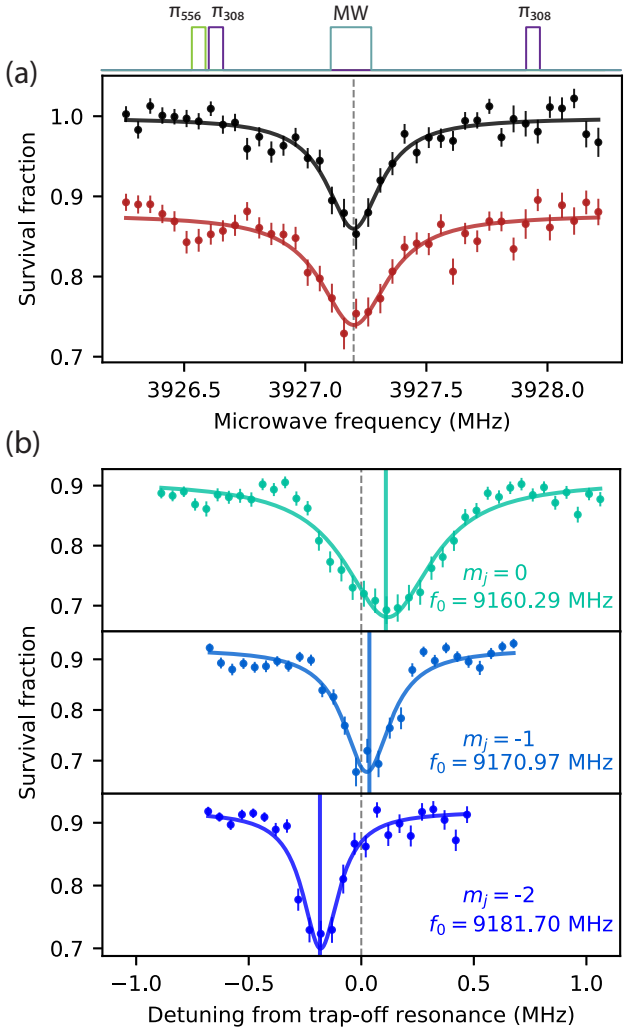

Figure 5.3: (a) Microwave spectrum of the $n = 75$ $^3S_1$ to $n = 74$ $^3P_0$ transition with (black) and without (red) the traps, demonstrating the magic trapping condition. The black data are shifted for clarity and the solid lines are Lorentzian fits. (b) Microwave spectra of the n=75 $^3S_1$ $m_j = -1$ to $n = 74$ $^3P_2$ $m_j = -2, -1, 0$ transitions, showing the tensor light shift of different m_j levels from the ponderomotive potential. For each transition, zero detuning indicates the measured transition frequency without the trap, indicated in the figure. The solid vertical lines show the predicted m_j^2 dependence of the tensor light shift.

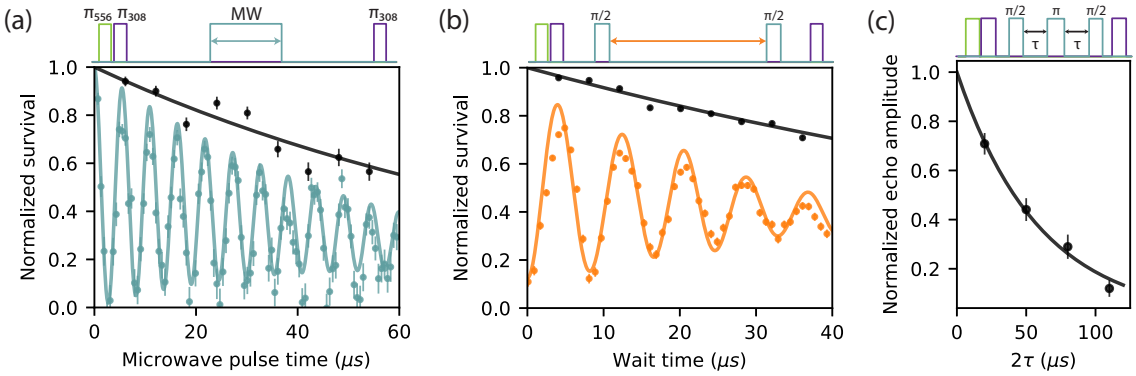

Figure 5.4: (a) Two-photon Rabi oscillations between $n = 75\ ^3\mathrm{S}_1$ and $n = 74\ ^3\mathrm{S}_1$. The solid line is a cosine fit with exponential decay time $\tau = 42\,\mu$s. Control data without microwave pulses (black data) shows T_1 for comparison. (b) Ramsey measurement of T_2^*. The orange line is a simulation that takes into account dephasing from the differential light shift between the two levels (90 kHz) and a finite atomic temperature (13 μK), yielding a $1/e$ decay time of $22\,\mu$s. (c) Hahn echo measurement. The black line is a exponential fit that yields $T_2 = 59\,\mu$s.

dephasing from thermal motion [120] for an atom with a temperature of $T = 13$ μK and the (measured) difference in the potential depth for the two states of 90 kHz. A Hahn echo sequence yields $T_2 = 59\,\mu$s, which is shorter than the limit $T_2 = T_1$ because the axial trap period is longer than T_1, so the revival in coherence is not reached (here, $T_1 = 108\,\mu$s is the lifetime of the upper *and* lower states).

These results demonstrate that trapping Rydberg states of alkaline earth atoms using the core polarizability can extend the coherence of quantum operations beyond what is possible with un-trapped atoms. This may lead to improved fidelities for quantum simulators and Rydberg gates, especially between distant atoms when the interaction is small. The expected improvement from trapping Rydberg states is most significant when the Rydberg lifetimes are very long, as expected for low-l states at cryogenic temperatures, and especially circular Rydberg states.

We conclude with a discussion of several aspects of these results. First, the coherence times in Fig. 5.4 are limited by a slight n-dependence of the trapping potential. While the ponderomotive potential itself is only weakly n-dependent, it contributes a large

fractional n-dependence when it is almost completely cancelled by the n-independent core potential near the crossover at $n \approx 60$. In future experiments where a higher degree of state-insensitive trapping is required, this can be improved by using higher n states or by pushing the crossover to lower n using shorter wavelength trapping light (to increase the core polarizability and decrease the ponderomotive potential) or smaller beam waist. Tuning the beam waist allows the precise potential for a particular Rydberg state to be manipulated, which may be advantageous for fine-tuning triply-magic trapping of ground, clock and Rydberg states, for example [121].

Second, we consider the prospect of trapping circular Rydberg states of Yb. The photoionization rate of the P and D states shortens their lifetime from their intrinsic values by 15-30% at a trap power of 9 mW per tweezer. However, for high-L states, including circular states, the photoionization cross-section is significantly smaller, ultimately decreasing exponentially with L [104]. The auto-ionization rate, while immeasurably small in our current experiments, should decrease as L^{-5} as the contact of the Rydberg electron with the core is suppressed [122]. Therefore, it seems likely that circular states may be trapped for extremely long times without adverse affects. Furthermore, transfer of orbital angular momentum from focused Laguerre-Gauss modes through the ponderomotive potential offers an intriguing new route to efficiently and rapidly exciting circular Rydberg states [116] or driving transitions between them.

5.3 Trap-induced loss mechanisms

5.3.1 Auto-ionization

The polarizability of the Yb^+ ion core primarily arises from the $6s$ to $6p_{1/2}$ and $6p_{3/2}$ transitions at 369 and 329 nm, respectively. For an optically trapped Yb^+ ion, the finite lifetime of these states ($1/\Gamma = 8$ ns for $6p_{1/2}$, [123]) would give rise to photon scattering at a rate $\Gamma\Omega^2/\Delta^2 = \Gamma U_0/\Delta$, where Ω and Δ are the Rabi frequency and

detuning of the trapping laser, and U_0 is the trap depth. In the case of a trapped Yb^0 Rydberg state, the trap laser can excite these ion core transitions from $6snl$ to $6p_jnl$ (where n, l are the quantum numbers of the outer Rydberg electron). Since these states are generally above the ionization limit of the $6snl$ series, they can rapidly auto-ionize. In an auto-ionization event, the core electron is de-excited by ejecting the Rydberg electron. The rate of this process decreases as $1/n^{*3}$, since the interaction between the Rydberg and core electron decreases as the former moves farther out. The rate of these events is the same as photon scattering for a Yb^+ ion, with the linewidth Γ replaced by the auto-ionizing linewidth $\gamma' n^{*-3}$, according to the isolated core electron approximation [124].

The auto-ionization rates have been measured for certain $5p_jns$ states in Sr [125] and $6p_jns$ states in Ba (cited in Ref. 21 of [125]) and Yb [126]. All are within the range of $\gamma' = 2\pi \times 10^{14}$ - $2\pi \times 10^{15}$ s^{-1}. The rate for the Yb $6p_{3/2}ns$ series has not been measured, but for concreteness we take the measured value for the $6p_{1/2}ns$ series of $\gamma' = 1.2 \times 10^{15}$ s^{-1} [126], and assume the $6p_{3/2}ns$ rate is 2 times higher, approximately the case for Sr and Ba. From this, we can estimate an auto-ionization rate of about $n^{*-3}\, 58 \times 10^6$ s^{-1} at typical trap powers (9 mW). This corresponds to a 7 ms lifetime at $n = 75$, which is insignificant on the timescale of our experiments. The rate should be even smaller for higher l states, since the overlap with the core decreases for high l. This is supported by measurements [124, 127] for $l < 7$ and theory predicting an l^{-5} scaling of the autoionization rate for high l [122].

5.3.2 Photo-ionization

Another loss mechanism is direct excitation of the Rydberg electron into continuum states, termed photoionization [128, 57]. Calculating this process requires computing matrix elements between bound and free Rydberg states, which requires either model potentials or extrapolation of measured bound state quantum defects into the contin-

state	Lifetime (μs)
$n = 74\ ^3P_2$	83(5)
$n = 74\ ^3P_0$	14(4)*
$n = 73\ ^1D_2$	75(18)
$n = 83\ ^1D_2$	59(3)
$n = 90\ ^1D_2$	60(3)
$n = 70\ ^3S_1$	85(4)
$n = 75\ ^3S_1$	105(3)
$n = 92\ ^3S_1$	42(2)

Table 5.2: Summary table of power dependent lifetime studies for various $^3\mathrm{P}_2$, $^3\mathrm{P}_0$, $^1D_2$, and $^3\mathrm{S}_1$ states, showing the extrapolated lifetimes with no trap-induced losses. *We do not have power dependence data to quote the extrapolated lifetime for $^3\mathrm{P}_0$, but give the value for 9 mW trap power.

uum [129]. The extrapolation quantum defects based on the Rydberg-Ritz model has been studied for alkali atoms [129]; however, given the very strong n-dependence near the ionization threshold observed for the Yb $^3P_0$ and $^3P_1$ states [101], a multi-channel quantum defect model would be necessary for a precise calculation of photo-ionization rates for Yb. Furthermore, it is possible to have perturbers above the ionization threshold that would not be evident from the bound state quantum defect series.

We instead determine the photoionization rates for a few S, P, and D states by measuring the Rydberg state lifetime as a function of trap power. Fig. 5.5a shows an example measurement for the $n = 74\ ^3\mathrm{P}_2$ state with the corresponding decay rates and a fit to $\Gamma = \Gamma_0 + \gamma_{PI}P$, where P is the trap power. Extrapolating the decay rates to zero trap power gives an estimate for the natural Rydberg state lifetimes $1/\Gamma_0$, which are summarized in Table 5.2. Fig. 5.5b shows the photoionization cross sections for the measured states, related to the decay rates by $\gamma_{PI}P = \sigma_{PI}I/\hbar\omega$. The measured photoionization cross sections are consistent with zero for the $^3\mathrm{S}_1$ series, but the rates are non-negligible for the $^3\mathrm{P}_2$ and $^1D_2$ states, resulting in a 15-30% reduction of the trapped lifetimes at typical trap powers. The observed magnitude and low-L dependence of the cross section is similar to previous calculations for Rb [57]. As with

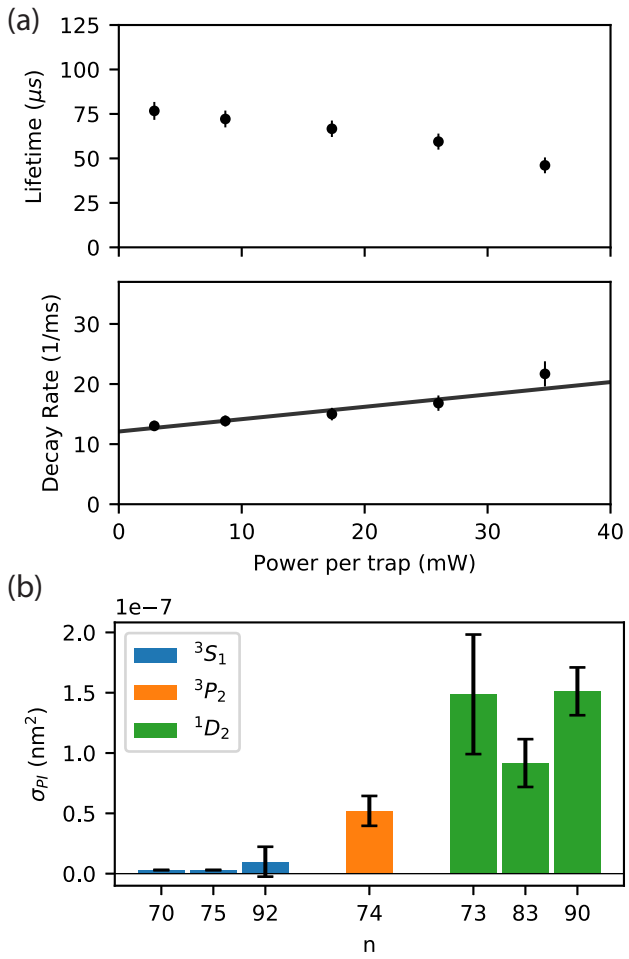

Figure 5.5: (a) Rydberg lifetimes vs. trap power for the $n = 74\,^3P_2$ state. The lower plot shows the corresponding decay rates and a linear fit, the slope of which determines the photoionization cross section σ_{PI}. (b) Measured photoionization cross sections for $^3S_1$, $^3P_2$, and $^1D_2$ states at different n. We see no evidence of photoionization for S states.

auto-ionization, the photoionization rate should decrease for high-L Rydberg states, in this case exponentially with L [104].

5.4 ^{3}S$_1$ Lifetime at high n

Given that we observe no trap-induced losses for the ^{3}S$_1$ series, the measured decrease in the ^{3}S$_1$ lifetimes at high n is surprising. For alkali atoms, the finite Rydberg state lifetime is a combination of spontaneous emission to much lower-n Rydberg states, and

blackbody-induced transitions between nearby Rydberg levels [16]. These rates scale as n^{*-3} and n^{*-2} respectively. Lifetimes of greater than 250 μs have been measured for Rb Rydberg states at $n = 85$ at room temperature [103]. In alkaline earth atoms, an additional loss mechanism is present: configuration interactions can mix Rydberg series attached to different ionization thresholds associated with different core ion states, which results in admixtures of fast-decaying low-n states into the high-n states. Rydberg state energies and lifetimes can be highly irregular near a perturbing resonance. Far from a resonance, however (e.g., at high n), the impact of the perturber is a constant factor reduction of the Rydberg series radiative lifetime [53]. Perturbers are almost certainly responsible for the measured, short lifetime of the $^3P_0$ series (Table 5.2), as this series is known to be extremely strongly perturbed [101].

Whether series perturbations are responsible for the drop in $^3\mathrm{S}_1$ lifetime at high-n is unclear. While the low-n $^3\mathrm{S}_1$ spectrum (Fig. 4.3) appears relatively unperturbed (compared to $^3\mathrm{P}_0$, for example, where the quantum defect varies by nearly 0.5 between $n = 30$ and $n = 80$), the deviation from constant δ at high-n could reflect an above-threshold perturber (or a technical artifact in the measurement, see Chapter 4). Another possibility is high-frequency electric field noise conducted to the atoms by a set of intra-vacuum electrodes around the atoms (described in Chapter 4). We have simulated the local density of states in the center of the electrodes at microwave frequencies and find low-Q resonances giving rise to Purcell enhancement factors of 2-3 at 7 and 15 GHz, where the strongest transitions lie for $n = 65 - 100$, which could enhance the blackbody transition rate by a similar factor or enhance the coupling of noise at these frequencies. This could also reduce high-n lifetimes for other series as well, but we do not have sufficient data on the n-dependence of the P and D series to confirm this. At present, we are unable to experimentally distinguish whether the high-n lifetimes are intrinsic or limited by technical effects.

Lastly, we note that the lifetime can in principle be extracted from MQDT analysis of the Rydberg spectrum. This has been attempted in some detail for Strontium [53]. In the case of Yb, this is hampered by the absence of complete spectroscopic data, the larger number of perturbers that result from low-lying f-shell excitations in the core (e.g., states of the form $4f^{13}5d6s$), and the fact that the lifetimes of the open f-shell states are not known in many cases. The lifetimes presented in this paper are, to the best of our knowledge, the first reported (or predicted) lifetimes for high-n Yb Rydberg states, which will aid future analyses.

Chapter 6

Controlling Rydberg Excitations

In order to implement high-fidelity quantum operations utilizing Rydberg interactions it is necessary to be able to drive high contrast Rabi oscillations between a ground qubit state and the relevent Rydberg state. In the work presented in Chapter 5, excitations to the Rydberg states were driven via a two-step process with initial single photon excitation from $^1S_0$ to $^3P_1$, followed by single photon excitation from $^3P_1$ to a $^3S_1$ Rydberg state. However, this process is highly susceptible to spontaneous emission out of $^3P_1$ leading to both inefficient transfer to the Rydberg state and rapid decoherence of oscillation contrast. The use of this technique was motivated by a high-noise 556 nm laser system.

In this chapter, using a lower noise 556 nm laser system (fixed by changing the probe laser source in the SFG process described in section 2.3.1), we demonstrate high contrast Rabi oscillations between $^1S_0$ and a $^3S_1$ Rydberg state via a two-photon excitation process using $^3P_1$ as an intermediate state, where spontaneous emission events are suppressed due to an intermediate state detuning. We also demonstrate the ability to controllably turn on and off excitations to the Rydberg state and Rydberg-mediated entanglement, via a new scheme that applies light shifts to the Rydberg

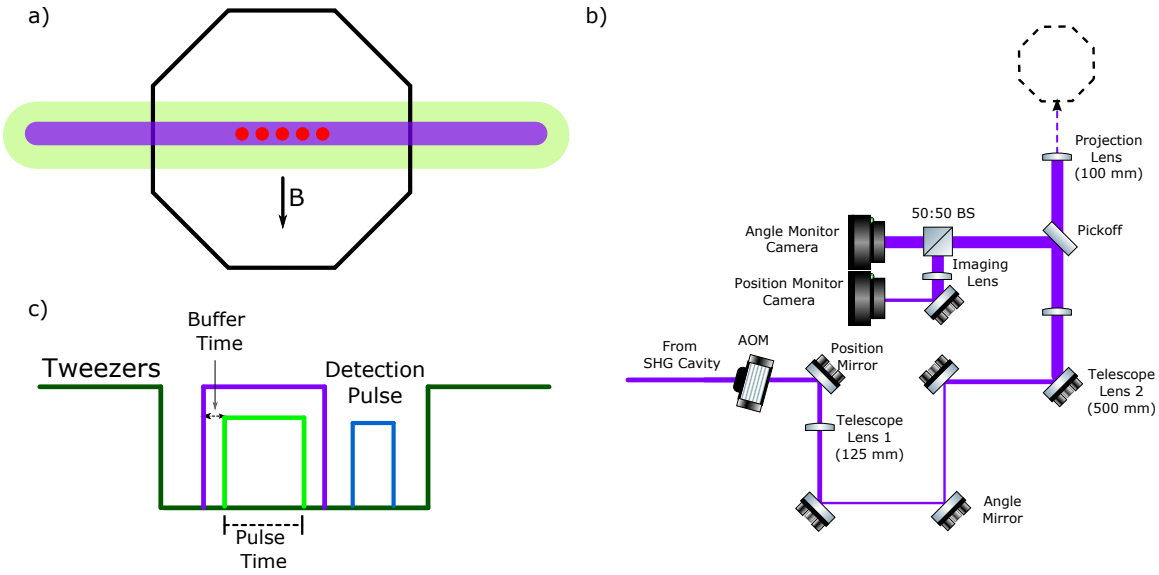

Figure 6.1: a) A schematic of the Rydberg excitation beam geometry in the science cell. b) A schematic of the UV beam optics. c) Diagram of pulse sequence for Rydberg excitation. The trap is turned off during excitation. The UV pulse is turned on before the start of the green pulse and turned off after the green pulse to correct for AOM frequency chirp.

state from a beam nearly resonant with the Yb^+ ion core transition (further details on this scheme and its potential advantages over other light-shifting control schemes are discussed in Section 6.2). This capability is promising for scalable implementation of local Rydberg gates in an Yb tweezer array.

6.1 Two-photon Rydberg excitation

We drive Rydberg excitations via a two-photon process using $^3\mathrm{P}_1\,(m_j = 1)$ as an intermediate state. We turn on a ∼3 G B-field orthogonal to the 1D tweezer axis, leading to ∼10 MHz splitting between m_j levels in $^3\mathrm{P}_1$. A 556 nm σ^+ beam is blue-detuned from $^3\mathrm{P}_1\,(m_j = 1)$ and directed along the axis of the 1D array, focused to a beam waist of $w_0 \approx 60$ μm. A counter-propagating 308 nm π beam, focused to a beam waist of $w_0 \approx 15$ μm is tuned to a two-photon resonance with a desired $\mathrm{n}^3\mathrm{S}_1\,(m_j = 1)$ Rydberg state. Fig 6.1a depicts the beam configuration.

The UV beam is aligned out of the doubling cavity in free space into the science cell. After going through an AOM for the purpose of pulsing the beam, it enters a 5x telescope to enlarge the beam size in order to achieve tighter focusing by a final 100mm lens into the science cell. The lens is on a motor-stage to adjust the focus in the science cell. In order to align the UV beam to the atoms we have two fine-control picomotor mirrors (Newport), one placed before the enlarging telescope to control the position of the beam in the science-cell and a second placed at the focus of the enlarging telescope to control the angle of the beam relative to the atom array. Two monitor cameras are used to monitor the position and angle of the beam, respectively. Fig 6.1b shows the UV beam optics.

To drive a two-photon Rydberg excitation we first pulse off the traps so as not to deal with variable light shifts from the tweezers on the ground and Rydberg state. The UV beam is then pulsed on for a time, $\tau_{\text{pulse}} + 2\tau_{\text{buffer}}$, and the green is turned on for time, τ_{pulse}, following a delay time of τ_{buffer} after the UV pulse is turned on. The buffer time is set to 200 ns and exists to correct for a frequency chirp effect from the UV AOM (described below). Then a 369 nm beam (overlapped with the UV beam), near-resonant with the ion core autoionizing transition is pulsed on to rapidly autoionize Rydberg atoms for readout. After the completion of the pulse sequence the traps are turned back on and a fluorescence image is taken, where Rydberg atoms are detected by the loss of an atom. The pulse sequence is shown in Fig 6.1c.

We drive two-photon Rabi oscillations between $^1S_0$ and the 75^3S_1 Rydberg state. While the majority of atoms that are excited to the Rydberg state are typically lost from decay into anti-trapped states prior to imaging, there is a considerable probability ($\sim$15-20%) that Rydberg atoms decay back to the ground state and are detected via fluorescence imaging. In order to eliminate this detection error we illuminate the atoms with a beam that rapidly autoionizes Rydberg atoms causing Rydberg atoms

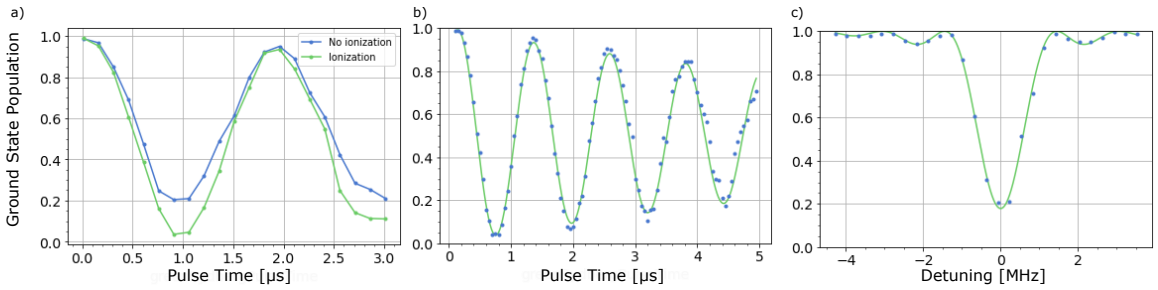

Figure 6.2: a) Rabi oscillations with and without the ionization pulse, demonstrating the imperfect Rydberg state detection without the ionization pulse. b) High contrast two-photon rabi oscillations between the ground and Rydberg state shown to longer times than in (a). We measure the ground state population versus two-photon pulse time. The green curve is a fit to an oscillating sine function with a exponentially decaying envelope. b) Two-photon spectrum of Rydberg state. We measure the ground state population versus UV frequency at pulse time $t < t_\pi$. The green curve is a fit to an analytical model of a detuned-Rabi oscillation.

to be lost with near unity probability [50, 63]. Fig. 6.2a shows the ground state population as a function of two-photon excitation pulse length with and without the ionization pulse, demonstrating the imperfect Rydberg state detection without the ionization pulse. Fig. 6.2b shows the high contrast oscillations out to longer pulse times. Further details of the autoionizing transition are discussed in the latter part of Chapter 6.

We measure the resonance of the two-photon transition by setting the two-photon excitation pulse to a time, $\tau < \tau_\pi$, and measuring the ground state population as a function of the UV laser frequency. A characteristic spectrum is shown in 6.2b. Surprisingly, across an array of 20 atoms we see significant inhomogeneity ($\sim$2 MHz across the array) in the single site two-photon resonances (shown in Fig 6.3a). We first consider the possibility that this inhomogeneity is due to an electric-field gradient across the array. However, we find that the frequency gradient is independent of electrode voltage, while we would expect a frequency gradient caused by an electric field gradient to be linear in the average electric field (due to the quadratic dependence of the DC Stark shift). We also consider the possibility that the inhomogeneity is

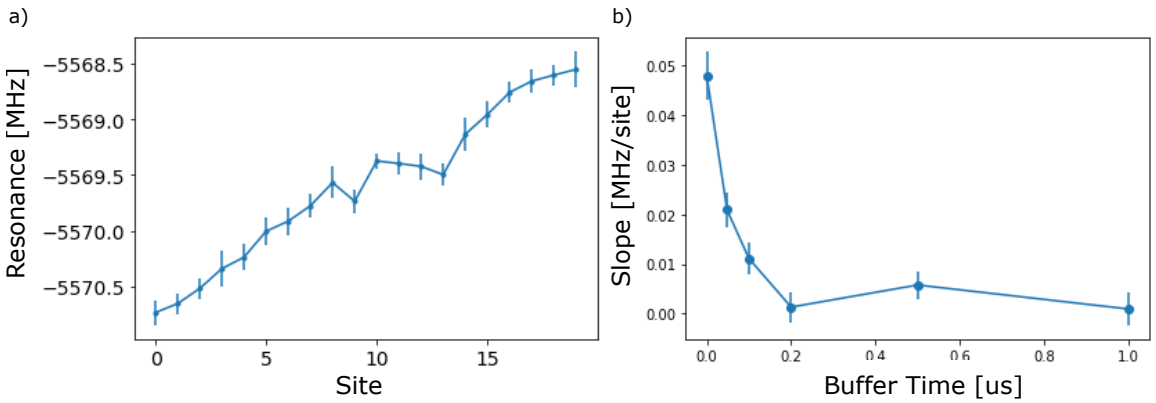

Figure 6.3: a) UV two-photon resonance as vs array site demonstrating inhomogeneity of roughly 2 MHz across the array. The absolute measurement of the resonance is arbitrary. b) Dependence of inhomogeneity across the array measured in slope of the resonance vs site (MHz/site) on the UV pulse buffer time (This data was taken when the angular misalignment of the UV beam was less severe leading to smaller inhomogeneties at zero buffer time compared to the data in (a)). At buffer times of 200 ns or greater the inhomogeneity in the UV resonance across the array is no longer present.

due to variable light shifts from the Rydberg excitation beams if the observed beam intensity varies across the array. However, the magnitude of the inhomogeneity is much greater than one would expect from independent measurements of the light shift from each beam and measurements of the intensity variation across the array from site-dependent measurements of the Rabi frequency (less than a few %)

We instead theorize that the inhomogeneity is caused by a frequency chirp effect from the UV AOM. Due to finite rise-time effects from the UV AOM one side of the UV beam will be turned on prior to the other side. If the axis of beam propagation is aligned with the atom array then the optical path length from either side of the beam will be equivalent. However, if the axis of beam propagation is slightly misaligned from the atom array axis then the optical path length from either side of the beam will be different. Thus, as the AOM turns on, the phase of the light seen by the atoms will change as the full aperture of the lens is illuminated. Since the difference in optical path lengths across the UV beam will vary across the array this can be the

cause of the two-photon resonance inhomogeneity. An ideal solution to the problem is to ensure that the UV beam is perfectly aligned relative to the atom array, however, this process is time-consuming and slow alignment drifts of the beam could cause the problem to persistently return. Instead we solve the inhomogenity with a UV pulse buffer, so that the UV beam is turned on and off with a 200 ns buffer time relative to the green pulse. This solves the issue because the finite rise-time effects of the UV AOM have already occurred before the two-photon excitation begins, at no cost in terms of photon scattering since there is no population in either $^3P_1$ or the Rydberg state. The inhomogeneity across the array as a function of the UV pulse buffer time is shown in Fig. 6.3b. For buffer times 200 ns or longer the inhomogeneity in the UV resonance across the array disappears.

6.2 Rydberg control with light shifts from ion core transition

The remaining work discussed in this chapter will also be presented in a manuscript currently in preparation: A.P. Burgers, S. Ma, S. Saskin, J. Wilson, M. Alarcon, C. Greene, J.D. Thompson, "Controlling Rydberg excitations using ion core transitions in alkaline earth tweezer arrays"

An outstanding challenge in the field of quantum computing and programmable simulation with Rydberg atom arrays is scalable, local addressing of gate operations, especially for two-qubit gates. Generating rapidly switchable, reconfigurable and focused Rydberg excitation beams across an array is demanding for optical modulators, as the intensity, pointing and frequency of these beams must be tightly regulated. This challenge is exacerbated for the wavelengths needed for single-photon Rydberg excitation (near or below 300 nm [130, 131, 50]), for which very few optical materials are transparent.

An alternative approach is to apply local light shifts with non-resonant control beams, to tune the ground to Rydberg ($|g\rangle \rightarrow |r\rangle$) transition on individual sites out of resonance with a global Rydberg excitation beam (Fig. 6.4a). Local control with light shifts has been demonstrated with Rydberg arrays [132, 59, 133], and with microwave transitions in optical lattices [134, 135]. In the case that the qubits are encoded in hyperfine ground states, this local control over excitation to the Rydberg state determines which atoms participate in the gate. To avoid spurious interactions with spectator atoms, the magnitude of the light shift must be much larger than the global Rydberg Rabi frequency, Ω_r. At the same time, photon scattering from the hyperfine levels must be suppressed to avoid gate error. Balancing these conditions requires a large detuning of the control beam to achieve high fidelity operations.

However, we point out that the scattering error can be significantly reduced if the control beam only couples to the Rydberg state, $|r\rangle$ (Fig. 6.4b). In this case, the scattering errors occur primarily from $|r\rangle$, but the population of this state is suppressed for atoms illuminated by the control beam, which remain in the ground state. As a consequence, the control beam can be operated at much smaller detunings and lower powers.

Unfortunately, in alkali atoms such as Rb and Cs, there are no strong optical transitions connected to $|r\rangle$. In alkaline earth atoms (AEAs) with two valence electrons, the situation is different: the Rydberg electron orbits an optically active ion core, which has strong, allowed transitions. The far off-resonance polarizability of these transitions has been used for trapping Yb [136] and Sr [111] Rydberg atoms, while the short lifetime (via autoionization decay) of core excited states has been used for efficient state detection in Sr atomic gases [63] and tweezer arrays [50].

In this work, we theoretically quantify the control field intensity I_c needed to realize locally addressed operations with an error rate ϵ by shifting the ground states or the

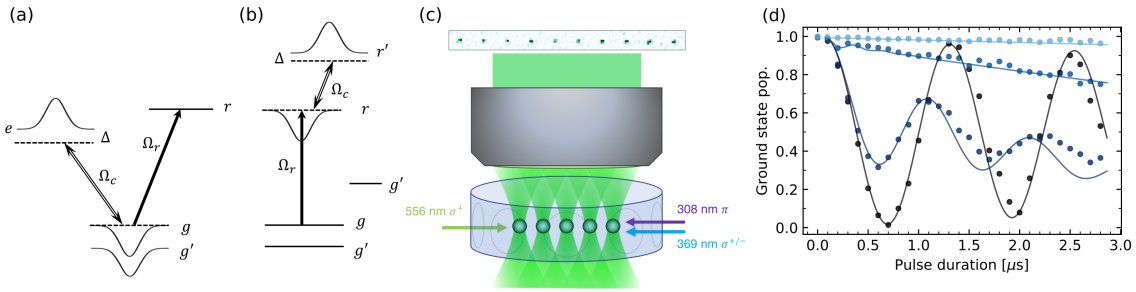

Figure 6.4: (a) In the conventional approach to local control with light shifts, the $|g\rangle \rightarrow |r\rangle$ transition is detuned by a light shift generated by the $|g\rangle \rightarrow |e\rangle$ transition. (b) In another approach, studied here, the light shift is generated on a transition from $|r\rangle$ to $|r'\rangle$. (c) Schematic of the experiment, indicating the propagation direction and polarization of the two-photon Rydberg excitation (556 nm + 308 nm) and the control beam (369 nm). The Rydberg and control beams are focused to approximately 15 μm $1/e^2$ radius. (d) Applying increasing control beam intensities (black to blue: $I_c =$ 0, 15, 90, 601 W/cm^2) suppresses Rabi oscillations between $|g\rangle$ and $|r\rangle$. Here, the control beam is detuned by $\Delta = -5$ GHz from the $|r\rangle \rightarrow |r'\rangle$ transition. The solid lines show the result of a numerical simulation.

Rydberg states, and find that scaling is improved from $I_c \propto 1/\epsilon^3$ to $I_c \propto 1/\epsilon^2$ in the latter case. We then experimentally demonstrate control of Rydberg excitations in an optical tweezer array of ^{174}Yb atoms [81, 136] using a light shift induced on the Rydberg state by a control beam tuned near the 369 nm $6s \rightarrow 6p_{1/2}$ transition in the Yb$^+$ ion core. We investigate the influence of the control beam on the $6sns$ $^3S_1$ Rydberg states in detail, and find that, near resonance, the light shift and autoionization loss rate can be explained with a two-level system model consistent with the isolated core electron (ICE) approximation for doubly excited Rydberg states [137]. We then use the control beam to switch *on* and *off* the excitation of single atoms and high-fidelity ($\mathcal{F} > 0.948$) Bell states in a dimerized array, using a control beam intensity equivalent to only 1.3 μW in a diffraction-limited spot. Lastly, we observe that for larger control beam detunings (comparable to the spacing between Rydberg levels), satellite features called "shake-up" lines [138] appear, giving rise to an additional enhancement or suppression of the loss rate without altering the light shift. We demonstrate an additional reduction in scattering errors from the control beam

at these special detunings.

These results suggest a new direction for implementing scalable, locally addressed multi-qubit gate operations in AEA tweezer arrays. While ^{174}Yb does not support a qubit in the $^1S_0$ ground state, this technique could be applied to control quantum gates on qubits encoded on the clock transition ($^1S_0 \rightarrow^3 P_0$) or in the hyperfine state of an odd isotope (*i.e.* ^{171}Yb or ^{87}Sr). The latter has the particular advantage that both the photon scattering rate and differential light shift on the qubit levels are extremely small. Therefore, a simple, binary amplitude modulator should be sufficient to control which sites are resonant with a global (or weakly focused) Rydberg beam, enabling efficient local control of entangling operations.

We first establish the theoretical scaling of the addressing fidelity with the intensity of the control light. We consider the following scenario: given a regular array of atoms with qubits encoded in hyperfine ground states (Fig. 6.4a), we wish to apply an entangling Rydberg blockade gate using a global Rydberg beam Ω_r [139, 140] to a sparse subset of nearest-neighbor qubit pairs, while realizing no operation (up to single-qubit phases) on the remaining, spectator qubits. Given a control beam that shifts the ground states of the spectator atoms relative to $|r\rangle$ by an amount $\Delta_{LS} = \Omega_c^2/(4\Delta)$, and induces a scattering rate $\Gamma_{LS} = \Gamma\Omega_c^2/(4\Delta^2)$ [1] (see Fig. 6.4a for variable definitions), there are two dominant errors. The first is the probability for a spectator atom to be excited off-resonantly to $|r\rangle$, $P_r \propto (\Omega_r/\Delta_{LS})^2$, and thereby blockade the intended gate, which results in an error probability $\epsilon_{rot} \propto P_r$. The second is a photon scattering error in the spectator atom, with a probability $\epsilon_{sc} = \Gamma_{LS} t_g$ ($t_g \approx 2\pi/\Omega_r$ is the gate duration). We note that the former error is improved with larger control field intensity, while the latter gets worse, resulting in a minimum total

[1] This is the total scattering rate including both Raman and Rayleigh scattering, but we treat it as Raman scattering when $\Delta < \Delta_f$, the fine structure splitting [141]. Given the required value of Δ derived below, this is self-consistent for gate errors $\epsilon \gtrsim 10^{-4}$ in Rb and Cs, given $\Delta_r/\Gamma \approx 10^6$ in these atoms.

error that can only be reduced by increasing Δ.

There is also an intrinsic gate error on the un-shifted qubits resulting from the finite lifetime of the Rydberg state, $\epsilon \approx t_g\Gamma_r = 2\pi\Gamma_r/\Omega_r$, where Γ_r is the decay rate of $|r\rangle$. A natural condition is that the addressing errors should be comparable to the intrinsic error, $\epsilon_{rot} + \epsilon_{sc} = \epsilon$, and the minimum Δ and I_c needed to realize this are $\tilde{\Delta} \propto \Gamma/\epsilon^{3/2}$, and $\tilde{I}_c \propto |\tilde{\Omega}_c|^2 \propto \Gamma\Gamma_r/\epsilon^3$.

If the light shift is applied on the state $|r\rangle$ by coupling to another state $|r'\rangle$ (Fig. 6.4b), the spectator qubit error probability ϵ_{rot} is the same but the scattering error is strongly suppressed since only the $|r\rangle$ state experiences loss. In this case, $\epsilon_{sc} = \Gamma_{LS}t_gP_r$, with $P_r \propto \epsilon_{rot}$ as before. Since $\epsilon_{rot} \propto \Omega_c^{-4}$ and $\Gamma_{LS} \propto \Omega_c^2$, both errors now decrease monotonically with increasing control power. The condition $\epsilon_{rot} + \epsilon_{sc} = \epsilon$ can be satisfied with $\tilde{\Delta} \propto \Gamma/\sqrt{\epsilon}$, and $\tilde{I}_c \propto |\tilde{\Omega}_c|^2 \propto \Gamma\Gamma_r/\epsilon^2$. An additional benefit of shifting $|r\rangle$ is that no single-qubit phases accrue on the spectator atoms, which makes the gate operation insensitive to variations in I_c.

We now turn to an experimental demonstration of controlling Rydberg excitations by shifting $|r\rangle$ on an ion core transition. Our experiment begins by creating a 1D, defect-free array [142, 143] of 10 ^{174}Yb atoms in the $^1S_0$ ground state $|g\rangle$. This state is coupled to the $6s75s\,^3S_1$ ($m_J = -1$) Rydberg state $|r\rangle$ in a two-photon process via the $^3P_1$ state, with an intermediate state detuning of 25 MHz and two-photon Rabi frequency $\Omega_r = 2\pi \times 0.7$ MHz. The 369 nm control beam with intensity I_c is co-propagating with the Rydberg lasers, and is stabilized near the $|r\rangle \rightarrow |r'\rangle$ transition using a wavemeter with 60 MHz accuracy. At the end of the experiment any population in $|r\rangle$ blown away by a a second pulse of the 369 nm beam, at full power, before detecting the remaining atoms in $|g\rangle$ [50] (without this pulse, approximately 20% of atoms in $|r\rangle$ return to $|g\rangle$ before detection).

The essential result is illustrated in Fig. 6.4d. With the control beam turned off,

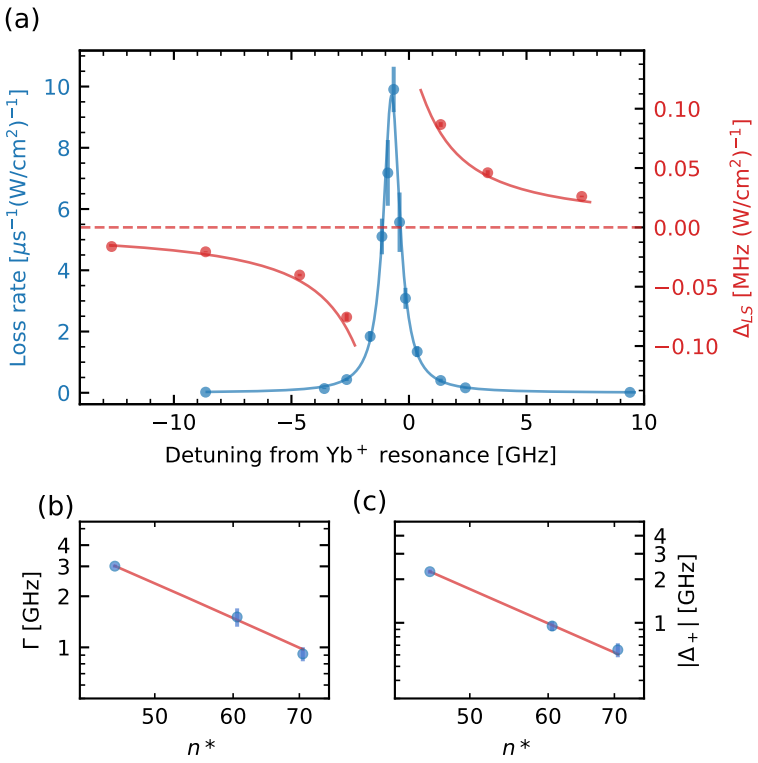

Figure 6.5: (a) Δ_{LS} and Γ_{LS} for the $6s75s$ $^3S_1$ state, as a function of the control beam detuning from the Yb^+ $6s \rightarrow 6p_{1/2}$ transition frequency, f_+. The fits show a comparison to a two-level model, with $\Delta = f - (f_+ + \Delta_+)$. (b) The extracted linewidth, Γ and (c) center frequency offset Δ_+ as a function of n^*, with a fit to $(n^*)^{-3}$ overlaid.

we observe Rabi oscillations between $|g\rangle$ and $|r\rangle$ with a high visibility. Applying the control beam with successively higher intensities, these oscillations become damped and eventually cease, leaving the atoms in $^1S_0$. The control light is detuned by $\Delta = -5$ GHz from the $|r\rangle \rightarrow |r'\rangle$ transition. The absence of loss from autoionization of $|r'\rangle$ directly illustrates the suppression of loss resulting from light shifting $|r\rangle$ instead of $|g\rangle$. We note that the highest I_c, 600 W/cm^2, is equivalent to only 1.3 μW in a diffraction-limited spot with $w_0 = \lambda$.

To better understand and quantitatively model the properties of the $|r\rangle \rightarrow |r'\rangle$ transition, we measure the light shift and loss rate of $|r\rangle$ as a function of the detuning, Δ, of the 369 nm beam from the Yb^+ resonance at $f_+ = 811.29150(40)$ THz (Fig. 6.5a)

[144]. The light shift, Δ_{LS}, is extracted from the resonance shift of the $|g\rangle \rightarrow |r\rangle$ transition when the 369 nm light is applied at an intensity of $I_c = 50$ W/cm^2. The loss rate, Γ_{LS}, is measured through the population decay from $|r\rangle$ after a variable duration 369 nm pulse with intensity $I_c = 0.67$ W/cm^2. We have experimentally verified that both the light shift and loss rate are linear in intensity over a wide range. We also note that the peak loss rate of 6.65 μs^{-1}/(W/cm^2) is more than 100 times faster than what was reported in Ref. [50] for the Sr $5s61s \rightarrow 5p_{3/2}ns$ transition.

The data is well-described by a two-level system model, $\Delta_{LS} = \Omega_c^2\Delta/(4\Delta^2 + \Gamma^2)$ and $\Gamma_{LS} = \Gamma\Omega_c^2/(4\Delta^2 + \Gamma^2)$. From a fit, we extract the parameters $\Delta = f - (f_+ + \Delta_+)$ and $\Gamma = 2\pi \times 0.92(3)$ GHz. The transition is centered at a frequency $\Delta_+ = -0.73(7)$ GHz, slightly below the Yb$^+$ transition frequency (the uncertainty arises from the accuracy of the wavemeter and the literature value of f_+). This is consistent with a quantum defect of the $6p_{1/2}ns\ ^3P_{J'}$ Rydberg series that is larger than that of $6sns\ ^3S_1$ ($\delta = 4.438$ [136]) by 0.035 (modulo 1). Note that based on the $\sigma^{+/-}$ polarization of the 369 nm light, both the $J' = 1$ and $J' = 0$ autoionizing states are excited, and cannot be distinguished within our measurement.

Based on the known intensity, a dipole moment d can be extracted from the fit to Δ_{LS} or Γ_{LS}. The value from Γ_{LS} is $d = 1.46(2)\, ea_0$, which is consistent with the literature value for the Yb$^+$ transition using $\Gamma = 1/8.12$ ns^{-1} and taking into account the Clebsch-Gordan coefficient for the control beam polarization [145]. Curiously, the value of d extracted from Δ_{LS}, $d_{\Delta_{LS}} = 1.08(3)\, ea_0$, is approximately 25% lower than that for Γ_{LS}, which we do not understand at the present time.

We have repeated these measurements at $n = 50$ and 65 to understand the scaling properties of these parameters. Both $|\Delta_+|$ and Γ scale as $1/n^{*3}$ as expected (Fig. 6.5b and c) [138]. The coefficient for Γ, $2\pi \times 2.9 \times 10^{14}\,\mathrm{s}^{-1}$, is approximately 50% larger than a previous measurement for the Yb $6p_{1/2}ns\ ^1P_1$ series [146] but within

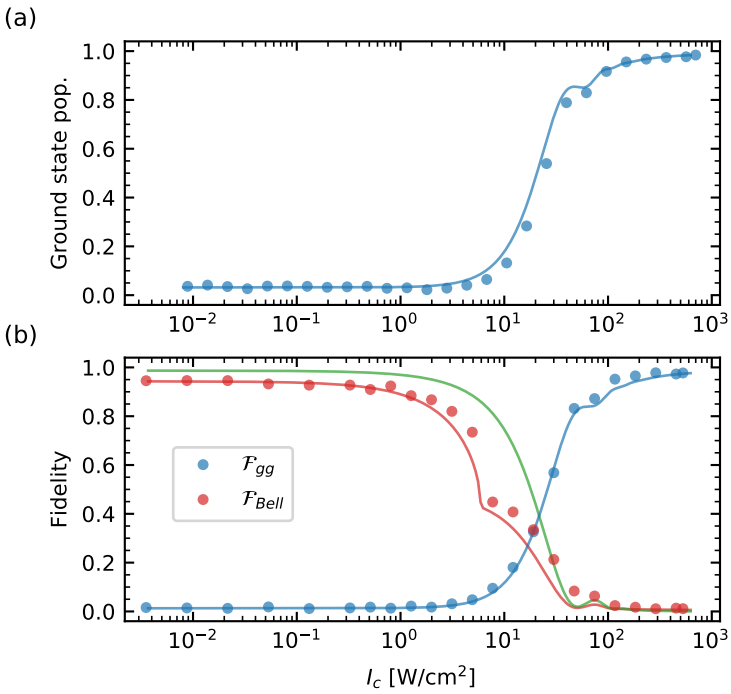

Figure 6.6: (a) Probability to find an atom in $|g\rangle$ after a π pulse to $|r\rangle$, for varying control intensities I_c with $\Delta = 5$ GHz. At high intensities, the population transfer is strongly suppressed and 99% of the atoms remain in $|g\rangle$. (b) Final state fidelity with $|\phi^+\rangle$ (red: lower bound, green: simulated exact fidelity) and $|gg\rangle$ (blue) after a π pulse in a dimerized array with a strong intra-dimer Rydberg blockade. The control beam switches the final state from having $> 94.8\%$ fidelity with $|\phi^+\rangle$, to 98% fidelity with $|gg\rangle$. In both plots, the curves show simulations using parameters from Fig. 6.5a and a phenomenological dephasing to match the observed oscillation visibility.

the range of values for similar series in Sr [137] and Ba [147].

We now study the effectiveness of the control beam at modulating Rydberg excitation induced by Ω_r, in the case of isolated, non-interacting atoms (Fig. 6.6a). To do this, we apply Ω_r for a time $t_g = \pi/\Omega_r \approx 700$ ns (π-pulse), while varying the control beam intensity I_c. The control beam detuning is fixed at $\Delta = -5$ GHz. In this experiment, the atoms are spaced by $d = 21\,\mu$m, such that the van der Waals interaction is negligible compared to Ω_r. In the absence of the control beam, around 97% of the ground state population is transferred to $|r\rangle$, limited by residual technical noise, Doppler shifts and photon scattering. However, at the maximum intensity of 699

W/cm^2, the Rydberg excitation is suppressed and the atoms remain in $|g\rangle$ with 99% probability. The data is in excellent agreement with a numerical simulation based on parameters extracted from Fig. 6.5a.

Next, we demonstrate control over coherent excitations in the Rydberg blockade regime using a dimerized array (Fig. 6.6b). The intra-dimer spacing is 3.15 μm, for which we estimate a blockade strength $V = 1.2$ GHz. We apply a Ω_r for a time $t_g = \pi/(\sqrt{2}\Omega_r) = 495$ ns, which drives a π pulse on the blockaded transition $|gg\rangle \rightarrow |\phi^+\rangle = (|gr\rangle + |rg\rangle)/\sqrt{2}$. When $I_c = 0$, we extract a lower bound of the state fidelity (with respect to the Bell state) of $\mathcal{F}_\phi > 0.948$, using the state purity after a $2t_g$ pulse (following Ref. [50]). However, at the maximum I_c, the oscillations are highly suppressed and the fidelity with the starting state is $F_{gg} = 0.98$.

Lastly, we study the the loss rate and light shift over a broader range of control beam detunings. Near the transition to other Rydberg states, such as $6s75s \rightarrow 6p_{1/2}74s$ (approximately $\Delta = -19$ GHz below the transition to $6p_{1/2}75s$), the loss rate shows sharp, Fano-like features (Fig. 6.7a) known as "shake-up" resonances [138]. These features can be qualitatively reproduced with a model based on the overlap integral of the Rydberg electron wavefunction in the initial and final states, with the minimum occurring at the energy where the final state Rydberg electron wavefunction is orthogonal to the initial state [148]. A somewhat improved fit can be obtained with a multichannel MQDT model. Experimentally, we observe a dip in the loss rate that is a factor of ~ 34 below the value predicted by the two-level model shown in Fig. 6.5.

Importantly, the light shift does not show any irregular behavior near the shake-up resonance. Therefore, operating the control laser at detuning corresponding to the scattering minimum (Δ_{min}) is beneficial, reducing ϵ_{sc} or allowing the same total addressing error $\epsilon_{rot} + \epsilon_{sc}$ to be realized with less power. We experimentally demonstrate

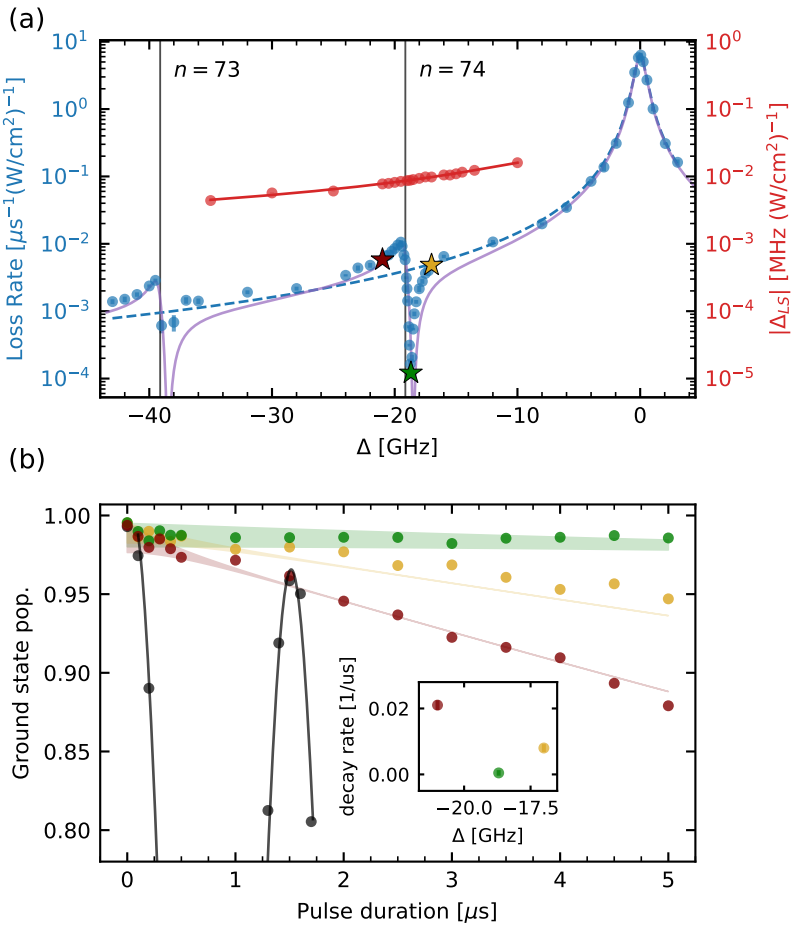

Figure 6.7: (a) Δ_{LS} (red) and Γ_{LS} (blue) for the $6s75s\ ^3S_1$ state, as in Fig. 6.5 but over a broader range of detunings. The positions of the $6p_{1/2}ns$ states (black lines) and the detuning that minimizes the loss rate $\Delta_{min} = -18.7$ GHz (green star) are indicated. (b) Rabi oscillations to $|r\rangle$ (black, $I_c = 0$) are strongly suppressed by applying the control field at detunings near Δ_{min} [colors correspond to starred points in panel (a)]. Population loss from autoionization is suppressed to less than 0.06% per π-pulse when $\Delta = \Delta_{min}$.

the reduction in ϵ_{sc} by simultaneously applying Ω_r and the control light for a long duration (t $\approx 7\pi/\Omega_r$), at three detunings near Δ_{min} (Fig. 6.7b). The light shift ($\Delta_{LS} \approx 5.8 - 4.6$ MHz) suppresses coherent oscillations to around 1% for each detuning. However, there is a gradual population loss from ϵ_{sc} that is linear in Γ_{LS}, and we find that this loss vanishes, within our experimental resolution, at Δ_{min}. The behavior is in agreement with a master equation simulation, where the shake-up resonance is incorporated as a reduction in Γ to match the experimentally measured Γ_{LS}

at each detuning in Fig. 6.7a.

We have demonstrated that a light shift of the excited Rydberg states using a core electron transition can be used to control Rydberg excitations in an optical tweezer array. In contrast to applying a light shift on the ground state, shifting the Rydberg state has reduced laser power requirements to achieve a given error rate from photon scattering or off-target excitation. This demonstration was carried out with a global control laser, however, the main application of this result will be with locally addressed control fields, and using the ^{171}Yb isotope with qubits encoded in the nuclear spin sublevels of the $J = 0$ states $^1S_0$ or $^3P_0$. This approach has the additional benefit that the qubit states experience negligible differential light shift from the control field, significantly relaxing the technical demands for local control.

6.3 Measuring Autoionization Rabi Frequency

6.3.1 Determining Ω_c

For the data in Fig 6.6 we determine the control beam Rabi frequency by measuring the loss rate at the desired detuning ($\Delta = -5$ GHz) for different powers of the control beam. Using $\Gamma_{LS} = \Gamma\Omega_c^2/(4\Delta^2 + \Gamma^2)$, we extract Ω_c directly from the loss rate for high powers. From this trend of Ω_c vs power we interpolate the Rabi frequency at low powers where the autoionization loss rates are too slow to measure directly using our method described in the text.

6.3.2 Notes on estimating Ω from dipole matrix element

We start with $H = -\mathbf{d} \cdot \mathbf{E}$, where $\mathbf{d} = -e\mathbf{r}$ and the electric field $\mathbf{E}$ with polarization $\hat{\varepsilon}$ is

$$\begin{aligned}\mathbf{E} &= \hat{\varepsilon} E_0 \cos\omega t \\ &= \hat{\varepsilon}\frac{E_0}{2}(e^{-i\omega t} + e^{i\omega t}).\end{aligned}$$

After assuming a two level system with levels $|g\rangle$ and $|e\rangle$ and making the rotating wave approximation, this Hamiltonian can be written as (Ref [149] 5.18)

$$\begin{aligned}H &= -\langle g|\,\hat{\varepsilon}\cdot\mathbf{d}\,|e\rangle\,\frac{E_0}{2}(\sigma e^{i\omega t} + \sigma^\dagger e^{-i\omega t}) \\ &= \frac{\hbar\Omega}{2}(\sigma e^{i\omega t} + \sigma^\dagger e^{-i\omega t}).\end{aligned}$$

The Rabi frequency is then given by

$$\Omega = \frac{-\langle g|\,\hat{\varepsilon}\cdot\mathbf{d}\,|e\rangle\,E_0}{\hbar}.$$

There are two factors of 2, one from the $\Omega/2$ matrix element in the Hamiltonian (so that the populations in $|g\rangle$ and $|e\rangle$ oscillate at frequency Ω), and another from the fact that the positive and negative electric field components have amplitude $E_0/2$. These cancel out in the expression for Ω.

The relationship between the dipole matrix element (Ref. [149] 5.242) and decay rate is

$$d_0^2 = |\,\langle g|\,\mathbf{d}\,|e\rangle\,|^2 = \frac{3\pi\epsilon\Gamma\hbar c^3}{\omega^3}.$$

In our case, we have a linearly polarized 369 beam effectively driving the σ^+ and σ^- transitions from $^2S_{1/2}$ to $^2P_{1/2}$ in the Yb^+ ion. The CG coefficients for the $^2P_{1/2}$ $m_j = 1/2$ state are $\sqrt{2/3}$ for $|m_l = 1, m_s = -1/2\rangle$ and $\sqrt{1/3}$ for $|m_l = 0, m_s = 1/2\rangle$

so there is an extra factor of $\sqrt{2/3}$ for the sigma transitions, $d = \sqrt{\frac{2}{3}}d_0$. Estimate the electric field amplitude E_0 from $E_0^2 = \frac{4P_0}{\pi\epsilon c w^2}$.

Numbers: We have $P_0 = 2$ mW in the 369 nm beam focused to a waist $w = 15$ μm. We lose a factor of two here since the power is evenly split between σ^+ and σ^- polarizations. With $\Gamma = 1/(8.12\ ns)$, this gives $\Omega \approx 2\pi\times$ 840 MHz.

6.4 Simulations

6.4.1 Single Atom

We solve the master equation for the following Hamiltonian:

$$H_1 = \frac{\Omega_r}{2}(\sigma^+_{r,g} + \sigma^-_{r,g}) + \frac{\Omega_c}{2}(\sigma^+_{r,r'} + \sigma^-_{r,r'}) - \Delta_c P_{r'} \tag{6.1}$$

We also include an additional state, $|\Psi_d\rangle$, in the Hilbert space to simulate the case in which an atom scatters out of the autoionizing state. Thus we include the collapse operator $c_1 = \sqrt{\Gamma_{\text{ai}}}\sigma^-_{r',d}$. We also include an additional collapse operator, $c_2 = \sqrt{\Gamma_{\text{dephase}}}\sigma^z_{g,r}$ to account for dephasing during Rabi oscillations between the ground and Rydberg state. The dephasing rate, Γ_{dephase}, is chosen such that the ground state population after a π-pulse in simulation, $P_g(t = \pi/\Omega_r)$ agrees with our measured, P_g, during a π-pulse.

We simulate $P_g(t = \pi/\Omega_r)$ as a function of the auto-ionizing Rabi frequency, Ω_c. In order to account for imperfect ground state detection we compare $P_g(t = \pi/\Omega_r) * F_g$ with our measured P_g, where F_g, is the ground state detection fidelity.

6.4.2 Two atom blockade

We solve the master equation for the two-atom Hamiltonian:

$$H_2 = H_1 \otimes \mathbb{1} + \mathbb{1} \otimes H_1 + U_{\text{int}} P_r \otimes P_r \tag{6.2}$$

We now have four collapse operators: $c_1 = \sqrt{\Gamma_{\text{ai}}}\sigma^-_{r',d} \otimes \mathbb{1}$, $c_2 = \sqrt{\Gamma_{\text{ai}}}\mathbb{1} \otimes \sigma^-_{r',d}$, $c_3 = \sqrt{\Gamma_{\text{dephase}}}\sigma^z_{g,r} \otimes \mathbb{1}$, $c_4 = \sqrt{\Gamma_{\text{dephase}}}\mathbb{1} \otimes \sigma^z_{g,r}$.

We simulate $P_{gg}(t = \pi/(\sqrt{2}\Omega_r))$ and extract a simulated bell-state Fidelity lower bound (method from Ref. [50]) from the simulated populations $P_{gr}((t = \pi/(\sqrt{2}\Omega_r))$, $P_{rg}((t = \pi/(\sqrt{2}\Omega_r))$, $P_{gg}((t = 2\pi/(\sqrt{2}\Omega_r))$, $P_{gr}((t = 2\pi/(\sqrt{2}\Omega_r))$, $P_{rg}((t = 2\pi/(\sqrt{2}\Omega_r))$, $P_{rr}((t = 2\pi/(\sqrt{2}\Omega_r))$ as a function of the auto-ionizing Rabi frequency, Ω_c. In order to account for imperfect ground state detection we transform the simulated populations by the following transformation matrix:

$$T_{(\text{sim}\to\text{meas})} = \begin{pmatrix} F_g^2 & 0 & 0 & 0 \\ F_g(1-F_g) & F_g & 0 & 0 \\ F_g(1-F_g) & 0 & F_g & 0 \\ (1-F_g)^2 & 1-F_g & 1-F_g & 1 \end{pmatrix} \tag{6.3}$$

A complication in these simulations is that they assume the Rydberg to auto-ionizing transition can be treated as a two-level system. However, as discussed in section 6.2, there is an inconsistency between the measured light shift, Δ_{LS}, and the value of the light shift one would predict from a two-level modeling of the measured loss rates, Γ_{LS}. Specifically, while Δ_{LS} exhibits the line-shape of a two-level system its measured values over a range of autoionization detunings is $\sim$0.6 of the values predicted by the Γ_{LS} two-level model.

To account for this inconsistency in simulations we set the autoionization Rabi frequency, Ω_c, in order to simulate the measured light shifts, Δ_{LS}, and then adjust the auto-ionizing states measured linewidth, Γ_{ai}, by a factor of 1/0.6 to recreate the mea-

sured ratio of Γ_{LS}/Δ_{LS}. Given, that we calibrate Ω_c by modeling the measured loss rates as a two-level system, for comparing our simulation results to data, we must also multiply our calibrated Ω_c values by a factor of $\sqrt{0.6}$ in order for the simulation to model a light shift, Δ_{LS}, consistent with the measured values.

6.5 Error Expressions

We consider two regimes of errors for a scheme where we light shift the Rydberg state with an autoionizing transition to control excitations to the Rydberg state. The first regime is the blocked regime, where we intend to block the excitation of a target atom to the Rydberg state. The second regime is the cross-talk regime where we intend to leave a non-target atom unaffacted (i.e. excite it to the Rydberg state), however, cross-talk from a light-shifting beam on a target atom inadvertently has some effect on a non-target atom. For both regimes we will derive the theoretical error expressions for two sources of error: rotation errors and scattering errors. For all errors we will discuss the error for a π-pulse ($t = \frac{\pi}{\Omega_r}$) on the non-target atom. While I present the error expressions for a π-pulse on a single atom with a single ground state, the scalings of these errors will generalize to the fidelity of both single-qubit and two-qubit operations on qubits encoded in two ground states, with a single qubit state linked to the Rydberg state (however, some multiplicative factors for the errors may change).

6.5.1 Blocking Errors

For blocking errors we consider the regime where the light shift on the Rydberg state (Δ_{LS}) is much greater than the Rydberg Rabi frequency (Ω_r).

Rotation Error

The Rydberg state population for a blocked atom with light shift, Δ_{LS}, and Rydberg Rabi frequency Ω_r at $t = \frac{2\pi}{\Omega_r}$, will be:

$$P_r = \frac{\Omega_r^2}{\Omega_r^2 + \Delta_{LS}^2} \mathrm{Sin}[\frac{\pi\sqrt{\Omega_r^2 + \Delta_{LS}^2}}{2\Omega_r}]^2 \tag{6.4}$$

For a blocked excitation the desired Rydberg state population is zero, so to get the rotation error scaling we expand the first term to lowest order in $\frac{\Omega_r}{\Delta_{LS}}$ and take the average of the rapidly oscillating sine term to be $\frac{1}{2}$. This gives us an average rotation error of:

$$\epsilon_{\mathrm{rot}} = \frac{1}{2}\left(\frac{\Omega_r}{\Delta_{LS}}\right)^2 \tag{6.5}$$

Scattering Error

Scattering errors will occur when atoms scatter out of the autoionizing state due to the light-shifting beam. Crucially, scattering errors are suppressed because atoms can only be excited to the autoionizing state from the Rydberg state, to which excitation is already blocked. The scattering error during a π-pulse will be given by:

$$\epsilon_{\mathrm{sc}} = \Gamma P_{ai} t_\pi \tag{6.6}$$

Here, Γ is the linewidth of the autoionizing transition, P_{ai} is the population in the autoionizing state, and $t_\pi = \frac{2\pi}{\Omega_r}$. In order to extract P_{ai} as a function of the autoionizing Rabi frequency, Ω_c, and the autoionizing detuning, Δ_x, we diagonalize the full 3-level Hamiltonian (ground state, Rydberg state, autoionizing state) and take the population in the autoionizing state for the eigenstate, which is adiabatically linked

to the ground state. This approximation is valid because we work in the regime where Ω_r is much smaller than Ω_x and Δ_x. The 3-level Hamiltonian is given by:

$$H = \begin{pmatrix} 0 & \frac{\Omega_r}{2} & 0 \\ \frac{\Omega_r}{2} & 0 & \frac{\Omega_c}{2} \\ 0 & \frac{\Omega_c}{2} & \Delta_c \end{pmatrix} \tag{6.7}$$

Diagonalizing H we find the eigenstate adiabatically linked to the ground state ($\left|\psi_g^{'}\right\rangle$), which gives the autoionizing population, P_{ai}, to lowest order in Ω_r:

$$P_{ai} = \left|\left\langle \psi_{ai} \middle| \psi_g^{'} \right\rangle\right|^2 = \frac{1}{1 + \frac{4\Delta_{ai}^2}{\Omega_{ai}^2} + (\frac{\Omega_{ai}}{\Omega_r} + \frac{4\Delta_{ai}^2\Omega_r}{\Omega_{ai}^3})^2} \tag{6.8}$$

Thus the total scattering error over a π-pulse is:

$$\epsilon_{\text{sc}} = \frac{\Gamma}{1 + \frac{4\Delta_{ai}^2}{\Omega_{ai}^2} + (\frac{\Omega_{ai}}{\Omega_r} + \frac{4\Delta_{ai}^2\Omega_r}{\Omega_{ai}^3})^2} \frac{\pi}{\Omega_r} \tag{6.9}$$

As a quick aside, a naive consideration of the scattering error could give the expression $\epsilon_{\text{sc}} = \Gamma_{LS}\langle P_r\rangle t_\pi$, where Γ_{LS} is the effective scattering rate on the autoionizing transition from a two level model of the Rydberg state and autoionizing state and $\langle P_r\rangle$ is the average Rydberg state population. However, this approximation breaks down in the regime of high Ω_c, as it assumes that the ground state and Rydberg state, and, Rydberg state and autoionizing state, can be treated as independent two-level systems instead of the fully correct three level system. Nevertheless, in the regime of low Ω_c, which we will consider for cross-talk errors, this approximation will be a valid method to estimate the scattering error.

6.5.2 Cross-talk Errors

For cross-talk errors we consider the regime where the light shift on the Rydberg state (Δ_{LS}) is much less than the Rydberg Rabi frequency (Ω_r).

Rotation Error

In the case of atoms for which we don't intend to block Rydberg excitation the desired Rydberg state population after a pi-pulse is $P_r = 1$. Thus to find the rotation error in the cross-talk regime we expand 1 - P_r to lowest order in $\frac{\Delta_{LS}}{\Omega_r}$, where P_r is given by equation (6.4). This gives a rotation error of:

$$\epsilon_{\text{rot}} = \left(\frac{\Delta_{LS}}{\Omega_r}\right)^2 \tag{6.10}$$

Scattering Error

As discussed in the scattering error section for the blocking regime, in the cross-talk regime we can describe the scattering error by the effective scattering rate of the Rydberg state to autoionizing state transition (Γ_{LS}) and the average Rydberg state population ($\langle P_r \rangle$) over a π-pulse ($t_\pi = \frac{\pi}{\Omega_r}$). In the regime where $\Delta_{LS} \ll \Omega_r$ the average Rydberg state population over a pi-pulse will simply be $\langle P_r \rangle \approx \frac{1}{2}$. Thus the scattering error in the cross-talk regime is:

$$\epsilon_{\text{sc}} = \frac{\Gamma_{LS}}{2}\frac{\pi}{\Omega_r} \tag{6.11}$$

6.5.3 Comparison with Simulation

Fig. 6.8 shows a comparison of these analytical error expressions with the results of the master equation simulations for $t = \frac{\pi}{\Omega_r}$ at different autoionization detunings, Δ.

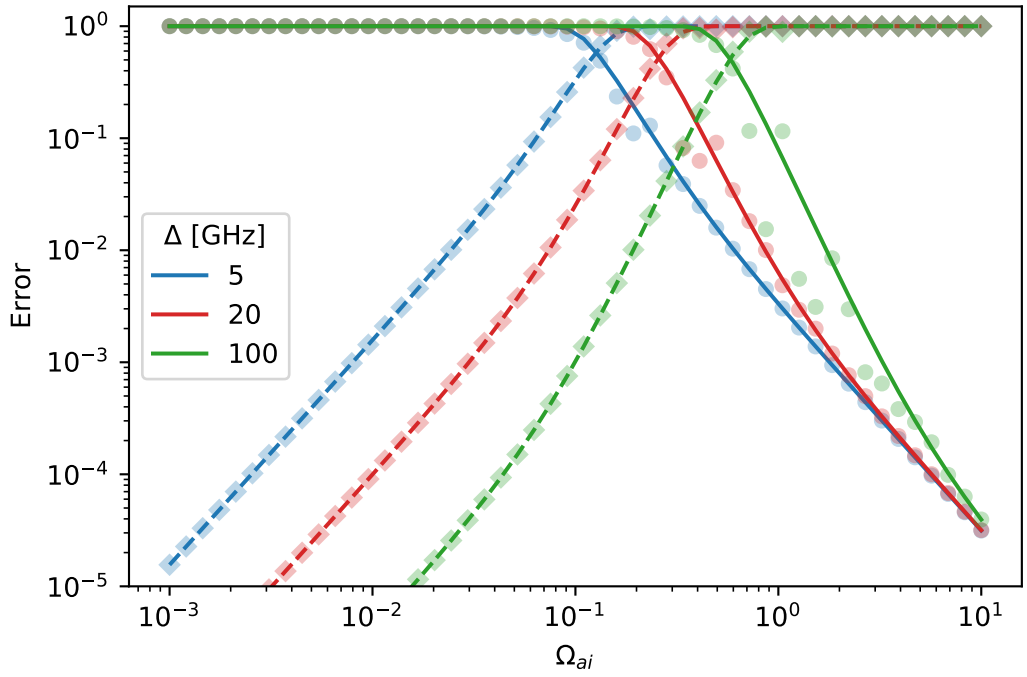

Figure 6.8: A comparison of theoretical error expressions in the blocked and cross-talk regime to simulated populations as a function of autoionization Rabi frequency, Ω_{ai} at different autoionization detunings, Δ. The simulated $1 - P_r$ corresponds to the error in the cross-talk regime and is represented by diamond points in the plot. The simulated $1 - P_g$ corresponds to the error in the blocked regime and is represented by circle points in the plot. The theoretical error expression for the sum of the rotation and scattering errors in the cross-talk regime is shown as a dotted line, while the in the blocked regime the sum of the errors is shown as a solid line.

The theoretical expressions are compared to simulated $1 - P_r$ in the cross-talk regime (diamond points for simulation, dotted line for theoretical curve) and to simulated $1 - P_g$ in the blocked regime (circle points for simulation, solid line for theoretical curve). In all cases the theoretical expressions agree well with the simulated results. Deviations from the curve for blocked errors in the 100 GHz detuning case can be attributed to oscillations in the simulated rotation error, due to a rapidly oscillating term at frequency Δ_{LS}, whereas we compare to only the average rotation error in the theoretical expressions. It is evident that as we move to higher autoionization detunings the power required to achieve certain error rates increases slower than the

suppression of cross-talk errors. Thus, in practice one would choose a desired error threshold and work at the highest detuning where they could achieve that error in the blocked regime at maximum achievable optical power.

Chapter 7

Next steps: Gates in ^{171}Yb

All of the experimental work discussed in this thesis was done using the bosonic ^{174}Yb isotope. However, as discussed in section 1.4, one of the strong motivations for building this platform is to use the I = 1/2 nuclear spin of ^{171}Yb as a nuclear spin qubit. In particular, we plan to use globally addressed Rydberg excitation beams, with locally addressed light-shifting autoionization beams for local control, to drive both single and two-qubit gates.

In ^{171}Yb the qubit will be stored in the $m_F = \pm 1/2$ states of either $^1\mathrm{S}_0\,(\mathrm{F} = 1/2)$ or $^3\mathrm{P}_0\,(\mathrm{F} = 1/2)$. We implement a two-qubit gate using globally-addressed Rydberg beams following the scheme described in Ref. [36], where we selectively drive an excitation of the $|g(m_F = +1/2)\rangle$ ground state to a $|r(S, F = 3/2, m_F = +3/2)\rangle$ Rydberg state. Due to strong hyperfine coupling in alkaline-earth Rydberg states, we can sufficiently split the m_F levels of the F=3/2 Rydberg state with modest magnetic fields, such that the $|g(m_F = -1/2)\rangle \rightarrow |r(m_F = +1/2)\rangle$ transition is far-detuned from the lasers driving the $|g(m_F = +1/2)\rangle \rightarrow |r(m_F = +3/2)\rangle$ transition. The two-qubit gates can be addressed to specific pairs of qubits using local autoionization light shift beams to light shift the Rydberg state of atoms we don't wish to address.

Similarly, single-qubit X rotations can be driven by driving global Raman transitions through the Rydberg state, and locally light-shifting the Rydberg state of non-target atoms.

A current challenge in using ^{171}Yb in our experiment is that our tweezer wavelength, 532 nm, is a magic wavelength for $^1\mathrm{S}_0$ and $^3\mathrm{P}_1\,(m_j = 0)$ but not $^3\mathrm{P}_1\,(m_j = |1|)$, as is shown in Fig. 3.2a. However, if we consider the the m_F sublevels of $^3\mathrm{P}_1\,(\mathrm{F} = 3/2)$ in ^{171}Yb, their m_J components, which can be determined from Clebsch-Gordan coefficients, are:

$$|m_F = 3/2\rangle = |m_J = 1, m_I = +1/2\rangle \tag{7.1}$$

$$|m_F = 1/2\rangle = \sqrt{\frac{2}{3}}\,|m_J = 0, m_I = +1/2\rangle + \sqrt{\frac{1}{3}}\,|m_J = 1, m_I = -1/2\rangle \tag{7.2}$$

That is, neither $m_F = \left|\frac{3}{2}\right|$ nor $m_F = \left|\frac{1}{2}\right|$ sublevels of $^3\mathrm{P}_1\,(\mathrm{F}{=}3/2)$, have a pure component of the magic $m_J = 0$, and consequently neither will be magic with the $^1\mathrm{S}_0\,(\mathrm{F}{=}1/2)$ ground state. The lack of a magic trapping wavelength makes imaging in ^{171}Yb quite difficult as cycling on the imaging transition will heat atoms out of the trap due to rapid and repeated fluctuations in the atom's trapping potential [150]. In our initial attempts to image single ^{171}Yb atoms in 532 nm optical tweezers we measured far shorter atom lifetimes (<1 s) and also collected fewer photons in comparable exposures to our ^{174}Yb imaging, leading to imaging fidelities <95%. Unfortunately, Yb does not benefit to the same degree from non-magic Sisyphus cooling from the trap potentials that has been demonstrated in Sr tweezer arrays [44, 45, 46] because the larger linewidth of the intercombination line does not satisfy the condition $\Gamma \ll \omega_{trap}$. Furthermore, we attempted to implement Raman sideband cooling, which under certain conditions did significantly extend trapped atom lifetimes (>10 s), but

also led to much slower photon scattering rates, and consequently required much longer exposure times for imaging (>200 ms).

As a solution we plan to work at a new trap wavelength, which is magic for $^1S_0$ (F=1/2) and $^3P_1$ (F=3/2, $m_F = \left|\frac{1}{2}\right|$). Calculations of trap polarizability for $^1S_0$ and $^3P_1$ suggest such a wavelength can be found in the range of 470-490 nm and we are currently in the process of performing trap spectroscopy to determine the magic wavelength for future operation.

Bibliography

[1] R. Yamamoto, J. Kobayashi, T. Kuno, K. Kato, and Y. Takahashi, "An ytterbium quantum gas microscope with narrow-line laser cooling," *New Journal of Physics*, vol. 18, 2 2016.

[2] M. H. Anderson, J. R. Ensher, M. R. Matthews, C. E. Wieman, and E. A. Cornell, "Observation of Bose-Einstein Condensation in a Dilute Atomic Vapor," *Science*, vol. 269, pp. 198–201, July 1995.

[3] K. B. Davis, M. O. Mewes, M. R. Andrews, N. J. van Druten, D. S. Durfee, D. M. Kurn, and W. Ketterle, "Bose-Einstein Condensation in a Gas of Sodium Atoms," *Physical Review Letters*, vol. 75, pp. 3969–3973, Nov. 1995.

[4] M. Greiner, O. Mandel, T. Esslinger, T. W. Hänsch, and I. Bloch, "Quantum phase transition from a superfluid to a Mott insulator in a gas of ultracold atoms," *Nature*, vol. 415, pp. 39–44, Jan. 2002.

[5] W. S. Bakr, J. I. Gillen, A. Peng, S. Fölling, and M. Greiner, "A quantum gas microscope for detecting single atoms in a Hubbard-regime optical lattice," *Nature*, vol. 462, pp. 74–77, Nov. 2009.

[6] N. Gemelke, X. Zhang, C.-L. Hung, and C. Chin, "In situ observation of incompressible Mott-insulating domains in ultracold atomic gases," *Nature*, vol. 460, pp. 995–998, Aug. 2009.

[7] J. F. Sherson, C. Weitenberg, M. Endres, M. Cheneau, I. Bloch, and S. Kuhr, "Single-atom-resolved fluorescence imaging of an atomic Mott insulator," *Nature*, vol. 467, pp. 68–72, Sept. 2010.

[8] W. S. Bakr, A. Peng, M. E. Tai, R. Ma, J. Simon, J. I. Gillen, S. Fölling, L. Pollet, and M. Greiner, "Probing the Superfluid–to–Mott Insulator Transition at the Single-Atom Level," *Science*, vol. 329, pp. 547–550, July 2010.

[9] M. Endres, M. Cheneau, T. Fukuhara, C. Weitenberg, P. Schauß, C. Gross, L. Mazza, M. C. Bañuls, L. Pollet, I. Bloch, and S. Kuhr, "Observation of Correlated Particle-Hole Pairs and String Order in Low-Dimensional Mott Insulators," *Science*, vol. 334, pp. 200–203, Oct. 2011.

[10] J. Simon, W. S. Bakr, R. Ma, M. E. Tai, P. M. Preiss, and M. Greiner, "Quantum simulation of antiferromagnetic spin chains in an optical lattice," *Nature*, vol. 472, pp. 307–312, Apr. 2011.

[11] L. W. Cheuk, M. A. Nichols, K. R. Lawrence, M. Okan, H. Zhang, E. Khatami, N. Trivedi, T. Paiva, M. Rigol, and M. W. Zwierlein, "Observation of spatial charge and spin correlations in the 2D Fermi-Hubbard model," *Science*, vol. 353, pp. 1260–1264, Sept. 2016.

[12] D. Mitra, P. T. Brown, E. Guardado-Sanchez, S. S. Kondov, T. Devakul, D. A. Huse, P. Schauß, and W. S. Bakr, "Quantum gas microscopy of an attractive Fermi–Hubbard system," *Nature Physics*, vol. 14, pp. 173–177, Feb. 2018.

[13] P. T. Brown, D. Mitra, E. Guardado-Sanchez, P. Schauß, S. S. Kondov, E. Khatami, T. Paiva, N. Trivedi, D. A. Huse, and W. S. Bakr, "Spin-imbalance in a 2D Fermi-Hubbard system," *Science*, vol. 357, pp. 1385–1388, Sept. 2017.

[14] D. Jaksch, J. I. Cirac, P. Zoller, S. L. Rolston, R. Cote, and M. D. Lukin, "Fast Quantum Gates for Neutral Atoms," *Phys. Rev. Lett.*, vol. 85, pp. 2208–2211,

Sept. 2000.

[15] M. D. Lukin, M. Fleischhauer, R. Cote, L. M. Duan, D. Jaksch, J. I. Cirac, and P. Zoller, "Dipole blockade and quantum information processing in mesoscopic atomic ensembles," *Phys. Rev. Lett.*, vol. 87, p. 037901, Jun 2001.

[16] M. Saffman, T. G. Walker, and K. Mølmer, "Quantum information with rydberg atoms," *Rev. Mod. Phys.*, vol. 82, pp. 2313–2363, Aug 2010.

[17] N. Schlosser, G. Reymond, I. Protsenko, and P. Grangier, "Sub-poissonian loading of single atoms in a microscopic dipole trap," *Nature*, vol. 411, no. 6841, pp. 1024–1027, 2001.

[18] J. Beugnon, C. Tuchendler, H. Marion, A. Gaëtan, Y. Miroshnychenko, Y. R. P. Sortais, A. M. Lance, M. P. A. Jones, G. Messin, A. Browaeys, and P. Grangier, "Two-dimensional transport and transfer of a single atomic qubit in optical tweezers," *Nature Physics*, vol. 3, pp. 696–699, Oct. 2007.

[19] D. D. Yavuz, P. B. Kulatunga, E. Urban, T. A. Johnson, N. Proite, T. Henage, T. G. Walker, and M. Saffman, "Fast Ground State Manipulation of Neutral Atoms in Microscopic Optical Traps," *Physical Review Letters*, vol. 96, p. 063001, Feb. 2006.

[20] M. P. A. Jones, J. Beugnon, A. Gaëtan, J. Zhang, G. Messin, A. Browaeys, and P. Grangier, "Fast quantum state control of a single trapped neutral atom," *Physical Review A*, vol. 75, p. 040301, Apr. 2007.

[21] A. Fuhrmanek, R. Bourgain, Y. R. P. Sortais, and A. Browaeys, "Free-Space Lossless State Detection of a Single Trapped Atom," *Physical Review Letters*, vol. 106, p. 133003, Mar. 2011.

[22] A. M. Kaufman, B. J. Lester, and C. A. Regal, "Cooling a Single Atom in an Optical Tweezer to Its Quantum Ground State," *Physical Review X*, vol. 2,

p. 041014, Nov. 2012.

[23] J. D. Thompson, T. G. Tiecke, A. S. Zibrov, V. Vuletić, and M. D. Lukin, "Coherence and Raman Sideband Cooling of a Single Atom in an Optical Tweezer," *Physical Review Letters*, vol. 110, p. 133001, Mar. 2013.

[24] D. Hayes, P. S. Julienne, and I. H. Deutsch, "Quantum Logic via the Exchange Blockade in Ultracold Collisions," *Physical Review Letters*, vol. 98, p. 070501, Feb. 2007.

[25] M. Anderlini, P. J. Lee, B. L. Brown, J. Sebby-Strabley, W. D. Phillips, and J. V. Porto, "Controlled exchange interaction between pairs of neutral atoms in an optical lattice," *Nature*, vol. 448, pp. 452–456, July 2007.

[26] A. M. Kaufman, B. J. Lester, M. Foss-Feig, M. L. Wall, A. M. Rey, and C. A. Regal, "Entangling two transportable neutral atoms via local spin exchange," *Nature*, vol. 527, pp. 208–211, Nov. 2015.

[27] J. D. Thompson, T. G. Tiecke, N. P. d. Leon, J. Feist, A. V. Akimov, M. Gullans, A. S. Zibrov, V. Vuletić, and M. D. Lukin, "Coupling a Single Trapped Atom to a Nanoscale Optical Cavity," *Science*, vol. 340, pp. 1202–1205, June 2013.

[28] T. G. Tiecke, J. D. Thompson, N. P. de Leon, L. R. Liu, V. Vuletić, and M. D. Lukin, "Nanophotonic quantum phase switch with a single atom," *Nature*, vol. 508, pp. 241–244, Apr. 2014.

[29] S. Welte, B. Hacker, S. Daiss, S. Ritter, and G. Rempe, "Photon-Mediated Quantum Gate between Two Neutral Atoms in an Optical Cavity," *Phys. Rev. X*, vol. 8, p. 011018, Feb. 2018.

[30] M. Endres, H. Bernien, A. Keesling, H. Levine, E. R. Anschuetz, A. Krajenbrink, C. Senko, V. Vuletic, M. Greiner, and M. D. Lukin, "Atom-by-atom

assembly of defect-free one-dimensional cold atom arrays," *Science*, vol. 354, pp. 1024–1027, Nov. 2016.

[31] D. Barredo, S. de Léséluc, V. Lienhard, T. Lahaye, and A. Browaeys, "An atom-by-atom assembler of defect-free arbitrary two-dimensional atomic arrays," *Science*, vol. 354, no. 6315, pp. 1021–1023, 2016.

[32] D. Barredo, V. Lienhard, S. de Léséleuc, T. Lahaye, and A. Browaeys, "Synthetic three-dimensional atomic structures assembled atom by atom," *Nature*, vol. 561, pp. 79–82, Sept. 2018.

[33] E. Urban, T. A. Johnson, T. Henage, L. Isenhower, D. D. Yavuz, T. G. Walker, and M. Saffman, "Observation of Rydberg blockade between two atoms," *Nature Physics*, vol. 5, no. 2, pp. 110–114, 2009.

[34] T. Wilk, A. Gaëtan, C. Evellin, J. Wolters, Y. Miroshnychenko, P. Grangier, and A. Browaeys, "Entanglement of Two Individual Neutral Atoms Using Rydberg Blockade," *Phys. Rev. Lett.*, vol. 104, p. 010502, Jan. 2010.

[35] L. Isenhower, E. Urban, X. L. Zhang, A. T. Gill, T. Henage, T. A. Johnson, T. G. Walker, and M. Saffman, "Demonstration of a Neutral Atom Controlled-NOT Quantum Gate," *Phys. Rev. Lett.*, vol. 104, p. 010503, Jan. 2010.

[36] H. Levine, A. Keesling, G. Semeghini, A. Omran, T. T. Wang, S. Ebadi, H. Bernien, M. Greiner, V. Vuletić, H. Pichler, and M. D. Lukin, "Parallel Implementation of High-Fidelity Multiqubit Gates with Neutral Atoms," *Physical Review Letters*, vol. 123, p. 170503, 10 2019.

[37] H. Bernien, S. Schwartz, A. Keesling, H. Levine, A. Omran, H. Pichler, S. Choi, A. S. Zibrov, M. Endres, M. Greiner, V. Vuletic, and M. D. Lukin, "Probing many-body dynamics on a 51-atom quantum simulator," *Nature*, vol. 551, pp. 579–584, 11 2017.

[38] V. Lienhard, S. De Léséleuc, D. Barredo, T. Lahaye, A. Browaeys, M. Schuler, L. P. Henry, and A. M. Läuchli, "Observing the Space- and Time-Dependent Growth of Correlations in Dynamically Tuned Synthetic Ising Models with Antiferromagnetic Interactions," *Physical Review X*, vol. 8, 6 2018.

[39] T. Topcu and A. Derevianko, "Divalent Rydberg atoms in optical lattices: Intensity landscape and magic trapping," *Physical Review A*, vol. 89, p. 023411, 2 2014.

[40] J. Wilson, S. Saskin, Y. Meng, S. Ma, R. Dilip, A. Burgers, and J. Thompson, "Trapped arrays of alkaline earth Rydberg atoms in optical tweezers," *arXiv:1912.08754 [physics, physics:quant-ph]*, Dec. 2019. arXiv: 1912.08754.

[41] R. Beigang, W. Makat, A. Timmermann, and P. J. West, "Hyperfine-Induced n Mixing in High Rydberg States of 87Sr," *Phys. Rev. Lett.*, vol. 51, pp. 771–774, Aug. 1983.

[42] P. F. Liao, R. R. Freeman, R. Panock, and L. M. Humphrey, "Hyperfine-induced singlet-triplet mixing in 3He," *Opt Commun*, vol. 34, pp. 195–198, Aug. 1980.

[43] F. Robicheaux, D. W. Booth, and M. Saffman, "Theory of long-range interactions for Rydberg states attached to hyperfine-split cores," *Phys Rev A*, vol. 97, p. 022508, Feb. 2018.

[44] A. Cooper, J. P. Covey, I. S. Madjarov, S. G. Porsev, M. S. Safronova, and M. Endres, "Alkaline-Earth Atoms in Optical Tweezers," *Physical Review X*, vol. 8, 12 2018.

[45] M. A. Norcia, A. W. Young, and A. M. Kaufman, "Microscopic Control and Detection of Ultracold Strontium in Optical-Tweezer Arrays," *Physical Review X*, vol. 8, 12 2018.

[46] J. P. Covey, I. S. Madjarov, A. Cooper, and M. Endres, "2000-Times Repeated Imaging of Strontium Atoms in Clock-Magic Tweezer Arrays," *Physical Review Letters*, vol. 122, 5 2019.

[47] M. A. Norcia, A. W. Young, W. J. Eckner, E. Oelker, J. Ye, and A. M. Kaufman, "Seconds-scale coherence on an optical clock transition in a tweezer array," *Science*, vol. 366, pp. 93–97, 10 2019.

[48] A. W. Young, W. J. Eckner, W. R. Milner, D. Kedar, M. A. Norcia, E. Oelker, N. Schine, J. Ye, and A. M. Kaufman, "Half-minute-scale atomic coherence and high relative stability in a tweezer clock," *Nature*, vol. 588, no. 7838, pp. 408–413, 2020.

[49] I. S. Madjarov, A. Cooper, A. L. Shaw, J. P. Covey, V. Schkolnik, T. H. Yoon, J. R. Williams, and M. Endres, "An atomic array optical clock with single-atom readout," 8 2019.

[50] I. S. Madjarov, J. P. Covey, A. L. Shaw, J. Choi, A. Kale, A. Cooper, H. Pichler, V. Schkolnik, J. R. Williams, and M. Endres, "High-fidelity entanglement and detection of alkaline-earth rydberg atoms," *Nature Physics*, vol. 16, no. 8, pp. 857–861, 2020.

[51] K. M. Jones, E. Tiesinga, P. D. Lett, and P. S. Julienne, "Ultracold photoassociation spectroscopy: Long-range molecules and atomic scattering," *Reviews of Modern Physics*, vol. 78, pp. 483–535, May 2006.

[52] F. Nogrette, H. Labuhn, S. Ravets, D. Barredo, L. Béguin, A. Vernier, T. Lahaye, and A. Browaeys, "Single-Atom Trapping in Holographic 2D Arrays of Microtraps with Arbitrary Geometries," *Physical Review X*, vol. 4, p. 021034, May 2014.

[53] C. L. Vaillant, M. P. A. Jones, and R. M. Potvliege, "Multichannel quantum de-

fect theory of strontium bound Rydberg states," *Journal of Physics B: Atomic, Molecular and Optical Physics*, vol. 47, p. 155001, 8 2014.

[54] T. Förster, "Zwischenmolekulare energiewanderung und fluoreszenz," *Annalen der Physik*, vol. 437, no. 1-2, p. 55–75, 1948.

[55] A. Gaëtan, Y. Miroshnychenko, T. Wilk, A. Chotia, M. Viteau, D. Comparat, P. Pillet, A. Browaeys, and P. Grangier, "Observation of collective excitation of two individual atoms in the rydberg blockade regime," *Nature Physics*, vol. 5, no. 2, p. 115–118, 2009.

[56] M. A. Nielsen and I. L. Chuang, *Quantum computation and quantum information*. Cambridge University Press, 2000.

[57] M. Saffman and T. G. Walker, "Analysis of a quantum logic device based on dipole-dipole interactions of optically trapped Rydberg atoms," *Physical Review A*, vol. 72, p. 022347, 8 2005.

[58] M. Saffman, X. L. Zhang, A. T. Gill, L. Isenhower, and T. G. Walker, "Rydberg state mediated quantum gates and entanglement of pairs of neutral atoms," *Journal of Physics: Conference Series*, vol. 264, p. 012023, Jan. 2011.

[59] H. Levine, A. Keesling, A. Omran, H. Bernien, S. Schwartz, A. S. Zibrov, M. Endres, M. Greiner, V. Vuletić, and M. D. Lukin, "High-Fidelity Control and Entanglement of Rydberg-Atom Qubits," *Physical Review Letters*, vol. 121, 9 2018.

[60] A. D. Ludlow, M. M. Boyd, J. Ye, E. Peik, and P. O. Schmidt, "Optical atomic clocks," *Rev Mod Phys*, vol. 87, p. 637, 2015.

[61] T. Topcu and A. Derevianko, "Intensity landscape and the possibility of magic trapping of alkali-metal Rydberg atoms in infrared optical lattices," *Physical Review A*, vol. 88, p. 043407, 10 2013.

[62] S. R. Cohen and J. D. Thompson, "Quantum Computing with Circular Rydberg Atoms," *arXiv:2103.12744 [physics, physics:quant-ph]*, Mar. 2021. arXiv: 2103.12744.

[63] G. Lochead, D. Boddy, D. P. Sadler, C. S. Adams, and M. P. A. Jones, "Number-resolved imaging of excited-state atoms using a scanning autoionization microscope," *Phys. Rev. A*, vol. 87, p. 053409, May 2013.

[64] A. Tauschinsky, R. Newell, H. B. van Linden van den Heuvell, and R. J. C. Spreeuw, "Measurement of ^{87}rb rydberg-state hyperfine splitting in a room-temperature vapor cell," *Phys. Rev. A*, vol. 87, p. 042522, Apr 2013.

[65] R. Senaratne, S. V. Rajagopal, Z. A. Geiger, K. M. Fujiwara, V. Lebedev, and D. M. Weld, "Effusive atomic oven nozzle design using an aligned microcapillary array," *Rev. Sci. Instrum.*, vol. 86, p. 023105, Feb. 2015.

[66] M. Knudsen, *The kinetic theory of gases; some modern aspects*. Methuen, 1950.

[67] T. Hosoya, M. Miranda, R. Inoue, and M. Kozuma, "Injection locking of a high power ultraviolet laser diode for laser cooling of ytterbium atoms," *Review of Scientific Instruments*, vol. 86, no. 7, p. 073110, 2015.

[68] B. Saxberg, B. Plotkin-Swing, and S. Gupta, "Active stabilization of a diode laser injection lock," *Review of Scientific Instruments*, vol. 87, no. 6, p. 063109, 2016.

[69] D. Gangloff, M. Shi, T. Wu, A. Bylinskii, B. Braverman, M. Gutierrez, R. Nichols, J. Li, K. Aichholz, M. Cetina, L. Karpa, B. Jelenković, I. Chuang, and V. Vuletić, "Preventing and reversing vacuum-induced optical losses in high-finesse tantalum (V) oxide mirror coatings," *Optics Express*, vol. 23, pp. 18014–18028, July 2015.

[70] J. Dijon, E. Quesnel, C. Pelle, and R. Thielsch, "Laser damage of optical coatings from UV to deep UV at 193 nm," in *Laser-Induced Damage in Optical Materials: 1998*, vol. 3578, pp. 54–63, International Society for Optics and Photonics, Apr. 1999.

[71] G. D. Boyd and D. A. Kleinman, "Parametric Interaction of Focused Gaussian Light Beams," *Journal of Applied Physics*, vol. 39, pp. 3597–3639, July 1968.

[72] A. C. Wilson, C. Ospelkaus, A. P. Vandevender, J. A. Mlynek, K. R. Brown, D. Leibfried, and D. J. Wineland, "A 750-mw, continuous-wave, solid-state laser source at 313 nm for cooling and manipulating trapped ^{9}be ions," *Applied Physics B*, vol. 105, no. 4, p. 741–748, 2011.

[73] R. W. P. Drever, J. L. Hall, F. V. Kowalski, J. Hough, G. M. Ford, A. J. Munley, and H. Ward, "Laser phase and frequency stabilization using an optical resonator," *Applied Physics B*, vol. 31, pp. 97–105, June 1983.

[74] S. Hannig, J. Mielke, J. A. Fenske, M. Misera, N. Beev, C. Ospelkaus, and P. O. Schmidt, "A highly stable monolithic enhancement cavity for second harmonic generation in the ultraviolet," *Review of Scientific Instruments*, vol. 89, p. 013106, Jan. 2018.

[75] T. Freegarde and C. Zimmermann, "On the design of enhancement cavities for second harmonic generation," *Optics Communications*, vol. 199, no. 5-6, p. 435–446, 2001.

[76] T. Hansch and B. Couillaud, "Laser frequency stabilization by polarization spectroscopy of a reflecting reference cavity," *Optics Communications*, vol. 35, no. 3, p. 441–444, 1980.

[77] F. Laeri, R. Jungen, G. Angelow, U. Vietze, T. Engel, M. WüRtz, and D. Hilgenberg, "Photorefraction in the ultraviolet: Materials and effects," *Ap-*

plied Physics B Laser and Optics, vol. 61, no. 4, p. 351–360, 1995.

[78] W. D. Phillips and H. Metcalf, "Laser deceleration of an atomic beam," *Physical Review Letters*, vol. 48, no. 9, p. 596–599, 1982.

[79] K. Dieckmann, R. J. C. Spreeuw, M. Weidemüller, and J. T. M. Walraven, "Two-dimensional magneto-optical trap as a source of slow atoms," *Physical Review A*, vol. 58, pp. 3891–3895, Nov. 1998.

[80] T. G. Tiecke, S. D. Gensemer, A. Ludewig, and J. T. M. Walraven, "High-flux two-dimensional magneto-optical-trap source for cold lithium atoms," *Phys Rev A*, vol. 80, p. 013409, July 2009.

[81] S. Saskin, J. T. Wilson, B. Grinkemeyer, and J. D. Thompson, "Narrow-line cooling and imaging of ytterbium atoms in an optical tweezer array," *Phys. Rev. Lett.*, vol. 122, p. 143002, Apr 2019.

[82] A. Omran, M. Boll, T. A. Hilker, K. Kleinlein, G. Salomon, I. Bloch, and C. Gross, "Microscopic Observation of Pauli Blocking in Degenerate Fermionic Lattice Gases," *Phys. Rev. Lett.*, vol. 115, p. 263001, Dec. 2015.

[83] M. F. Parsons, F. Huber, A. Mazurenko, C. S. Chiu, W. Setiawan, K. Wooley-Brown, S. Blatt, and M. Greiner, "Site-Resolved Imaging of Fermionic ^{6}Li in an Optical Lattice," *Phys. Rev. Lett.*, vol. 114, p. 213002, May 2015.

[84] L. W. Cheuk, M. A. Nichols, M. Okan, T. Gersdorf, V. V. Ramasesh, W. S. Bakr, T. Lompe, and M. W. Zwierlein, "Quantum-Gas Microscope for Fermionic Atoms," *Phys. Rev. Lett.*, vol. 114, p. 193001, May 2015.

[85] G. J. A. Edge, R. Anderson, D. Jervis, D. C. McKay, R. Day, S. Trotzky, and J. H. Thywissen, "Imaging and addressing of individual fermionic atoms in an optical lattice," *Phys Rev A*, vol. 92, p. 063406, Dec. 2015.

[86] E. Haller, J. Hudson, A. Kelly, D. A. Cotta, B. Peaudecerf, G. D. Bruce, and S. Kuhr, "Single-atom imaging of fermions in a quantum-gas microscope," *Nature Physics*, vol. 11, pp. 738–742, Sept. 2015.

[87] M. Miranda, R. Inoue, N. Tambo, and M. Kozuma, "Site-resolved imaging of a bosonic Mott insulator using ytterbium atoms," *Phys Rev A*, vol. 96, p. 043626, Oct. 2017.

[88] G. Reymond, N. Schlosser, I. Protsenko, and P. Grangier, "Single-atom manipulations in a microscopic dipole trap," *Philos T Roy Soc A*, vol. 361, no. 1808, pp. 1527–1536, 2003.

[89] P. Lett, W. Phillips, S. Rolston, C. Tanner, R. Watts, and C. Westbrook, "Optical molasses," *J Opt Soc Am B*, vol. 6, no. 11, pp. 2084–2107, 1989.

[90] See Supplemental Material at [URL will be inserted by publisher], which includes Ref. [51].

[91] V. A. Dzuba, V. V. Flambaum, and S. Schiller, "Testing physics beyond the standard model through additional clock transitions in neutral ytterbium," *Phys Rev A*, vol. 98, p. 022501, Aug. 2018.

[92] C. J. Picken, R. Legaie, and J. D. Pritchard, "Single atom imaging with an sCMOS camera," *Appl Phys Lett*, vol. 111, p. 164102, Oct. 2017.

[93] A. Frisch, K. Aikawa, M. Mark, A. Rietzler, J. Schindler, E. Zupanič, R. Grimm, and F. Ferlaino, "Narrow-line magneto-optical trap for erbium," *Phys Rev A*, vol. 85, p. 051401, May 2012.

[94] M. Lu, S. H. Youn, and B. L. Lev, "Spectroscopy of a narrow-line laser-cooling transition in atomic dysprosium," *Phys Rev A*, vol. 83, p. 012510, Jan. 2011.

[95] C. Bowers, D. Budker, S. Freedman, G. Gwinner, J. Stalnaker, and D. DeMille, "Experimental investigation of the $6s^2 1S_0 \rightarrow 5d6s^3 D_{1,2}$ forbidden transitions in atomic ytterbium," *Phys Rev A*, vol. 59, pp. 3513–3526, May 1999.

[96] L. Couturier, I. Nosske, F. Hu, C. Tan, C. Qiao, Y. H. Jiang, P. Chen, and M. Weidemüller, "Measurement of the strontium triplet Rydberg series by depletion spectroscopy of ultracold atoms," *Physical Review A*, vol. 99, 2 2019.

[97] J. Hostetter, J. D. Pritchard, J. E. Lawler, and M. Saffman, "Measurement of holmium Rydberg series through magneto-optical trap depletion spectroscopy," *Physical Review A - Atomic, Molecular, and Optical Physics*, vol. 91, 1 2015.

[98] L. Nenadovi and J. J. J. Mcferran, "Related content Clock and intercombination line frequency separation in 171 Yb," *J. Phys. B: At. Mol. Opt. Phys*, vol. 49, p. 65004, 2016.

[99] K. Pandey, A. K. Singh, P. V. Kumar, M. V. Suryanarayana, and V. Natarajan, "Isotope shifts and hyperfine structure in the 555.8-nm S1 0 $\rightarrow$ P3 1 line of Yb," *Physical Review A - Atomic, Molecular, and Optical Physics*, vol. 80, 8 2009.

[100] H. Lehec, A. Zuliani, W. Maineult, E. Luc-Koenig, P. Pillet, P. Cheinet, F. Niyaz, and T. F. Gallagher, "Laser and microwave spectroscopy of even-parity Rydberg states of neutral ytterbium and multichannel-quantum-defect-theory analysis," *Physical Review A*, vol. 98, p. 062506, 12 2018.

[101] M. Aymar, R. J. Champeau, C. Delsart, and O. Robaux, "Three-step laser spectroscopy and multichannel quantum defect analysis of odd-parity Rydberg states of neutral ytterbium," *Journal of Physics B: Atomic and Molecular Physics*, vol. 17, no. 18, pp. 3645–3661, 1984.

[102] S. K. Dutta, J. R. Guest, D. Feldbaum, A. Walz-Flannigan, and G. Raithel, "Ponderomotive optical lattice for rydberg atoms," *Phys. Rev. Lett.*, vol. 85,

pp. 5551–5554, Dec 2000.

[103] M. Archimi, C. Simonelli, L. Di Virgilio, A. Greco, M. Ceccanti, E. Arimondo, D. Ciampini, I. I. Ryabtsev, I. I. Beterov, and O. Morsch, "Measurements of single-state and state-ensemble lifetimes of high-lying Rb Rydberg levels," *Physical Review A*, vol. 100, 9 2019.

[104] T. Nguyen, J. Raimond, C. Sayrin, R. Cortiñas, T. Cantat-Moltrecht, F. Assemat, I. Dotsenko, S. Gleyzes, S. Haroche, G. Roux, T. Jolicoeur, and M. Brune, "Towards Quantum Simulation with Circular Rydberg Atoms," *Physical Review X*, vol. 8, p. 011032, 2 2018.

[105] D. Barredo, V. Lienhard, P. Scholl, S. de Léséleuc, T. Boulier, A. Browaeys, and T. Lahaye, "Three-dimensional trapping of individual rydberg atoms in ponderomotive bottle beam traps," *Physical Review Letters*, vol. 124, no. 2, 2020.

[106] T. M. Graham, M. Kwon, B. Grinkemeyer, Z. Marra, X. Jiang, M. T. Lichtman, Y. Sun, M. Ebert, and M. Saffman, "Rydberg-mediated entanglement in a two-dimensional neutral atom qubit array," *Phys. Rev. Lett.*, vol. 123, p. 230501, Dec 2019.

[107] S. E. Anderson, K. C. Younge, and G. Raithel, "Trapping Rydberg Atoms in an Optical Lattice," *Physical Review Letters*, vol. 107, p. 263001, 12 2011.

[108] L. Li, Y. O. Dudin, and A. Kuzmich, "Entanglement between light and an optical atomic excitation," *Nature*, vol. 498, pp. 466–469, 6 2013.

[109] D. A. Anderson, A. Schwarzkopf, R. E. Sapiro, and G. Raithel, "Production and trapping of cold circular Rydberg atoms," *Physical Review A*, vol. 88, p. 031401, 9 2013.

[110] S. D. Hogan and F. Merkt, "Demonstration of Three-Dimensional Electrostatic Trapping of State-Selected Rydberg Atoms," *Physical Review Letters*, vol. 100, p. 043001, 1 2008.

[111] R. G. Cortiñas, M. Favier, B. Ravon, P. Méhaignerie, Y. Machu, J. M. Raimond, C. Sayrin, and M. Brune, "Laser trapping of circular rydberg atoms," *Phys. Rev. Lett.*, vol. 124, p. 123201, Mar 2020.

[112] A. Roy, S. De, B. Arora, and B. K. Sahoo, "Accurate determination of blackbody radiation shift, magic and tune-out wavelengths for the $6S_{1/2} \rightarrow 5D_{3/2}$ clock transition in Yb^+," *Journal of Physics B: Atomic, Molecular and Optical Physics*, vol. 50, p. 205201, 10 2017.

[113] K. Guo, G. Wang, and A. Ye, "Dipole polarizabilities and magic wavelengths for a Sr and Yb atomic optical lattice clock," *Journal of Physics B: Atomic, Molecular and Optical Physics*, vol. 43, p. 135004, 7 2010.

[114] V. A. Dzuba and A. Derevianko, "Dynamic polarizabilities and related properties of clock states of the ytterbium atom," *Journal of Physics B: Atomic, Molecular and Optical Physics*, vol. 43, p. 074011, 4 2010.

[115] B. Knuffman and G. Raithel, "Multipole transitions of Rydberg atoms in modulated ponderomotive potentials," *Physical Review A*, vol. 75, p. 053401, 5 2007.

[116] R. Cardman and G. Raithel, "Circularizing Rydberg atoms with time-dependent optical traps," 9 2019.

[117] A. R. Edmonds, *Angular momentum in quantum mechanics*. Princeton University Press, 1996.

[118] J. Neukammer, H. Rinneberg, and U. Majewski, "Diamagnetic shift and singlet-triplet mixing of 6snp Yb Rydberg states with large radial extent," *Physical Review A*, vol. 30, pp. 1142–1144, 8 1984.

[119] A. E. Siegman, *Lasers*. Univ. Science Books, 1986.

[120] S. Kuhr, W. Alt, D. Schrader, I. Dotsenko, Y. Miroshnychenko, A. Rauschenbeutel, and D. Meschede, "Analysis of dephasing mechanisms in a standing-wave dipole trap," *Physical Review A*, vol. 72, p. 023406, 8 2005.

[121] T. Topcu and A. Derevianko, "Possibility of triple magic trapping of clock and Rydberg states of divalent atoms in optical lattices," *Journal of Physics B: Atomic, Molecular and Optical Physics*, vol. 49, p. 144004, 7 2016.

[122] W. E. Cooke and T. F. Gallagher, "Calculation of autoionization rates for high-angular-momentum Rydberg states," *Physical Review A*, vol. 19, no. 6, pp. 2151–2153, 1979.

[123] D. Hayes, S. Olmschenk, D. N. Matsukevich, P. Maunz, D. L. Moehring, K. C. Younge, and C. Monroe, "Measurement of the lifetime of the 6p P2 1/2 o level of Yb+," *Physical Review A - Atomic, Molecular, and Optical Physics*, vol. 80, 8 2009.

[124] W. E. Cooke, T. F. Gallagher, S. A. Edelstein, and R. M. Hill, "Doubly excited autoionizing Rydberg states of Sr," *Physical Review Letters*, vol. 40, no. 3, pp. 178–181, 1978.

[125] E. Y. Xu, Y. Zhu, O. C. Mullins, and T. F. Gallagher, "Sr 5 p 1 / 2 ns 1 / 2 and 5 p 3 / 2 ns 1 / 2 J=1 autoionizing states," *Physical Review A*, vol. 33, pp. 2401–2409, 4 1986.

[126] C. B. Xu, X. Y. Xu, W. Huang, M. Xue, and D. Y. Chen, "Rydberg and autoionizing states of neutral ytterbium," *Journal of Physics B: Atomic, Molecular and Optical Physics*, vol. 27, pp. 3905–3913, sep 1994.

[127] G. Fields, X. Zhang, F. B. Dunning, S. Yoshida, and J. Burgdörfer, "Autoionization of very-high- n strontium Rydberg states," *Physical Review A*, vol. 97,

1 2018.

[128] T. F. Gallagher, *Rydberg Atoms*. Cambridge: Cambridge University Press, 1994.

[129] A. Burgess and M. J. Seaton, "Cross Sections for Photoionization from Valence-Electron States," *Reviews of Modern Physics*, vol. 30, pp. 992–993, 7 1958.

[130] P. Schauß, M. Cheneau, M. Endres, T. Fukuhara, S. Hild, A. Omran, T. Pohl, C. Gross, S. Kuhr, and I. Bloch, "Observation of spatially ordered structures in a two-dimensional rydberg gas," *Nature*, vol. 491, no. 7422, pp. 87–91, 2012.

[131] A. M. Hankin, Y.-Y. Jau, L. P. Parazzoli, C. W. Chou, D. J. Armstrong, A. J. Landahl, and G. W. Biedermann, "Two-atom rydberg blockade using direct $6s$ to np excitation," *Phys. Rev. A*, vol. 89, p. 033416, Mar 2014.

[132] H. Labuhn, S. Ravets, D. Barredo, L. Béguin, F. Nogrette, T. Lahaye, and A. Browaeys, "Single-atom addressing in microtraps for quantum-state engineering using rydberg atoms," *Phys. Rev. A*, vol. 90, p. 023415, Aug 2014.

[133] A. Omran, H. Levine, A. Keesling, G. Semeghini, T. T. Wang, S. Ebadi, H. Bernien, A. S. Zibrov, H. Pichler, S. Choi, J. Cui, M. Rossignolo, P. Rembold, S. Montangero, T. Calarco, M. Endres, M. Greiner, V. Vuletić, and M. D. Lukin, "Generation and manipulation of schrödinger cat states in rydberg atom arrays," *Science*, vol. 365, no. 6453, pp. 570–574, 2019.

[134] C. Weitenberg, M. Endres, J. F. Sherson, M. Cheneau, P. Schauß, T. Fukuhara, I. Bloch, and S. Kuhr, "Single-spin addressing in an atomic mott insulator," *Nature*, vol. 471, no. 7338, pp. 319–324, 2011.

[135] Y. Wang, X. Zhang, T. A. Corcovilos, A. Kumar, and D. S. Weiss, "Coherent addressing of individual neutral atoms in a 3d optical lattice," *Phys. Rev. Lett.*, vol. 115, p. 043003, Jul 2015.

[136] J. Wilson, S. Saskin, Y. Meng, S. Ma, R. Dilip, A. Burgers, and J. Thompson, "Trapped arrays of alkaline earth rydberg atoms in optical tweezers," 2019.

[137] W. E. Cooke, T. F. Gallagher, S. A. Edelstein, and R. M. Hill, "Doubly excited autoionizing rydberg states of sr," *Phys. Rev. Lett.*, vol. 40, pp. 178–181, Jan 1978.

[138] T. F. Gallagher, "Doubly excited states," *J. Opt. Soc. Am. B*, vol. 4, pp. 794–804, May 1987.

[139] H. Levine, A. Keesling, G. Semeghini, A. Omran, T. T. Wang, S. Ebadi, H. Bernien, M. Greiner, V. Vuletić, H. Pichler, and M. D. Lukin, "Parallel implementation of high-fidelity multiqubit gates with neutral atoms," *Phys. Rev. Lett.*, vol. 123, p. 170503, Oct 2019.

[140] M. Saffman, I. I. Beterov, A. Dalal, E. J. Páez, and B. C. Sanders, "Symmetric rydberg controlled-z gates with adiabatic pulses," *Phys. Rev. A*, vol. 101, p. 062309, Jun 2020.

[141] R. A. Cline, J. D. Miller, M. R. Matthews, and D. J. Heinzen, "Spin relaxation of optically trapped atoms by light scattering," *Optics Letters*, vol. 19, no. 3, p. 207, 1994.

[142] M. Endres, H. Bernien, A. Keesling, H. Levine, E. R. Anschuetz, A. Krajenbrink, C. Senko, V. Vuletic, M. Greiner, and M. D. Lukin, "Atom-by-atom assembly of defect-free one-dimensional cold atom arrays," *Science*, p. 3752, 2016.

[143] D. Barredo, S. de Léséleuc, V. Lienhard, T. Lahaye, and A. Browaeys, "An atom-by-atom assembler of defect-free arbitrary two-dimensional atomic arrays," *Science*, vol. 354, no. 6315, pp. 1021–1023, 2016.

[144] I. Zalivako, I. Semerikov, A. Borisenko, V. Smirnov, P. Vishnyakov, M. Aksenov, P. Sidorov, N. Kolachevsky, and K. Khabarova, "Improved wavelength measurement of 2s1/2→2p1/2 and 2d3/2→3[3/2]1/2 transitions in yb+," *Journal of Russian Laser Research*, vol. 40, no. 4, pp. 375–381, 2019.

[145] S. Olmschenk, D. Hayes, D. N. Matsukevich, P. Maunz, D. L. Moehring, K. C. Younge, and C. Monroe, "Measurement of the lifetime of the $6p\ ^2P^o_{1/2}$ level of yb^+," *Phys. Rev. A*, vol. 80, p. 022502, Aug 2009.

[146] C. B. Xu, X. Y. Xu, W. Huang, M. Xue, and D. Y. Chen, "Rydberg and autoionizing states of neutral ytterbium," *Journal of Physics B: Atomic, Molecular and Optical Physics*, vol. 27, pp. 3905–3913, sep 1994.

[147] W. E. Cooke and T. F. Gallagher, "Observation of pair splittings in the autoionization spectrum of ba," *Phys. Rev. Lett.*, vol. 41, pp. 1648–1652, Dec 1978.

[148] N. H. Tran, R. Kachru, and T. F. Gallagher, "Multistep laser excitation of barium: Apparent interferences due to overlap-integral variations," *Phys. Rev. A*, vol. 26, pp. 3016–3019, Nov 1982.

[149] D. A. Steck, *Quantum and Atom Optics*. http://steck.us/teaching, 2007.

[150] T. A. Savard, K. M. O'Hara, and J. E. Thomas, "Laser-noise-induced heating in far-off resonance optical traps," *Physical Review A*, vol. 56, no. 2, 1997.